Post buckling of curved skin-stiffened metal panels under shear loading

An investigation using virtual testing

MSc Thesis

Ayush Prasad

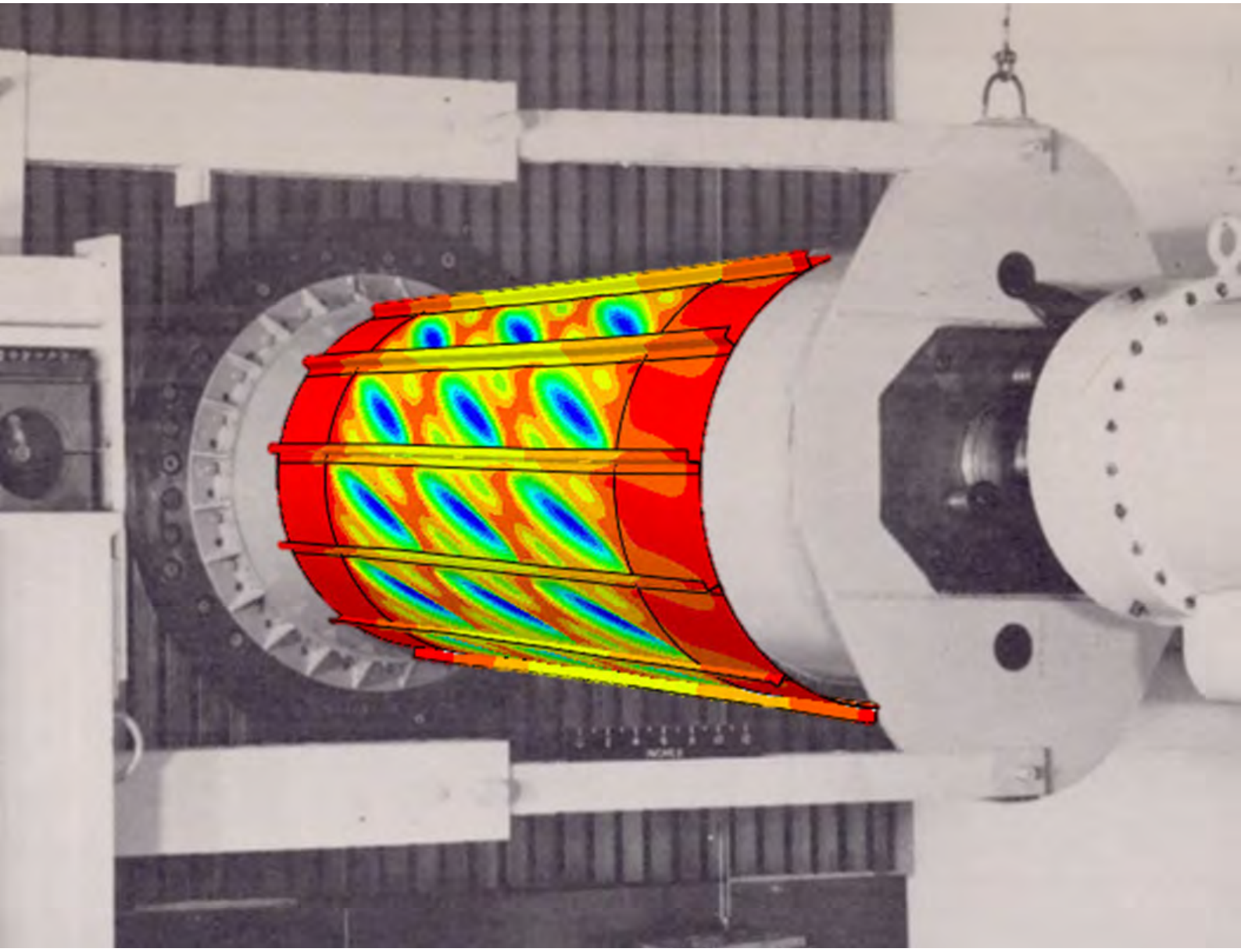

TU Delft

Fokker

GKN AEROSPACE

Post buckling of curved skin-stiffened metal panels under shear loading

An investigation using virtual testing

by

Ayush Prasad

to obtain the degree of Master of Science

at the Delft University of Technology,

to be defended publicly on Thursday August 29, 2024 at 09:30 AM.

Student number:	5803306	
Project duration:	November 7, 2023 – August 29, 2024	
Supervisors:	Dr.-Ing. S. (Saullo) G.P. Castro	TU Delft
	Dr. B. (Bas) H. A. H. Tijs	GKN Fokker Aerospace B.V.
	Eng. S. (Silviu) Rogozea	GKN Fokker Engineering Romania
Thesis Committee:	Dr. D.M.J. (Daniël) Peeters	TU Delft
	Dr. C.D. (Calvin) Rans	TU Delft

This thesis is confidential and cannot be made public until August 31, 2026.

Cover:	Virtual testing result superimposed on the picture of the experimental setup used at NACA
Style:	TU Delft Report Style, with modifications by Daan Zwaneveld

An electronic version of this thesis is available at `http://repository.tudelft.nl/`.


Fokker


TU Delft


GKN AEROSPACE

Preface

This thesis marks the completion of my MSc in Aerospace Engineering at TU Delft. Looking back, I remember being overjoyed about joining this program, and I came with the goal to learn in-depth about aerospace structures from one of the best faculties in the field. In the first year, I pushed myself to learn and understand complex topics through the courses offered by the faculty, and structural analysis became something in which I became most interested. So, when the opportunity presented itself with an internship about the analysis of flat diagonal tension panels at GKN Fokker, I immediately grabbed it. I enjoyed my work there and wanted to continue my work into the more challenging case of curved diagonal tension, which culminated in me taking on the thesis that is presented here.

This thesis has been an incredible learning experience and also has been a very challenging endeavor which would not have been possible without the excellent support that has been provided to me by my supervisors. Their guidance on technical topics and encouragement has been invaluable in completing this thesis. Specifically, I would like to thank Saullo for his excellent guidance on the scientific content and the writing of the thesis, in addition to his help on specific technical problems. Bas, who was also my supervisor during my internship, has immensely helped me in setting up the thesis topic and providing invaluable help with setting up the virtual testing model. Finally, I would like to thank Silviu, who has really challenged me on my explanations of the results, enabling me to develop a better understanding of the effects of diagonal tension.

I would like to extend my gratitude to my friends at TU Delft (especially Tejas, Claudia, Nathan, Kubra, Nico, Malolan, Vin, Najeeba, and Aamir) who have really supported me through the challenges in both the academic and personal realms. Finally, I would like to thank my parents and my sister who have given me their unwavering support during this time like they have throughout my life, which gives me the courage to take on any challenges that are thrown my way and enables me to chase my dreams and passions.

The time here in Delft has been an incredible experience where I have grown both as a person and as a student and engineer. The journey of the last two years gives me confidence to take on new challenges, both as a professional and as a person, that may come my way in the future.

Ayush Prasad
Delft, August 2024

Summary

The established theory of diagonal tension (i.e., post-buckling of skin-stiffened structures under shear load) for curved skin is based on experiments conducted on stiffened cylindrical shells at NACA in the 1940s-50s. However, the experiments were unable to capture all aspects of the phenomenon, leaving knowledge gaps in the understanding of the local distribution of the compressive loads generated on the stiffener, which were filled using the theory of diagonal tension for flat skins. Furthermore, due to the limitations of the time, the secondary bending effects on the stringers were not captured well.

This MSc thesis attempted to fill this gap by performing virtual tests using non-linear finite element modelling, which is enabled by the significant improvements in computational hardware of today. A virtual testing framework is developed based on the stiffened cylinders tested at NACA using the ABAQUS finite element modelling software. The skin and the stringers are modelled using continuum shell elements and the rivets are modelled using point-based fasteners. Furthermore, the generation of the models were parameterised using python scripting with provisions to model imperfections on the cylinders in the shape of the buckling eigenmodes. To validate the modelling framework, FE models of 8 cylinders were created and the results were compared with experimental data. Satisfactory correlation was found between the virtual testing results and the experimental results given the under-reported experimental data and the unknown imperfections in the original test

A custom post-processing method was developed that was able to capture the axial and bending loads that were generated in the stringers, which were used to develop a more detailed understanding of the load-transfer mechanism under diagonal tension. The results were also compared with the semi-empirical design method and the theory of diagonal tension, and significant discrepancies were found pertaining to the local variation of the axial loads and the secondary bending of the stiffeners.

Contents

Preface i

Summary ii

1 Introduction 1

2 Literature Review 4

2.1 Buckling . . . 4

2.1.1 Compression Buckling . . . 4

2.1.2 Shear Buckling . . . 5

2.1.3 Combined Shear and Compression Buckling . . . 7

2.2 Post-Buckling of Skin-Stiffened Panels . . . 9

2.2.1 Compression Loading . . . 9

2.2.2 Shear Loading . . . 10

2.2.3 Combined Loading . . . 14

2.3 Discussion and Research Questions . . . 15

3 Virtual Testing Framework 19

3.1 NACA Test Campaign . . . 20

3.2 Finite Element Modelling . . . 22

3.2.1 Modelling the Geometry . . . 22

3.2.2 Joint between the stiffeners and the skin . . . 26

3.2.3 Material Model . . . 27

3.2.4 Boundary Conditions . . . 28

3.2.5 Solution Procedure . . . 30

3.2.6 Modelling Geometrical Imperfections . . . 30

3.2.7 Extraction of Stresses . . . 30

3.3 Implementation of the Framework . . . 31

4 Results and Validation 32

4.1 Results for a typical non-linear analysis . . . 33

4.1.1 Stringer Stresses . . . 36

4.1.2 Ring Stresses . . . 39

4.2 Effect of Imperfection . . . 41

4.2.1 Loading Curve . . . 43

4.2.2 Effect on the Stiffener Stresses . . . 43

4.3 Other important effects . . . 49
4.3.1 Effect of constraining axial contraction of the cylinder . . . 49
4.3.2 Sensitivity of ring stresses to the positioning of extraction location . . . 54
4.4 Discussion and Validation . . . 55
4.4.1 Validation of Ring Stresses . . . 55
4.4.2 Validation of Stringer Stresses . . . 56
4.4.3 Remarks . . . 56

5 Loading of the Stiffeners under Diagonal Tension 59
5.1 Post-Processing Approach . . . 59
5.2 Analysis of Primary Loads . . . 62
5.2.1 Stiffener Axial Loads . . . 64
5.2.2 Understanding the load transfer mechanism and local variations . . . 72
5.2.3 Comparison with Semi-Empirical Method . . . 74
5.2.4 Remarks . . . 78
5.3 Analysis of Bending of Stiffeners . . . 79
5.3.1 Stringer Radial Bending . . . 82
5.3.2 Stringer In-Plane Bending . . . 88
5.3.3 Ring Radial Bending . . . 89
5.3.4 Ring In-Plane Bending . . . 90
5.3.5 Remarks . . . 91

6 Conclusion 93
6.1 Answers to the Sub-Questions . . . 93
6.2 Concluding Remarks . . . 95
6.3 Recommendations for future work . . . 96

References 98

A Stress Extraction Location Nomenclature 102

B Selection of Modelling Parameters 104
B.0.1 Effect of modelling the doubler using the skin feature . . . 104
B.0.2 Effect of Modelling Rivets . . . 106

C Mesh 109
C.1 Mesh Convergence Study . . . 109
C.2 Discussion on convergence of Extracted Loads . . . 110

D Graphs: Secondary Bending Distributions 115

E Graphs: Skin Section Force Distributions 122

1

Introduction

The design of modern aircraft air-frame is dominated by the use of skin-stiffened structures that have to be as light as possible because because a higher weight of the aircraft increases the fuel consumption, which limits the range and the payload-carrying capacity of the aircraft. These structures are made of a thin skin supported by stiffeners which are beam-like structures. The skin provides the aircraft its aerodynamic profile. The aerodynamic loads generated on the skin then get distributed into the stiffeners. The structure has to handle the loads without permanent deformation under the limit loads in flight and without collapse under the ultimate loads. The trade-off between strength and weight means that these structures are heavily optimised, which in turn means that the stringers and skins are designed to be thin which makes their stability a concern.

When a structure is loaded to have high-enough compressive loads, it can buckle, which is a change in the stable equilibrium condition, usually characterised by a sudden change in the shape, typically in the transverse direction to the load application and also with a corresponding reduction in the stiffness of the structure. Typically, aircraft structures are designed so that no buckling occurs during operational loads. For the stiffeners, indeed any buckling as a column is catastrophic because beam structures lose their load bearing ability and undergo large deformation until material failure occurs. However for shells both flat and curved, there may be considerable stiffness and load-bearing ability after buckling. Especially, in the case when the shell is supported by stiffeners in the loading direction, the post-buckled load-bearing ability is even better. Usually, when a structure is designed to be stability critical, this possibility of utilising the residual post-buckled strength is neglected. Thus, allowing for the skin to buckle allows for further optimisation and weight-reduction. So, indeed there have been aircraft designs that allow the skin to buckle in some load cases for example for the B-52 aircraft for which the skin of the forward fuselage buckles under its own weight when it is depressurised and on ground.

A skin can buckle under compression, under shear or in combination of them. Due to the complicated loading conditions of any given aircraft panel, it is often that it is the case of combined shear and compression that causes buckling. Furthermore, the skin in aircraft is more often than not, curved rather than flat. This means that the case of a curved skin stiffened panel loaded under combined shear and compression is a common design case. So, to design against this load case while allowing post-buckling, accurate analysis techniques are needed. The established theory on this topic was developed by Kuhn et al [1] where the theory of ”diagonal tension” is established. Diagonal tension refers to the load transfer along the tension diagonal of the skin after it buckles under the presence of shear loads. The diagonal tension effect loads the stiffeners under compression and Kuhn et al developed a semi-empirical method to analyse the loads and the failure.

The theory developed by Kuhn et al is empirical in nature and is more extensively developed for the case of pure shear loading and borrows heavily from the theory of diagonal tension in flat skins, which is even more experimentally validated, as will be seen in the literature review chapter. Other analysis techniques that may be used to analyse the structure are semi-analytical approaches and the finite element method (FEM). The earlier uses a superposition of shape functions, typically trigonometric functions or polynomials, to approximate the deformation field that satisfies the boundary conditions, after which the contributions of all shape function coefficients are calculated to satisfy the equilibrium condition. These methods have found extensive use in the linear and non-linear analyses of unstiffened cylinders and cones [2, 3]. Additionally, there are also methods that account for axially oriented stiffeners [4] by modelling them as plates. These methods offer theoretical solutions with lower computational expense than FEM, however, they can become inconvenient to implement for complicated problems such as the one herein addressed, consisting of full thin-walled structures containing multiple shell domains and stiffeners in both axial and horizontal direction, which requires accurate modelling of load transfers. For such cases, there are semi-analytical techniques to handle multiple domains, such as the multi-domain approach proposed by Castro and Donadon [5], however these techniques become computationally expensive for nonlinear analyses, because the full local stiffness matrix for a given domain must be calculated for each integration point, in contrasting with the convenient local support enabled by FEM. Furthermore, FEM can handle practically any problem given that enough elements and the correct kinematics are used.

The computation expense of using FEM to analyse post-buckled structures makes it prohibitive for use in the initial design and sizing of the structures, so the semi-empirical method is used for this purpose. However, as it will be clear from the literature review, the semi-empirical method is validated for limited design space for the pure shear case and an even smaller set of experiments for the case of shear combined with compression. Furthermore, the limitations of conventional tests leave some knowledge gaps. So, a clever way to utilise the finite element method is to perform ”virtual tests” on diagonal tension panels to fill in these gaps and possibly expand the design space on which the semi-empirical method may be applicable. To this end,

this thesis project aims to establish a validated virtual testing framework based on experiments conducted at NACA. The developed framework will be used to recreate 8 cylinders originally tested by kuhn et al [6] and validate them with experimental observations, which will then be used to gain more insights into the load transfer mechanism in diagonal tension panels.

This report documents the work done in the thesis and is arranged as follows. Chapter 2 presents a detailed literature review of the analysis techniques used for post-buckled skin-stiffened panes with a focus on diagonal tension. The research gaps are identified and the research objectives and questions are formulated. Chapter 3 details the development of the FE model in ABAQUS. The results from the FE model are presented in chapter 4 along with comparison with experimental results and a discussion on the validation and the usability of the model is established. Finally, in chapter 5, a post-processing approach is developed to understand the load transfer mechanism in diagonal tension. The findings are concluded in Chapter 6 with a discussion on the scope of future work.

2

Literature Review

The literature review primarily looks at the developed analytical and empirical design methods for cylindrically curved skin-stiffened panels undergoing post-buckling. Emphasis is given to the pure shear loading and combined compression and shear loading. The aim of this literature review is to analyse the design methods for these panels available in literature and to find out where their applicability is questionable. To this end, experimental evidence accompanying the development of the methods are presented. In addition, other experimental and numerical studies are highlighted wherever necessary.

This chapter is arranged in the following manner. The first section introduces the mathematical formulation of the problem. The second section summarises the buckling prediction methods followed by a summary of the design methods for post-buckling in the third section. Finally, the literature review is summarised and the research questions are formulated.

2.1. Buckling

2.1.1. Compression Buckling

First solutions for the buckling load of curved isotropic panels were developed by Timoshenko [7] in 1936 and Redshaw [8] in 1938. They solved the Kirchhoff-Love equations with simply supported and clamped boundary conditions approximately. They either let the solution satisfy the boundary conditions or the equilibrium equation. Batdorf et al [9] solved the problem exactly for long panels with transverse curvature. However, due to the imperfection sensitivity of the curved panels, the experimental buckling loads were considerably lower, thus, empirical design curves were generated in this paper to account for it. The results were modified for a finite shell in [10] and the following expression was established for the critical buckling stress (also presented in [11]):

$$\sigma_{cr} = \frac{k_x \pi^2 D}{b^2 t} \tag{2.1}$$

where,

b = smaller dimension of the rectangular plate (measured along the arc for curved edge)

t = thickness of plate

D = flexural stiffness per unit length = $\frac{Et^3}{12(1-\nu^2)}$

E = Young's modulus

ν = Poisson's ratio

k_x = Critical compressive stress coefficient (referred as k_c in [11])

For both boundary conditions, graphs were generated for k_x as a function of a curvature parameter (Z) defined as:

$$Z = \frac{b^2}{rt}\sqrt{1-\nu^2} \tag{2.2}$$

where,

r = radius of curvature of panel

The theoretical and empirical curves for k_x are shown in Figure 2.1. It was found that at higher curvatures, the boundary conditions do not affect the buckling loads. To get the empirical curves at moderate and high Z values, the the theoretical curve was modified. The critical compressive stress coefficient was expressed as $k_x = CZ$ where C was an empirically determined constant that is given by $C = 0.68 - 0.0005\frac{r}{t}$. The k_x established by this method tends to the value of 4 as Z decreases, which is the coefficient for a flat plate under simply supported boundary conditions. To generate the empirical curves for clamped boundary conditions, a smooth transition was drawn between the theoretical value for low curvatures (little effect of imperfections) and empirical values for moderate and higher curvatures (where the boundary condition does not matter).

In addition to these design methods, to get theoretically exact buckling loads, Semi analytical models could be used. Wilkins [12] formulated the problem using Vlasov's strain kinematics [13] to solve for the buckling loads of orthotropic curved plates using the Ritz method under any combination of shear and compression loads. The model was capable to handle simply supported, clamped and elastically restrained boundary conditions. Furthermore, it was able to also take into account the stiffeners, formulated as beams.

2.1.2. Shear Buckling

The problem of shear buckling of curved isotropic plates was studied by Leggett [14], who developed solutions for clamped and simply supported boundary conditions for slightly curved shells. Kromm [15] developed solutions for an infinitely long plate with simply supported edges for all curvatures. Batdorf et al [16] created a theoretical solution for long plates with any transverse curvature. Subsequently, they developed a theoretical closed form solution for

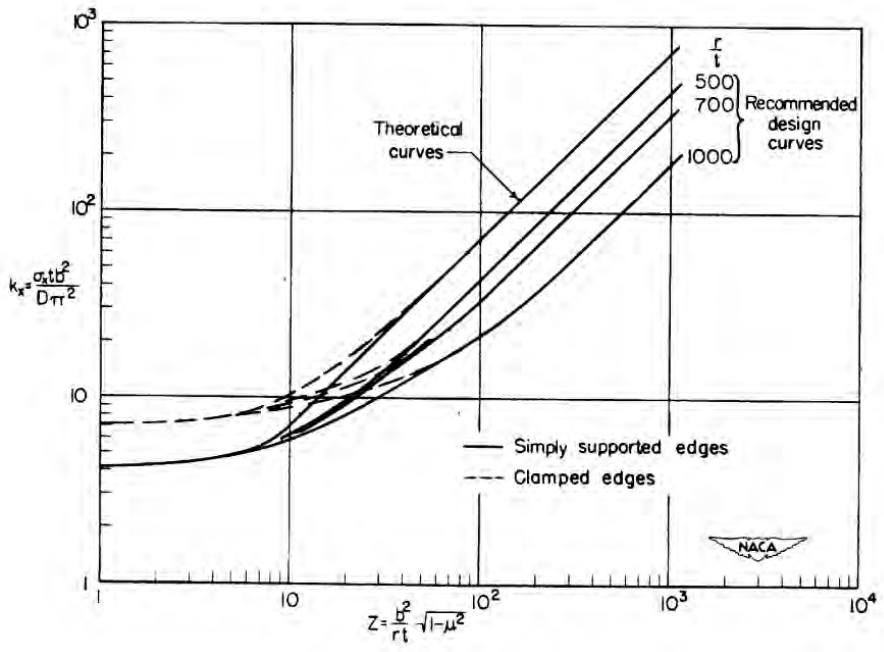

Figure 2.1: Theoretical and empirical values of the critical compressive stress coefficients for cylindrically curved plates loaded in axial compression [10]

simply supported rectangular plates with any curvature along one side [17] and an estimate of the theoretical curve of the same with all sides clamped. They proposed a closed form expression for critical shear stress:

$$\tau_{cr} = \frac{k_s \pi^2 D}{bt^2} \tag{2.3}$$

where,

k_s = Critical shear stress coefficient

For both boundary conditions, graphs were generated for the critical shear stress coefficient (k_s) as a function of the curvature parameter Z. The graphs were calculated theoretically for simply supported boundary conditions and estimated for clamped boundary conditions. For the estimation, known theoretical critical shear coefficients for cylinders [18] and infinitely long curved panels [16] under clamped boundary conditions were extrapolated. This theory was used for the prediction of post-buckling behaviour of curved panels by Kuhn et al [1]. They suggested using the simply supported curves as it was found to be in better agreement with experimental data and also for the cases where the critical shear was measured through the appearance of compressive stresses in the stiffeners. However, they remarked that for low curvatures, empirical restraint coefficients should be used to account for the restraint that the stiffeners provide to the panel.

The theoretical buckling stresses from Batdorf et al's solution [17] were computed for the simply supported boundary condition and then compared with experimentally determined values.

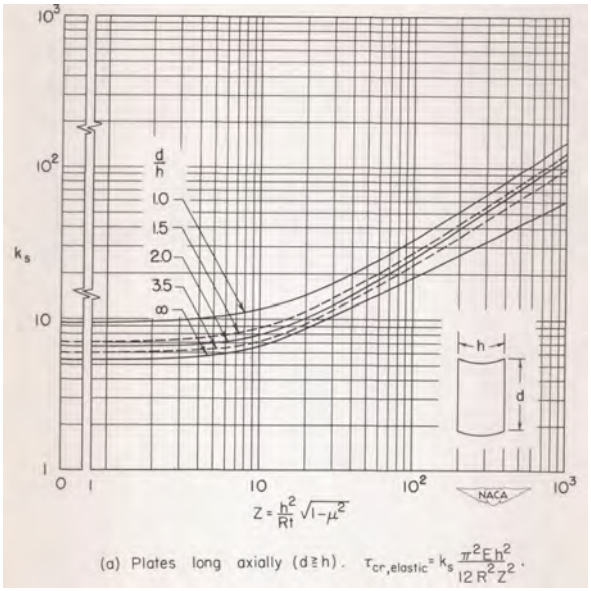

(a) Critical shear stress coefficient for axially long plates

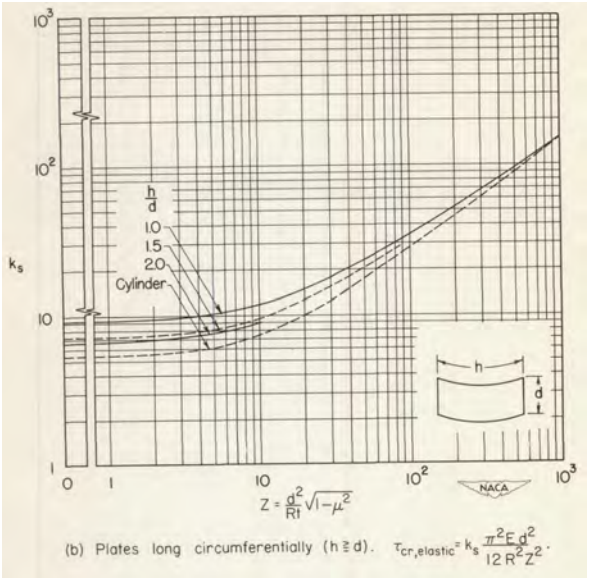

(b) Critical shear stress coefficient for circumferentially long plates

Figure 2.2: Critical shear stress coefficients (taken from [1])

The accuracy of the load depended on how the buckling load was measured. Buckling loads recorded when the buckle patterns are visible on any panel of a multi-panel specimen were found to be considerably lower than theoretical prediction. However, for experimental observations made such that the measured buckling load was less sensitive to initial imperfections, the agreement was found to be much better, although still lower than predictions. These observations were made by identifying the point where the torque-twist curve deviates from the initial straight line or from panels that had small initial imperfections. Considering the second set of experiments, the study concluded that the theoretical values are a valid estimate of the buckling load. The conclusion drawn from the second set of tests led to the developed theoretical curves being used as design curves for curved isotropic plates (for example in [11]). However, the first set of observations do indicate significant imperfection sensitivity. In a more recent study by Amani et al [19] using non-linear FE simulations, the imperfection sensitivity of the buckling load for curved plates under uniform shear was found to be significant. The study concluded that the shear design curves significantly over-predict the buckling load of imperfect and mildly to highly curved plates.

2.1.3. Combined Shear and Compression Buckling

The seminal work on the combined load case was presented by Schildcrout and Stein [10] where the modified Donnell's equations were solved exactly for simply supported isotropic panels with different circumferential to axial length ratios and curvatures. Curves were generated between the critical axial and critical shear coefficients (k_x and k_s) as defined in Equation 2.1 and Equation 2.3. The same equations were solved in a previous study by Batdorf et al [16] for panels with long axial dimension and it was noted that the curve between k_s and k_x are almost parabolic and the following interaction curve was proposed for the critical combination

of shear and axial stresses:

$$(R_s)_{th}^2 + (R_x)_{th} = 1 \tag{2.4}$$

$$(R_s)_{th} = \frac{\tau}{(\tau_{cr}^0)_{th}} \tag{2.4a}$$

$$(R_x)_{th} = \frac{\sigma}{(\sigma_{cr}^0)_{th}} \tag{2.4b}$$

where:

$(R_s)_{th}$ = theoretical shear interaction factor
$(R_x)_{th}$ = theoretical compression interaction factor
τ = applied shear stress
σ = applied axial stress
$(\tau_{cr}^0)_{th}$ = theoretical critical shear stress under pure shear loading
$(\sigma_{cr}^0)_{th}$ = theoretical critical axial stress under pure compression loading

In both the papers it was noted that since moderately or highly curved shells buckle at considerably lower loads, the interaction curve should be modified to account for this. This is done by using an experimental compression interaction factor to develop an empirical interaction curve as follows:

$$(R_s)_{th}^2 + (R_x)_{exp} = 1 \tag{2.5}$$

$$(R_x)_{exp} = \frac{\sigma}{(\sigma_{cr}^0)_{exp}} \tag{2.5a}$$

where:

$(R_x)_{exp}$ = experimental compression interaction factor
$(\sigma_{cr}^0)_{exp}$ = experimental critical axial stress under pure compression loading

For design purposes, using empirically determined values of k_x (as shown in Figure 2.1) in Equation 2.4 would yield results close to experiments as the empirical curve would provide a good approximation of $(R_x)_{exp}$. The above discussion was based on theoretical results for simply supported panels. However, the conclusions on the shape of the interaction curve were extended to clamped plates because for appreciably curved plates, the buckling loads for clamped boundary conditions are equal or slightly higher than the loads for simply supported boundary conditions. Thus, the interaction curves may be used similarly for clamped boundary conditions. The empirical interaction curves (modified to use $(R_s)_{exp}$) were compared with experimental data and good correlation was found. The interaction curve is also described in [11].

2.2. Post-Buckling of Skin-Stiffened Panels

This section reviews the semi-empirical methods developed for analysing the post-buckling response and failure of metal and composite panels and the tests used to establish them. In addition, other studies important in this field are highlighted.

2.2.1. Compression Loading

For a stiffened plate under compression loading, the load applied in excess of the critical load does not get applied uniformly along the edge. Due to the reduced in-plane stiffness of the skin towards the midpoint between the stringer axes, the skin near the stiffeners is more highly loaded than the middle. Consequently, the stringers take a greater share of the total load. For design purposes, an effective width is defined in literature [20, 11, 21]. It is the width (w_e) of an equivalent plate that carries the total load on the skin when a uniform stress of magnitude equal to the maximum stress on the post-buckled configuration (σ_{se}) is applied on it. It can be mathematically expressed as (refer Figure 2.3),

$$w_e \sigma_{se} t = t \int_{-0.5b}^{0.5b} \sigma_c \, dx \tag{2.6}$$

Analytical expressions for the effective width for flat isotropic skins were developed by von Karman and Sechler [22] using an analytical solution of von Karman equilibrium equations for an isotropic plate under compression. However, these proved to be inaccurate due to effects of plasticity. Marguerre [23] developed an empirical relation for the effective width in the case of flat plates. ANC-5 [24] provided design equations for the same. Sechler [20] adopted them for use in curved skins. The relation is given by:

$$\frac{w_e}{w} = 0.89 \sqrt{\frac{\sigma_{cr}}{\sigma_S}} \tag{2.7}$$

where σ_S is the compressive stress in the stiffener. Bruhn [11] also suggests an empirical relation, which is a modified version of the analytical expression given by Karman and Sechler. This expression was modified by and also adopted for use by Deo et al. [25, 26] on composite curved skins. It is expressed as follows:

$$w_{eff} = 1.9t \sqrt{\epsilon_S} \tag{2.8}$$

where ϵ_S is the strain in the stiffeners.

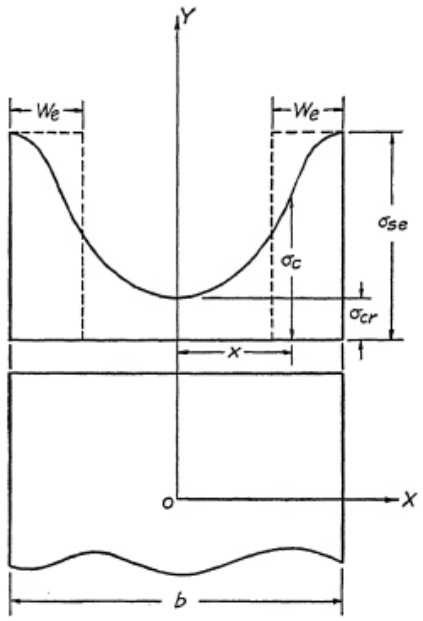

Figure 2.3: Effective width of a post-buckled plate under compression (taken from [20])

2.2.2. Shear Loading

The earliest work on the post-buckling behaviour of cylindrically curved rectangular skin-stiffened isotropic panels was undertaken by Wagner [27]. He analysed the post-buckling tension field in the web and derived an expression for the angle of diagonal tension (the angle at which the post-buckled web transmits tensile loads) with the assumption that the buckling load is so small that it is negligible. He classified the problems into two cases: panels long axially (defined by $b < \frac{1}{3}r$) and panels long in the circumferential direction (defined by $a < \frac{1}{3}r$). In the earlier case, the skin tries to flatten into the plane defined by the two axial stiffeners (stringers). In the latter case, the skin deforms into a hyperboloid revolved around the axis of curvature. For both the case, the extra compressive strain in the skin along the circumferential direction was calculated. This work was further continued by Kuhn and Griffith [28] to develop the engineering theory of diagonal tension to be used in design (also summarised in [1]). This theory also inherits from the engineering theory of diagonal tension in flat panels (summarised in [1]) which was extensively validated with experiments. The theory for curved webs is summarised in the upcoming paragraphs.

It was noticed experimentally that the skin was able to transmit loads through pure shear action after buckling, a phenomenon also present for flat webs. Thus, in this state of ”incomplete diagonal tension” as defined in the study, the applied stress was decomposed into stress that is transmitted through pure shear action and stress that is transmitted through the diagonal tension action. It was mathematically expressed as follows:

$$\tau = \tau_{PS} + \tau_{DT} \tag{2.9}$$

where τ_{PS} and τ_{DT} are the shear stress transmitted through pure shear and diagonal ten-

sion action. To calculate the shear transmitted through diagonal tension action, an empirical diagonal tension factor (k) was defined as follows [28]:

$$\tau_{DT} = k\ \tau \tag{2.10}$$

$$k = \tanh\left[\left(0.5 + 300\frac{ta}{rb}\right)\log_{10}\frac{\tau}{\tau_{cr}}\right] \tag{2.11}$$

Equation 2.11 is a modification to the empirically determined expression for the flat web case. The term "$300\frac{ta}{rb}$" accounts for the fact that diagonal tension develops faster in curved webs, where a is the axial length of the curved plate. The stringers and rings are loaded only due to the diagonal tension load transfer. The tension diagonals try to pull adjacent stringers and rings towards each other, which thus loads the rings and stringers respectively under compression. The average stresses in the stiffeners can be calculated using the following formulae given by Kuhn [28, 1]:

$$\sigma_{ST} = -\frac{k\tau\cot\alpha}{\frac{A_{ST}}{at} + 0.5(1-k)} \tag{2.12}$$

$$\sigma_{RG} = -\frac{k\tau\tan\alpha}{\frac{A_{RG}}{dt} + 0.5(1-k)} \tag{2.13}$$

where:

σ_{ST} = Stress in the stringer

σ_{RG} = Stress in the ring

α = Angle of diagonal tension

A_{ST} = Cross section area of stringer

A_{RG} = Cross section area of ring

The above formulae were derived by calculating the compressive forces created by the diagonal tension action and dividing it by the area that bears the load. The term "$0.5(1-k)$" accounts for the fact that there will be some effective width of the skin that will be assisting in the load transfer along the stiffeners. The effective width along the circumferential direction (b_{DT}^{eff}) or axial direction (a_{DT}^{eff}) can be defined as:

$$\frac{b_{DT}^{eff}}{b} = \frac{a_{DT}^{eff}}{a} = 0.5(1-k) \tag{2.14}$$

Equation 2.14 is taken from the design method developed for flat skins. Even in that case, the expression is based on the assumption that the effective width is proportional to the amount of pure shear transmitted by the skin (thus the proportionality with $(1-k)$). The assumption of half the width of the bay as the effective width right after buckling comes from assuming a sinusoidal distribution of compression stresses on the skin. Nevertheless, use of this expression was found to prevent extreme conservatism in the stiffener stress predictions than just

using the area of the stiffeners. In the case that the ring is designed to be floating, the effective width term should be removed. It is to be noted that the stresses given by Equation 2.13 and Equation 2.12 are average over the edges of the skin panels. In reality, there would be variation in the stresses along the length of the stiffeners. This effect was seen in flat webs, where due to the lower buckling deformation of the skin near the edges of the bays, the effective width effect is higher and thus the compression stress is lower at the ends and higher in the middle. To account for this, correction factors were developed empirically for flat webs. For curved webs, the same correction factors found their use in both the NACA method and the method developed by Deo et al [26]. However, the effective width could not be determined and validated due to the inability to separate the secondary loading effects in the experimental campaign for curved webs. For the correction factor, the NACA method provides an design graph, and the same correction factor is expressed using a mathematical expression by Deo et al, where they used it to find the maximum axial strain with respect to the average axial strain. Modifying this correction factor for stresses (considering linear relationship between stress and strain), the maximum stress in the stiffeners is given by multiplying Equation 2.13 and Equation 2.12 by the correction factor as follows:

$$\sigma_{ST}^{max} = \begin{cases} \sigma_{ST}\left(1 - 0.775(1-k)\left(1 - 0.8\frac{b}{a}\right)\right) & \text{if } a > b \\ \sigma_{ST}\left(1 - 0.775(1-k)\left(1 - 0.8\frac{a}{b}\right)\right) & \text{if } b > a \end{cases} \tag{2.15}$$

$$\sigma_{RG}^{max} = \begin{cases} \sigma_{RG}\left(1 - 0.775(1-k)\left(1 - 0.8\frac{b}{a}\right)\right) & \text{if } a > b \\ \sigma_{RG}\left(1 - 0.775(1-k)\left(1 - 0.8\frac{a}{b}\right)\right) & \text{if } b > a \end{cases} \tag{2.16}$$

Equation 2.13 and Equation 2.12 depend upon the angle of diagonal tension (α). Wagner [27] modified his work on flat panels to include the tendency for axially long webs to flatten and circumferentially long webs to deform into a hyperboloid and proposed the following expressions:

$$\tan^2\alpha = \frac{\epsilon - \epsilon_{ST}}{\epsilon - \epsilon_{RG} + \frac{1}{24}\left(\frac{b}{r}\right)^2} \qquad \text{if } b < \frac{1}{3}r \tag{2.17}$$

$$\tan^2\alpha = \frac{\epsilon - \epsilon_{ST}}{\epsilon - \epsilon_{RG} + \frac{1}{8}\left(\frac{a}{r}\right)^2 \tan^2\alpha} \qquad \text{if } a < \frac{1}{3}r \tag{2.18}$$

The terms "$\frac{1}{24}\left(\frac{b}{r}\right)^2$" and "$\frac{1}{8}\left(\frac{a}{r}\right)^2 \tan^2\alpha$" account for the excess compressive strains due to the flattening and the deformation into a hyperboloid of the web in the two respective cases. For practical use, Equation 2.17 may be used when $a > b$ and Equation 2.18 may be used when $b > a$. The strains ϵ, ϵ_{ST} and ϵ_{RG} are the strain in the web along the tension diagonal, the strain in the stringer and the strain in the rings respectively. The latter two can be calculated

by dividing the corresponding stresses by the young's modulus:

$$\begin{aligned} \epsilon_{ST} &= \frac{\sigma_{ST}}{E} \\ \epsilon_{RG} &= \frac{\sigma_{RG}}{E} \end{aligned} \tag{2.19}$$

The expression for the strain along the diagonals can be calculated by the following expression [28]:

$$\epsilon = \frac{\tau}{E}\left[\frac{2k}{\sin 2\alpha}(1-k)(1+\nu)\right] \tag{2.20}$$

Equation 2.20, Equation 2.19, can be solved with Equation 2.17 or Equation 2.18 to calculate the angle of diagonal tension and the stresses in the stiffeners. If it is assumed that the buckling happens at an infinitesimally small load (Pure Diagonal Tension assumption) and there is no effective width effect, the above equations can be combined into a transcendental equations in α [1]:

$$(1+R_R)\tan^4\alpha + A\tan^3\alpha = 1 + R_S \text{ if } \qquad (h > d) \tag{2.21}$$

$$B\tan^5\alpha + (1+R_R)\tan^4\alpha = 1 + R_S \text{ if } \qquad (d > h) \tag{2.22}$$

where:

$$A = \frac{1}{24}\left(\frac{b}{r}\right)^2\frac{E}{\tau} \quad ; \quad B = \frac{1}{8}\left(\frac{a}{r}\right)^2\frac{E}{\tau}$$

$$R_R = \frac{bt}{A_{RG}} \quad ; \quad R_S = \frac{at}{A_{ST}}$$

Kuhn et al [1] also analyse secondary stresses on the stiffeners. In the special case of floating rings, the hoop compression is introduced by radial loads transferred at the stringers. So, there will be a primary peak in bending moment at the stringers and a secondary moment midway between the stringers, having half the magnitude. The magnitude of the primary peak was calculated to be:

$$M_{RG} = k\tau t\frac{b^2 a}{12r}\tan\alpha \tag{2.23}$$

For panels longer axially, there should be a radial force distributed on the stringers when the panels buckle and flatten which would load them to bend inwards as a beam supported on two ends. Assuming uniform distribution of this load, there will be a peak moment at the joint with the rings and a secondary moment midway between two rings with half the magnitude. The primary peak was calculated to be:

$$M_{ST} = k\tau t\frac{ba^2}{12r}\tan\alpha \tag{2.24}$$

However, Kuhn et al observe that the radial distributed load would not be uniform for several reasons. The tension diagonals would not change their directions near the rings as the ring

would force the skin around it to follow its curvature. This would result in lower radial distributed near the rings. This combined with the sagging of the stringers and the rings and the non-uniformity of skin stresses, make the assumption of uniformly distributed load invalid.

The accuracy of the primary stresses were evaluated by comparing with experiments with webs designed at the extreme cases of the usual design space (Summarised in [6]). It was found that the measured stresses in the usual design space were reasonably close to the predictions. Additional cylinders were tested towards the extremes of the design space. The predictions were inaccurate for some cases but the inaccuracies were on the conservative side. So, reliability is ensured in the usual design space. For the secondary stresses, very few attempts had been made to measure the moments through strain measurements (section 9.4 of [1]) because the effective width is not known with accuracy and as a consequence, the separation of bending and axial stresses is not practical. In the few experiments that did look into the secondary stresses, it was found that the maximum moments are no larger than the secondary peaks. So, it was suggested to use half the moment given by Equation 2.24 for both primary and secondary peaks for both the rings and the stringers.

The expression for average stress in the stringer was compared with test data extracted from 12 metal cylinders stiffened with varying number of rings and stringers and loaded in torsion [28, 29] (Summarised in [6]). For cylinders lying in the usual design range showed acceptable agreement with the theory. Some cylinders had extreme design parameters to test the theory to the limits of the design space. For these cylinders, there was a significant deviation. However, it was on the conservative side.

2.2.3. Combined Loading

Literature for closed form analytical solutions could not be found, presumably due to the complexity of the governing equations. However, semi empirical methods for predicting the response of the skin and the loads in the stiffeners were developed by Kuhn et al [1] for metal webs and extended by Deo et al [30, 31, 32, 33] for composite webs.

The methods for shear-only and compression-only loads were combined to predict the post-buckling behaviour for the combined load case. To calculate the shear stress transferred by diagonal tension action, the expression of k (Equation 2.11) was used with the shear stress for the critical combination of compression and shear. Kuhn et al did not suggest any modification for the analysis of stresses in the web as compared to pure-shear loading. It was assumed that the compression would not have any major effect on the failure. However, no validation was attempted for this. Deo et al mention that skin rupture failure mode must account for the interaction of the interaction of the stresses developed. Nevertheless, both groups of researchers provide a more detailed analysis method for the stiffener failure modes. For the rings, Kuhn et al suggest using Equation 2.13. Although they note that there should be in theory a modification to the the effective width due to the effect of compression. The stresses for the stringers are calculated by adding the stress due to the compression load and the stress due

to the diagonal tension effect. For both the stresses, the effective widths are modified to take into account the combined loading. In the method by Kuhn et al, effective width in compression given by Equation 2.7 is multiplied with the compression interaction factor (R_x) and the effective width for shear is multiplied with the shear interaction factor (R_s). The expression for stress is given by:

$$\sigma_{ST} = -\frac{P}{n(A_{ST} + btw_{eff}R_x)} - \frac{k\tau \cot\alpha}{\frac{A_{ST}}{bt} + 0.5(1-k)R_s} \tag{2.25}$$

The maximum stress is calculated using the same correction factor used for the case of pure shear loads.

Deo et al used the similar expression however they used Equation 2.8 for the compression buckling effective width and did not modify it for the combined load case and defined it in terms of strain. The final expression for the total stringer strain, ϵ_{ST} would be a combination of the strain due to compressive loading, ϵ^c_{ST} and shear loading, ϵ^s_{ST}:

$$\epsilon_{ST} = \epsilon^c_{ST} + \epsilon^s_{ST} = -\frac{N_x b}{(EA)_{ST} + w_{eff}tE_x} - \frac{kN_{xy}\cot\alpha}{t\left[\frac{(EA)_{ST}}{bt} + 0.5(1-k)E_xR_s\right]} \tag{2.26}$$

The average section strain and the maximum compressive strain are calculated by modifying the component of stress developed by shear in the same was as done for the pure shear load case. The formula for average stress in the stringers was validated with tests on stiffened cylinders loaded in torsion and compression [34, 6]. The stresses were satisfactorily predicted for total load more than twice of the bukling load. However, just after the buckling, there is a jump in predicted stresses due to the Karman-Sechler expression for effective width under compression, which is not representative of any physical phenomenon.

2.3. Discussion and Research Questions

The literature presented in the previous section show how the semi-empirical was developed to analyse the post-buckling behaviour of curved skin-stiffened panels. Simultaneously, the comparison with the experiments was also provided. Analysing the presented literature, it can be noticed that the phenomenon of compression buckling and post-buckling of curved, stiffened panels are well developed. The semi-empirical method for buckling has been developed from a large range of tests, and accounts for the considerable imperfection sensitivity. For the post-buckling analysis, the loads on the skin and the stiffener can be analysed theoretically using the straight-forward concept of effective width, which can be calculated from analytical solutions. Furthermore, for metal panels, semi-empirical expressions exist which take into account the effects of plasticity and enable a better design method.

For shear buckling, the initial studies developed the theoretical solution by solving the Kirchhoff-Love equations, and after a considerable amount of tests, the theoretical buckling loads were presented as design curves. However, the tests did indicate a slight imperfection sensitivity, which was also found in a recent investigation using the finite element method [19]. For the

case of post-buckling, the analysis methods available in literature are only available from two sets of investigations, the first by NACA in the 1940s-1950s, and then by another group of engineers at Northrop in the 1980s. The experimental investigations are also mainly limited to these sets of investigations. Overall, the global load transfer mechanism is well understood, and the developed semi-empirical analysis method predicts the average loads on the stiffeners with decent accuracy. However, there has been little investigation into the local variation in the load transfer and the secondary loads generated on the stiffeners.

For curved panels loaded with a combination of shear and compression, a theoretical solution was calculated and an interaction curve for the critical combination of shear and compression stress was proposed based on the critical shear and compression stress. This curve was very close to the theoretical curve. However, to account for the imperfection sensitivity, the design value for the critical compression stress was used to create the design curve. For the post-buckling behaviour, the available test data is very scarce. The design method developed for this case, was validated on only one kind of test geometry. Even then, while the load predictions on the stringers were close, there were some noticeable inconsistencies with the physical response as measured in experiments.

The presented literature review reveals a significant gap in the understanding of the post-buckled behaviour of curved skin-stiffened panels under the presence of shear only and combined shear and compression loads. There is a lack of a detailed understanding of the load transfer from the skin to the stiffeners during post buckling under shear loads, especially under the presence of shear loads. The latest design methods have decent accuracy in the prediction of the average stresses in the stiffeners. However, the local variation in the axial load was not captured well in the experiments and the results for flat webs were adopted. It is known that the effective width effect changes along the length of the stiffeners which was the explanation for the local variation in the compression by Kuhn et al [1], but to the knowledge of the author, the actual variation has not been captured in any experimental or numerical investigation. Furthermore, there are secondary bending effects due to the radial loads on the stiffeners that have not been characterised well.

A lot of the unknown is due to limited number of tests performed to analyse such panels that are available in literature. Furthermore, in the tests that were performed, there are entire aspects of the load transfer that could not be studied in detail due to the limitations of an experimental test campaign, especially those run around 80 years ago. So, to address this knowledge gap, this thesis aims to create and validate a virtual testing approach using non-linear finite element method and use the models generated to gain further insights into the geometrical behavior and internal load transfer mechanism during post-buckling. In this thesis, a framework for virtual testing is developed to test stiffened cylinders under axial loading (tension or compression) and shear loading, however, the discussion is limited to/focused on pure shear loading considering available time. Thus, the research objective for this thesis can be summarised as:

To develop a virtual testing approach for post-buckled cylindrically curved

skin-stiffened structures using non-linear finite element method to characterise and understand the load transfer mechanism.

To create and validate the virtual testing approach, the experimental data from NACA [28, 6] would be recreated using non-linear finite element method. Once a validated model is achieved, it will be used to perform a detailed analysis into the load transfer mechanism between the skin and the stiffeners. To this end, the following research question was formulated:

Research Question: ***"How to develop and validate a virtual testing model for curved diagonal tension cylinders and accurately analyse the loads generated on the stiffeners?"***

Sub-questions:

1. What details are needed to be modelled to accurately recreate experimental results?
2. To what extent can the model be validated given the under-reported experimental data and how useful would that model be?
3. How to account for the unknown geometrical imperfections in the experiments?
4. What is the load transfer mechanism according to the results of virtual testing and how well do the analytical models take this into account?

The following hypotheses could be made regarding the above sub-questions based on literature and judgement:

- *For SQ1:* The aim of the model is to recreate the stresses on the stiffeners so that the model may be used for analysis of the loads on them. Also, the experimenters noted a gradual development of diagonal folds on the skin, which suggests that the tests were imperfection sensitive. So, it is hypothesised that **modelling the geometry, material and boundary conditions with accuracy is needed to recreate the stiffness and response and in addition, an imperfection model will be needed to recreate the gradual appearance of the diagonal folds.**
- *For SQ3:* From literature [19], it is known that for unstiffened shells, the buckling load is considerably imperfection sensitive. For post buckling, there is a slight sensitivity for the displacement of the shell. So, it is hypothesised that **during post buckling, there will be a slight imperfection sensitivity for the stresses on the stiffeners, which will not affect the stresses too much, especially for deep post buckling**.
- *For SQ4:* The skin alleviates some compression from the stiffeners, which can be noticed as the effective width effect, which depends on the deformation of the skin. So it is hypothesised that **the local distribution of the axial load depends upon the post-buckling deformation pattern of the adjacent panels.**
- *For SQ4:* The current semi-empirical design method extrapolates the observations for

flat panels to curved panels, so, it is hypothesised that **the local distribution of the loads is not captured well in the analytical method**.

3

Virtual Testing Framework

As laid out earlier, the goal of this thesis is to create a virtual testing framework that could be used to analyse curved skin-stiffened panels undergoing post-buckling. So, a decision had to be made on the experimental tests that would form the basis of the developed framework and that can be recreated virtually. For this, the set of tests run at NACA by Kuhn et al [28, 6] were selected. The results from these tests are well documented with the stresses on the stringers and rings being reported. Additionally, these are the tests used for the development of the semi-empirical design method reviewed in the previous chapter. Moreover, the experimenters had mentioned that certain aspects of the diagonal tension effect could not be characterised well due to the lack of resources available at the time. So, a virtual testing framework that could recreate the main observations of the experiments could also provide insights into these aspects that were not looked into in detail.

This chapter presents the development of the virtual testing framework. The chapter is split into three sections. The first would be a brief summary of the experimental testing campaign run by NACA. This would be followed by the explanation of the development of the modelling strategy. Finally, the implementation of the developed strategy using a parameterised approach is discussed

3.1. NACA Test Campaign

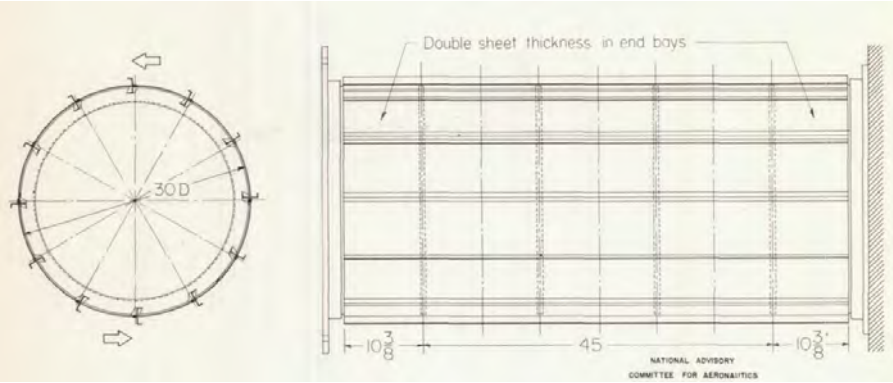

Figure 3.1: Dimensions of cylinders tested in pure torsion [28]

The main series of tests conducted at NACA to analyse the post-buckling behaviour of axially and circumferentially stiffened curved panels in pure shear loading are reported in [28]. Eight cylinders of 30 inch diameter were fabricated from 24S-T Aluminium Alloy (Al 2024-T3 in current naming scheme for Aluminium alloys). The cylinders were stiffened circumferentially with either 4 or 7 equally spaced rings and axially with 12 equally spaced stringers, all made from 24S-T Aluminium alloy and riveted to the skin. The drawing of the cylinders can be seen in Figure 3.1 and the specific dimensions for each of them can be seen in Table 3.1. The cross section of the stiffeners are shown in Figure 3.2.

Table 3.1: Dimensions of Cylinders tested under pure torsion [28]

Cylinder	Radius	Thickness			Spacing		Area	
		Stringer	Ring	Skin	Stringer	Ring	Stringer	Ring
	(inch)	(inch)	(inch)	(inch)	(inch)	(inch)	($inch^2$)	($inch^2$)
1	15.04	0.052	0.061	0.0248	7.87	15.00	0.230	0.197
2	15.03	0.050	0.064	0.0266	7.87	7.50	0.221	0.202
3	15.02	0.033	0.063	0.0265	7.86	15.00	0.155	0.198
4	15.02	0.033	0.068	0.0266	7.86	7.50	0.153	0.216
5	15.03	0.081	0.104	0.0393	7.87	15.00	0.335	0.320
6	15.05	0.080	0.104	0.0394	7.88	7.50	0.332	0.317
7	15.04	0.053	0.102	0.0428	7.87	15.00	0.239	0.318
8	15.06	0.053	0.102	0.0399	7.88	7.50	0.239	0.321

The cylinders were attached to two rigid supports at each end. One end was fixed and the other one rotated using a steel frame actuated by a hydraulic jack. It was ensured that the weight of the frame was counter-balanced so that no bending was introduced in the cylinders. The jig used can be seen in Figure 3.3 (note that the image shows a combined torsion and compression cylinder, which does not have any outer stringer). The skin at the bays at the ends (adjacent to the rigid supports) were doubled in thickness using doublers. This was done so that there is little effect of the end supports on the ”gage” section of the cylinders

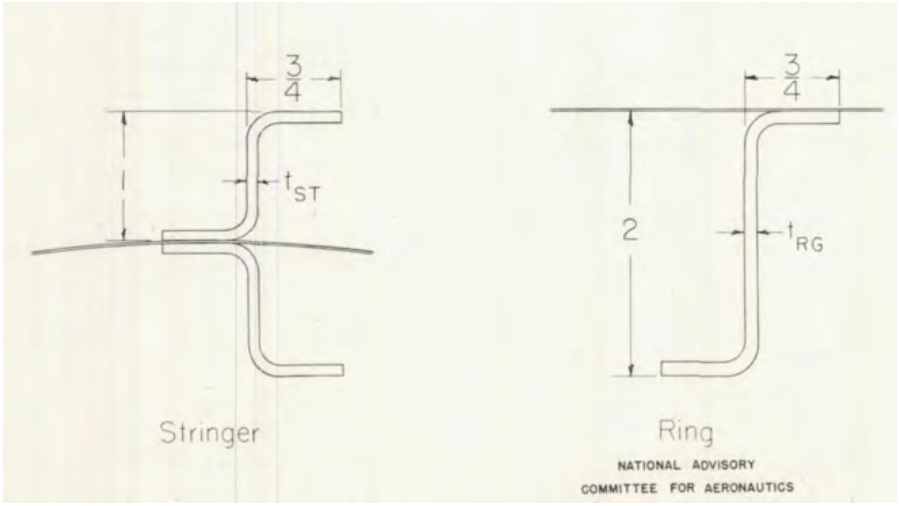

Figure 3.2: Nominal Dimensions of the stiffeners for cylinders tested in pure torsion [28]

For these set of tests, double stringers were used, which means that the stringer at each location was made by a stringer placed inside and another one placed outside the cylinder. This was done to ensure that the compression introduced into the stringers was close to the neutral axis, thus minimising any bending of the stringer due to the compression. It also enabled the experimenters to eliminate the effects of secondary bending by averaging pairs of stress readings at symmetrically located strain gauges.

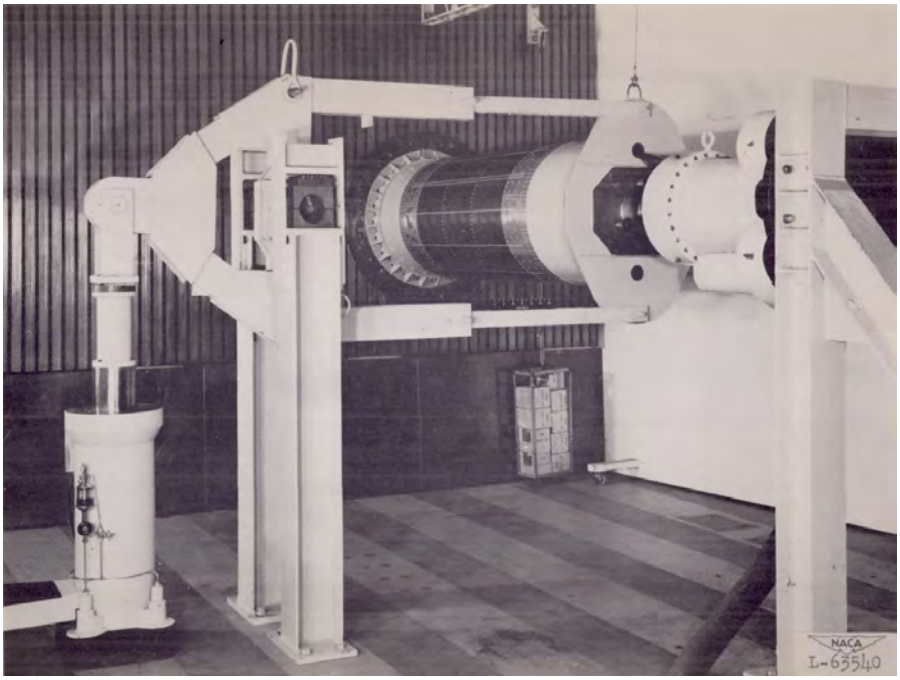

Figure 3.3: Experimental setup for cylinders tested under pure torsion and combined torsion and compression in the NACA tests [6]

3.2. Finite Element Modelling

To create the finite element models, ABAQUS 2022 was used. The geometry of the cylinder was modelled using SC8R elements, which are 8-node continuum shell elements. Each node has three displacement degrees of freedom. The kinematics and constitutive relations for this element is based on shell theory where the thickness is calculated from the element geometry. These elements offer more refined through the thickness section forces compared to conventional shell elements as these section forces are calculated from the deformation in the thickness direction and the initial elastic moduli. Moreover, the model created using these elements could be changed to use solid elements, which would allow more refinement and use of more advanced damage models in future studies.

3.2.1. Modelling the Geometry

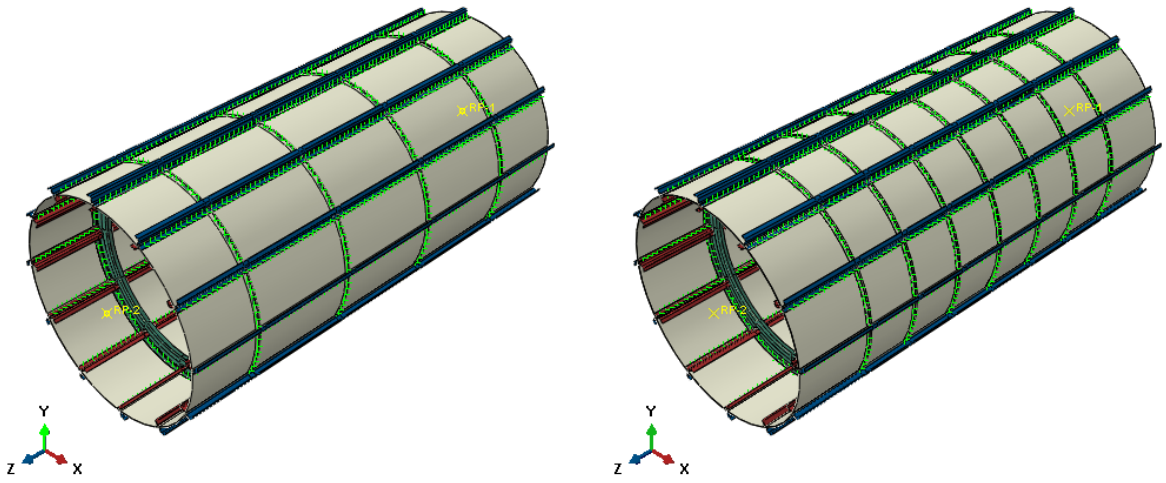

(a) 4-ring cylinders **(b)** 7-ring cylinders

Figure 3.4: Representative geometry of cylinders with 4 and 7 rings. The green markers show the locations of attachment points where the point-based fastener was created to model the rivets.

The skin and the stiffeners were created separately as solid parts and then assembled into the final geometry as shown in Figure 3.4[1]. A few simplifications were made to the geometry due to lack of information and to enable easier modelling. First, there is no information on how the thickness of the sheet was doubled in the end bays for this set of cylinders. However, the image of a cylinder tested in combined torsion and compression (shown in Figure 3.3) suggests that there is another layer of sheet joined with the skin using rivets. Additionally, the double thickness at the end bays and single thickness in the rest of the bays causes a step in thickness in the transition from the one to the other. Thus, of the two stringers attached to either side of the skin, one of them has uneven contact with the skin, depending upon the side on which the doubler plate is attached. No information is given as to how this consideration

[1]Only two cylinders are shown to be representative of the 4-ring and 7-ring cylinders as all cylinders from either categories have the same geometry except differences in the thickness of the constituent parts

has been taken into account in the fabrication of the test cylinders. One can only speculate whether there was a joggle provided on the stringers to make contact on both the single and the double thickness bays, or whether the stringers were straight and bent slightly to create a better contact. The latter could be the case as the thickness of the skin is very small and the compliance of the stringer may allow for such small deformations.

In the FE model, for simplicity, the stringers were modelled to be straight. For the double thickness region, two different strategies were used. In both cases, a cylindrical shell was created with the thickness of the . In the first one, a double thickness region was created on top of a cylindrical shell of uniform thickness at the end bays where they do not join with the stiffeners. However, this would create a discontinuity in the doubled region. Adding the doubled thickness to the locations where the stiffeners and the skin join would create issues with the contact as there will be some penetration of the parts into each other. So, in another approach, the ”Skin Reinforcement” feature in Abaqus was used to model the doubled thickness at the end bays. This feature overlays a shell section on top of a face of any solid geometry that can then be assigned a shell or membrane element. To model the doublers, the skin reinforcement was defined over all the top surfaces of the uniform cylinder that correspond to the doubled region. A thickness equal to the thickness of the skin was assigned on the skin, on top of the top surface of the solid part. The reinforcement was meshed with S4R elements that are 4-node conventional shell elements with reduced integration.

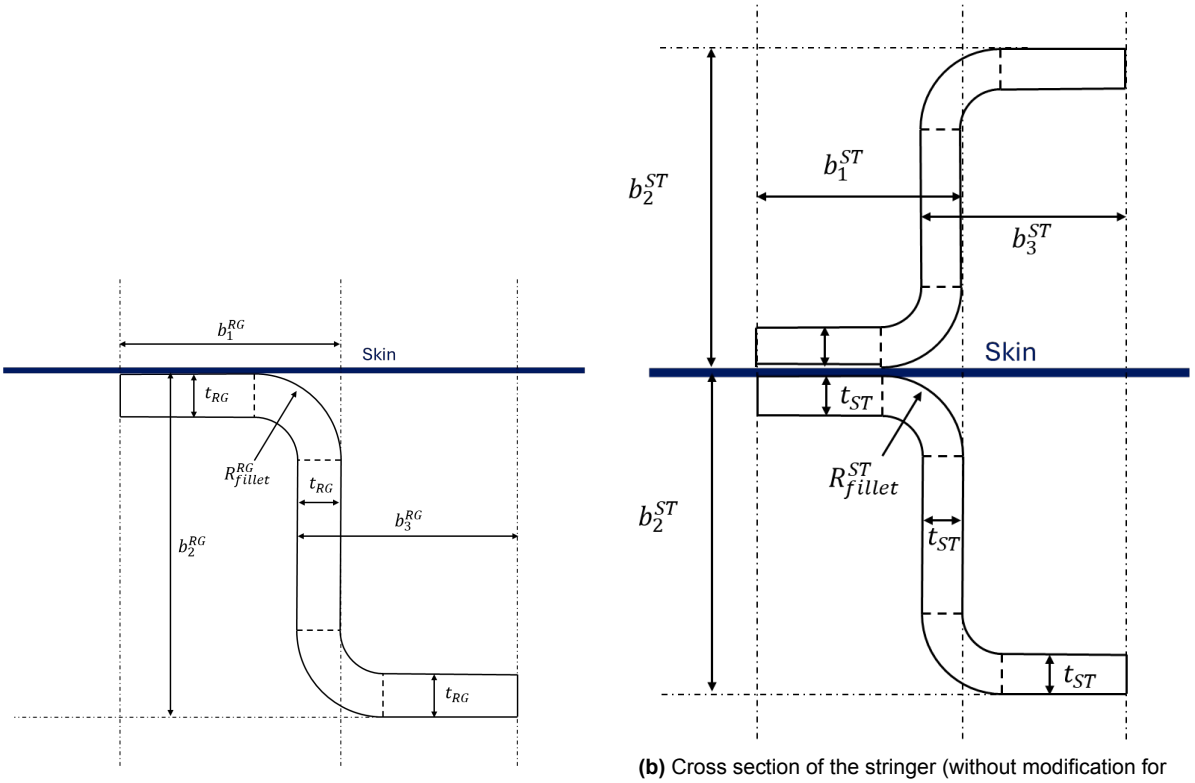

(a) Cross section of the ring

(b) Cross section of the stringer (without modification for curved skin)

Figure 3.5: Cross section of stiffeners as modelled in ABAQUS

Second, while the nominal dimensions of the stiffeners were provided (see Figure 3.2 and

Table 3.1), no measurement was provided about the fillet in the corners. Not modelling the fillets over-estimated the cross section area by around 8% compared to the reported value of cross section area. So, given the cross section area of the stiffeners (Table 3.1) and assuming the fillets on the outside and inside are concentric, the radii of the fillet were back-calculated. For the ring, the expression was evaluated to be the following (also refer Figure 3.5a):

$$R_{fillet}^{RG} = \frac{(A_{RG} - A_{RG}^{angled}) + (-2 + \frac{\pi}{2})t_{RG}^2}{(-4 + \pi)t_{RG}} \tag{3.1}$$

where A_{RG}^{angled} is the area of the cross section assuming no fillet, which is given by:

$$A_{RG}^{angled} = (b_1^{RG} + b_2^{RG} + b_3^{RG} - 2t_{RG})t_{RG}$$

For stringer, the above equations were used to back-calculate the fillet radius (R_{fillet}^{ST}) with a modification to account for the fact that Table 3.1 reports the combined area of the stringers on the outside and inside (also refer Figure 3.5b).

$$R_{fillet}^{ST} = \frac{(0.5 \cdot A_{ST} - A_{ST}^{angled}) + (-2 + \frac{\pi}{2})t_{ST}^2}{(-4 + \pi)t_{ST}} \tag{3.2}$$

where A_{ST}^{angled} is the area of the cross section assuming no fillet, which is given by:

$$A_{ST}^{angled} = (b_1^{ST} + b_2^{ST} + b_3^{ST} - 2t_{ST})t_{ST}$$

For the stringers, the geometry was modified slightly. To ensure that the bottom surface of the lower flange and the corresponding surface of the skin ”touch” at all points, the bottom flange of the stringers were curved (see the left diagram in Figure 3.6). The bottom flanges were curved around the axis of the cylinder and swept an angle of $\frac{b_1^{ST}}{R}$ radians. This angle corresponds to the length of bottom flange measured from the outer surface of the web to the tip of the flange wrapped around an arc equal to the outer radius of the cylinder. If the fillet is taken into account, a smaller length would be in contact with the skin. Assuming that this length is equal to ”$b_1^{ST} - R_{fillet}^{ST}$”, and that the fillets for each of stringers are tangent to the skin and the corresponding webs, the following expressions were derived for the fillet radii of the outside and inside stringers (referFigure 3.6),

$$R_{fillet}^{ST,\,out} = \frac{R \sin \theta_{ST}^{fillet}}{1 - \sin \theta_{ST}^{fillet}} \tag{3.3}$$

$$R_{fillet}^{ST,\,in} = \frac{R \sin \theta_{ST}^{fillet}}{1 + \sin \theta_{ST}^{fillet}} \tag{3.4}$$

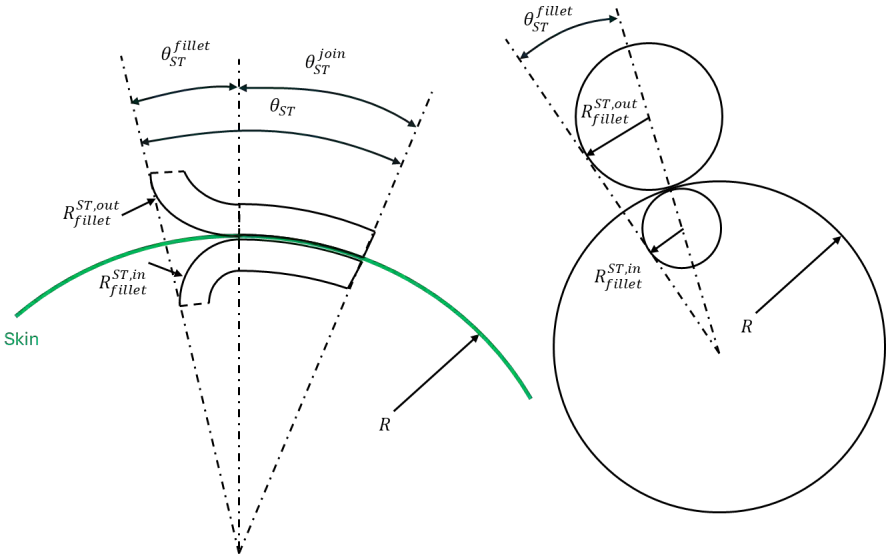

Figure 3.6: Drawing depicting the geometry modelled for the bottom flange of the stringers and the fillets

where, θ_{ST}^{fillet} is the angle swept at the centre of the skin cross section by the fillet,

$$\theta_{ST}^{fillet} = \theta_{ST} - \theta_{ST}^{join} \tag{3.5}$$

where, the θ_{ST} is the angle subtended by the nominal width of the bottom flange at the bottom of the top stringer, and θ_{ST}^{join} is the angle subtended by the joining surface between the top stringer and the skin. These are given by:

$$\theta_{ST} = \frac{b_1^{ST}}{R} \tag{3.6}$$

$$\theta_{ST}^{join} = \frac{b_1^{ST} - R_{fillet}^{ST}}{b_1^{ST}} \frac{b_1^{ST}}{R} \tag{3.7}$$

The use of the Equation 3.3 and Equation 3.4 does induce a slight inaccuracy in the cross section area of the total stringer because the assumption that the flange length barring the fillet region is "$b_1^{ST} - R_{fillet}^{ST}$". Also, the length of the bottom flange of the inside stringer is modelled as slightly less than b_1^{ST}.But, this enables the alignment of the mesh between the two stringers and the skin. It was decided that this method of modelling is "good enough" taking into account the lack of information on the details of the geometry used for the experiments.

For the inside stringer to pass through the ring, there were mouse holes provided in the rings at the locations of the stringer. As seen in Figure 3.1, it was shaped like a parallelogram cutout. However, again no information was provided about the dimensions. So, for the virtual testing model, a simple cutout profile was made by connecting the arc traced by the bottom flange and a similar arc for the top flange along the ring web mid-radius using two straight lines as seen in Figure 3.7. An arbitrary clearance of 0.05 mm was provided between the stringer cross section and the straight lines. The presence of the mouse-hole could mean that

there was contact between the ring and the stringer. However, no efforts were made to take this into account because of the lack of information from the experiments and the increased computational expense of modelling the contact.

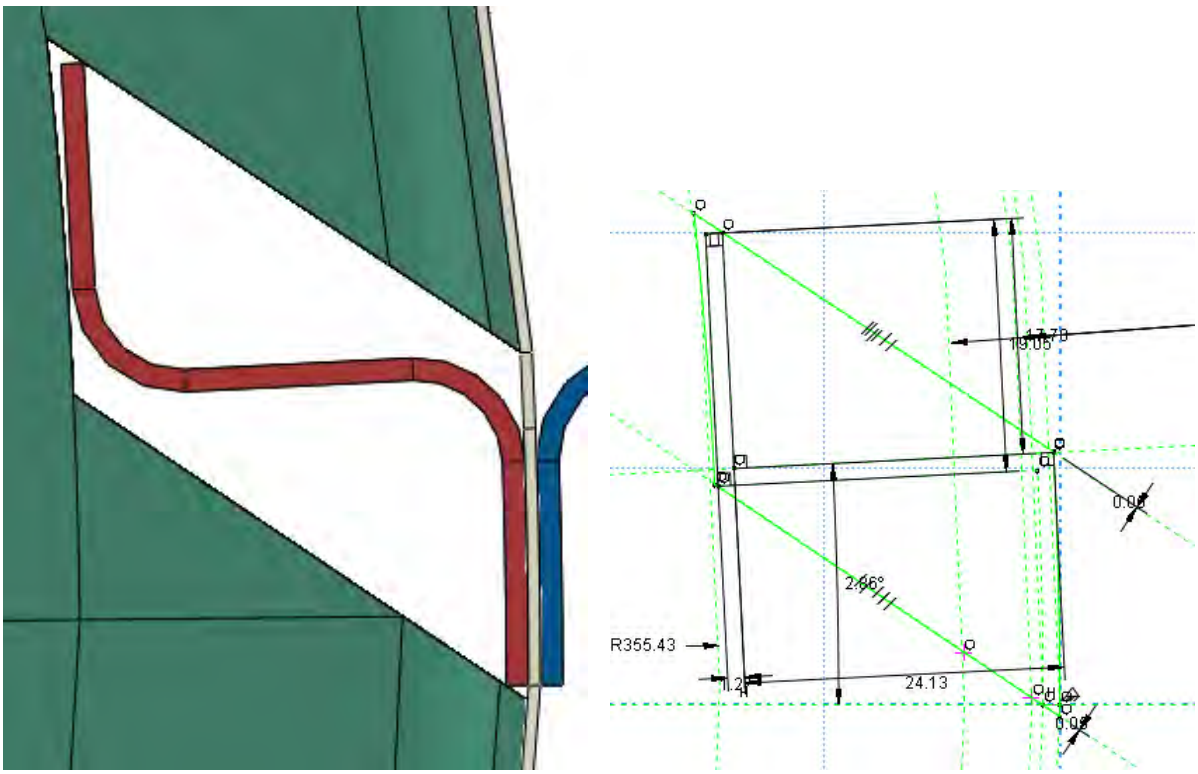

(a) Image **(b)** Dimensions

Figure 3.7: Ring cutout (mouse hole) modelled in ABAQUS for Cylinder-1

3.2.2. Joint between the stiffeners and the skin

In the experiments, rivets were used to assemble the cylinders. As no information about the rivets was available, it was assumed that the rivet pitch used is similar to the image shown in Figure 3.3. By observing the image, approximately, 7 rivets are used to attach the ring in every bay and 20 rivets were used to attach the stringer in every bay. In the model, two strategies were implemented. Initially, for its simplicity, surface-to-surface tie constraints were used to join the parts together. This connection is closer to a bonded joint than a riveted joint. So, to model the behaviour of riveted joints, ”point-based fasteners” were defined using rigid multi-point constraints. These constraints are defined by points that are created at the location of the fastener. The solver then finds the nodes on the surface to be coupled in a defined radius of influence. The motion of these nodes in their respective surfaces are then coupled in an average sense, which can be done using various weighting methods. In this study, uniform weighting which uses the same weights for the motion of all nodes in the radius of influence, which in this case was assigned to be equal to the radius of the rivet.

In the case of modelling point-based fasteners, it is necessary to model the contact between the skin and the stiffeners. This is because the surface of the stiffeners restrict the movement of

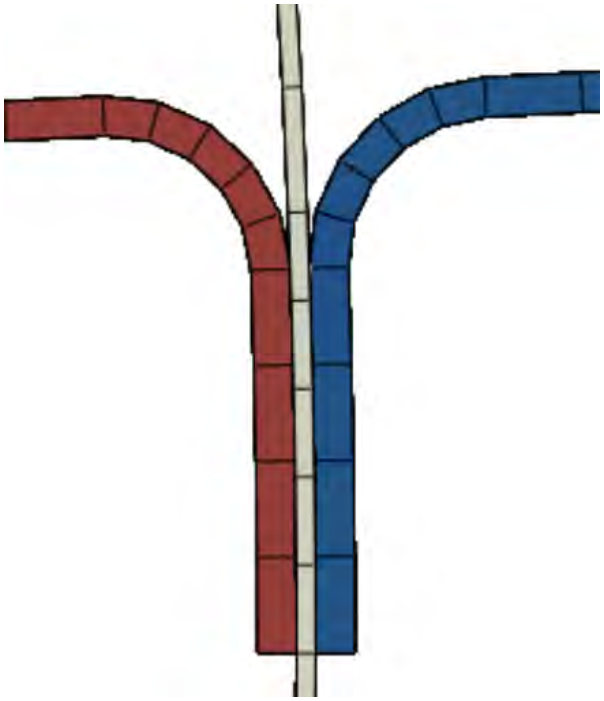

Figure 3.8: Figure showing the misalignment in the meshes of the skin and the stringers at the joining location.

the skin in addition to the rivets. To model this, the surface-to-surface finite sliding, ”hard” normal contact was defined between the relevant surfaces with frictionless tangential behaviour. The constrain enforcement method was kept to be default, which models the normal behaviour using a linear penalty stiffness method, where the penalty stiffness is 10 times the underlying element stiffness. This method is faster than the ”Direct” and ”Augmented Lagrange” methods (see [35]).

An interesting observation was made pertaining to the alignment of the meshes in the contact region. Usually, it is expected that aligning the meshes on the contact surfaces enables better convergence behaviour. However, in this study it was observed that when the mesh between the surfaces were completely aligned, i.e., their nodes were overlapping, the convergence was so slow as to not provide results in a practical time frame. Maligning the meshes by a small amount solved this issue, which can be seen in Figure 3.8.

3.2.3. Material Model

In the experimental reports, only the type of the alloy was specified, which was the 24S-T alloy. In the modern naming scheme of aluminium alloys, it is named the Al 2024-T3 alloy. However, in another NACA technical report from the year 1943 (NACA-WR-L-500) [36], the stress strain curves for the alloy was provided with the young’s modulus and the 0.2% yield stress. The plastic behaviour was modelled using the two parameter Ramberg-Osgood model (Equation 3.8).

$$\varepsilon = \varepsilon_{el} + \varepsilon_{pl} = \frac{\sigma}{E} + K\left(\frac{\sigma}{E}\right)^{n} \tag{3.8}$$

Tho calculate the Ramberg-Osgood coefficient and exponent, K and n was found by fitting two points, the 0.2% yield point and the ultimate point. As the ultimate load and permanent set at failure could not be found from the literature around the time of the experimental campaign, the values for the modern equivalent, Al 2024-T3 was used. The values are shown in Table 3.2 and the resulting stress-strain curve is shown in Figure 3.9. For the ABAQUS model, plasticity was defined by providing the yield stress and the plastic true strains and corresponding stresses in the strain hardening region. To ensure as close behaviour compared to the experimental curve and Equation 3.8, the yield stress was taken to be at 80% of the 0.2% yield stress and the plastic strain was set to be zero, which is a requirement in ABAQUS. This causes a slight discrepancy in the stress-strain curve, which can be seen on the right on Figure 3.9.

Table 3.2: Material properties used for the model

Young's Modulus	**0.2% Yield Stress**		**Ultimate Stress**		**Elongation After Failure**	
E, GPa	$\sigma_{0.2\%}$**, MPa**		σ_B**, MPa**		δ_B**, %**	
	Engineering	**True**	**Engineering**	**True**	**Engineering**	**True**
71.015	310.95	311.57	430	473	10	9.5

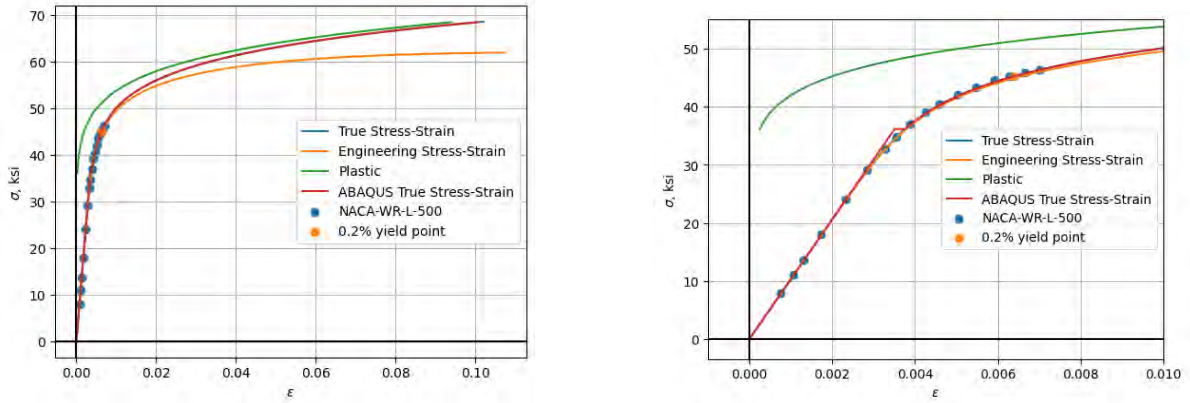

Figure 3.9: Material model used for the ABAQUS model compared to NACA-WR-L-500 data. Left: full curve, Right: elastic-plastic transition region

3.2.4. Boundary Conditions

The boundary conditions to be applied to the were supposed to imitate the loads applied on the cylinder from the jig. From Figure 3.1 and Figure 3.3, it can be seen that either end is attached to a heavy steel frames. Then, the steel frame is attached to a wall one one end an to the loading fixture on the other end. The connection of the ends of the cylinders to the steel frame can be idealised as the ends of the cylinders coupled to the motion of the frame because of the huge difference in stiffness. This was implemented in the model as the end surfaces of the cylinders being coupled to a reference point using rigid body coupling (see Figure 3.10). This couples all degrees of freedom of all nodes on the end surface to the degrees of freedom

of the reference points. In the experiment, the the skin would have been riveted to the steel frame. However, considering that there is no information about this connection provided in the reports, and the fact that the double thickness region distributes the load over the diagonal tension bays, it was thought that the current way of implementing the boundary conditions sufficiently captures the experimental behaviour.

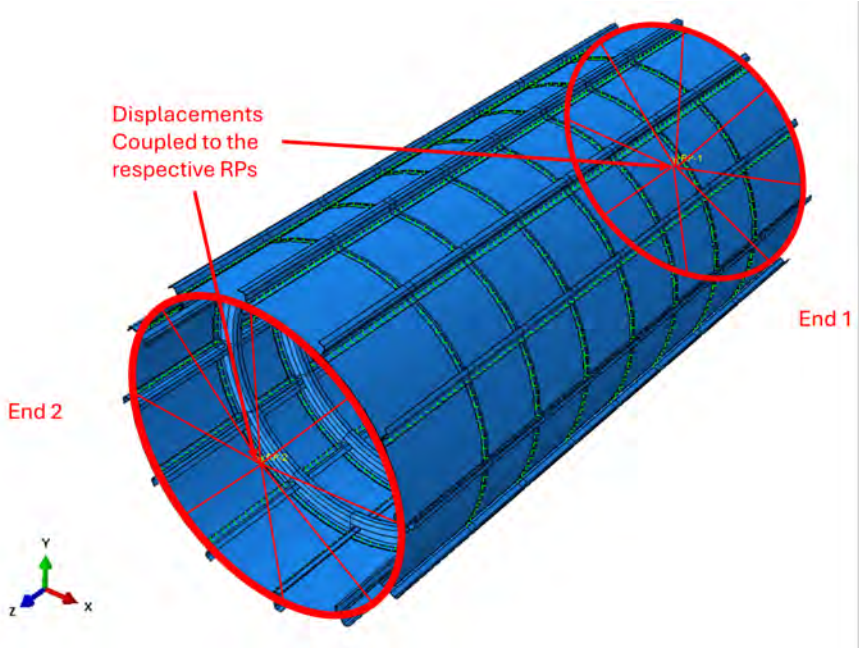

Figure 3.10: Boundary conditions applied to the ends of the cylinder

At the fixed end (End 1), all translation and rotation degrees of freedom were arrested, i.e., $U1 = U2 = U3 = UR1 = UR2 = UR3 = 0$ for the corresponding reference point. The testing jig shown in Figure 3.3 applies torsion to the cylinder using the hydraulic jack that rotates the steel frame on the fixed end about the axis of the cylinder. In the experiments, the loads were increased in steps and it was noted that the load did not drop anytime except for small load drops due to buckling of the skin. For the FE model, it was decided to only allow the translation and rotation of the loaded end surface in the axial directions, i.e., $U1 = U2 = UR1 = UR2 = 0$. The torque was applied by specifying an axial rotation of the loaded end. It was decided to use this displacement controlled loading because it seems to match what the experimenters did. Load controlled loading was ruled out because in that case, the load drops due to buckling would not have been perceptible.

A critical decision was to be made on whether to allow the movement of the loaded end in the axial direction or whether to constrain it. The diagonal tension effect in post buckling pulls the ends of the cylinder towards each other. So, if the loading end of the cylinder is free to move in the axial direction, it would move towards the fixed end. Constraining this degree of freedom would result in a reaction force that counteracts this tendency for the cylinder to shrink axially. This consideration is important to the results of this study and it's effects on the

stress distribution is discussed in a later section.

3.2.5. Solution Procedure

For the non-linear quasi-static analysis, the ABAQUS dynamic implicit solver was used with ”Quasi-static” formulation [35]. This solver uses implicit time integration to calculate the dynamic response of the system. The ”Quasi-static” formulation is used for when the concern is the final static response of a system under a given load. The inertial effects are introduced to provide a more stable response compared to the ”Static, General” solver. To capture the non-linearity in the material during post-buckling, the ”Nlgeom” option was turned on to model non-linear strains.

3.2.6. Modelling Geometrical Imperfections

It is known that the shear buckling curved plates are sensitive to imperfections and that the post-buckling behaviour shows little effect of the imperfection on the load-deformation behaviour. As this study aims to replicate the experiments, imperfections are needed to be modelled to possibly capture their effects that would have been present in the experiments.

In reality, the imperfections on the cylinders arise from the manufacturing and assembly process or external impacts. It is impossible to know the exact deviation from an ideal cylindrical surface because it was not measured in the experiments. However, for buckling analyses, it is known that assuming an imperfection field that is a scaled version of the first eigenmode of the shell causes the most drastic reduction in the buckling load [**citation_needed**]. In this study, the same approach was used to model the imperfection. While the behaviour would not be the same as that of the experimental cylinders, modelling the imperfection this way would allow some degree of accounting for the imperfection sensitivity.

3.2.7. Extraction of Stresses

The stresses on the stringers and the rings are the only reported observations from the NACA experiments apart from the failure loads. This is the data which will be used to validate the virtual testing model. So, it is imperative that the extraction of results from the finite element model is as close as possible to the strain measurement in the experiments [28, 6].

On the stringers, to capture the stress that is created only due to compression, the stresses on the upper flanges of the z-section were measured and averaged. The averaging will cancel out any effect due to the bending about the neutral axis, which will be extremely close to the skin mid-plane (see Figure 3.11). The strain gauges were applied on three to four stringers on the middle bay of each cylinder. The total number of strain gauges varied from 62 to 96, which means that the stresses at different locations along the length of the stringers were measured. Unfortunately, there is no information about the exact locations of the strain measurement.

The design of the rings in the experiments was done in a way to preclude ring failure and thus little effort was made on the extraction of ring stresses. On the cylinders that are under

consideration of this study, only three strain gauges were used to estimate stresses in the ring. The strain gauge was placed in the middle of the ring web (see Figure 3.11), which is around the location where the neutral axis of the ring, combined with the effective width of the skin will lie. Again, no information is available on the exact placement of the strain gauges along the circumferential direction of the stringers.

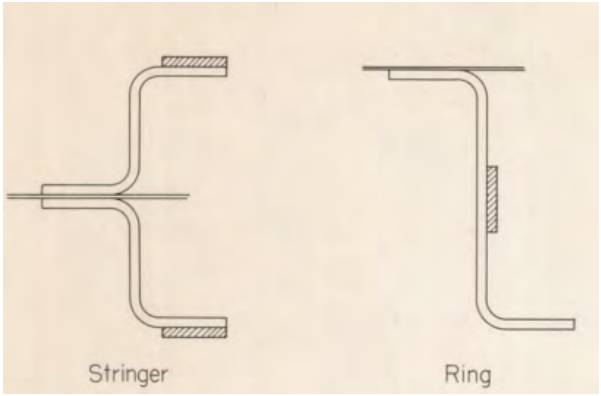

Figure 3.11: Placement of strain gauges on the cross section of the stiffeners (Taken from [6])

In this study, in order to account for the unknown locations of the measurement of the stresses, it was decided to calculate the stress at uniformly spaced locations all along the axial length of the stringers and the circumferential direction of the rings. The next decision was how to recreate the stress extracted from the gauges. The exact dimensions of the gauges depend upon the type used and there were multiple types of strain gauges used in the experiments. Furthermore, the exact locations of where a certain type of gauge was placed is unknown. However, Figure 3.11 suggests that the width of the strain gauges were of the order of the width of the flange without the fillet region. So, to recreate the stress measurement at a location, it was decided to average the surface stress for the elements that lie approximately on the region where the strain gauge was applied. For the stringers, this was all the elements on the top flange not part of the fillet and for the ring it was all the elements of the ring web.

3.3. Implementation of the Framework

To rapidly create a model using this framework, a parameterised Python script was created to automate the creation of the models using the above discussed modelling parameters. In addition to modelling the 8 NACA cylinders that will be used for validation and analysis later in the thesis, the implementation was made flexible enough to change the geometric and modelling parameters. To model the geometry, the script is able to generate cylinders of arbitrary dimensions, with variable number of stiffeners. However, the choices are limited to Z-shaped stiffeners only, but of variable cross sections. Furthermore, the script has the option to specify boundary conditions on the end surfaces of the cylinders and also to modify the solver settings. To post process the results for validation, a separate script is created that implements the extraction technique discussed earlier. The creation of this script allows rapid development of different configurations which would be useful in further studies.

4

Results and Validation

This chapter presents the results from virtual tests for the NACA cylinders using the framework presented in the last chapter using a similar stress extraction strategy as used in the experiments, which are then compared with experimental data to validate the model. With some exceptions which will be pointed out later in the text, all the results presented hereafter use the converged mesh as established in Appendix C. To understand the legend in the graphs, it is recommended to see the nomenclature for the extraction location as detailed in Appendix A. In the first section, the results for a typical non-linear analysis is presented to understand the results from the virtual testing models and their interpretation. Then, the effect of imperfections are analysed using the model. Finally, as the aim of this study is to establish a validated model, some interesting results relevant to validation is presented in the subsequent section, followed by the final section, which presents the results for all cylinders and a discussion on the validation of the model.

4.1. Results for a typical non-linear analysis

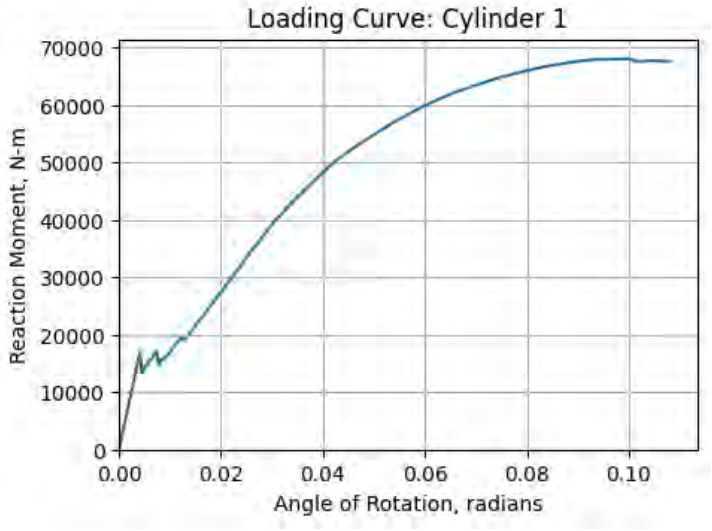

Figure 4.1: Loading Curve for Cylinder-1

To understand the results generated from the models, Cylinder-1 is taken as a typical case. The cylinder was loaded by applying a rotation of 0.12 radians to the loaded end about the z-axis. The loading curve can be seen in Figure 4.1. The response can be separated into two distinct sections. Initially, it is linear until a load drop is seen, which corresponds to the buckling of the skin at around 17.03 kN-m of torque. The second part of the graph is the post-buckled response, characterised by a reduced stiffness and non-linear behaviour. Similar analyses were run for all the other cylinders and the buckling loads calculated are plotted in Table 4.1. However, it is to be noted that the buckling loads for the 4-ring cylinders are being overshot by a bit (The reason for this suspicion can be found in subsection B.0.2).

Table 4.1: The buckling load observed from the Non-Linear analysis of perfect cylinders

Cylinder Number	Critical Torsion (kN-m)
1	17.03
2	24.48
3	19.04
4	23.67
5	49.68
6	60.84
7	59.95
8	63.08

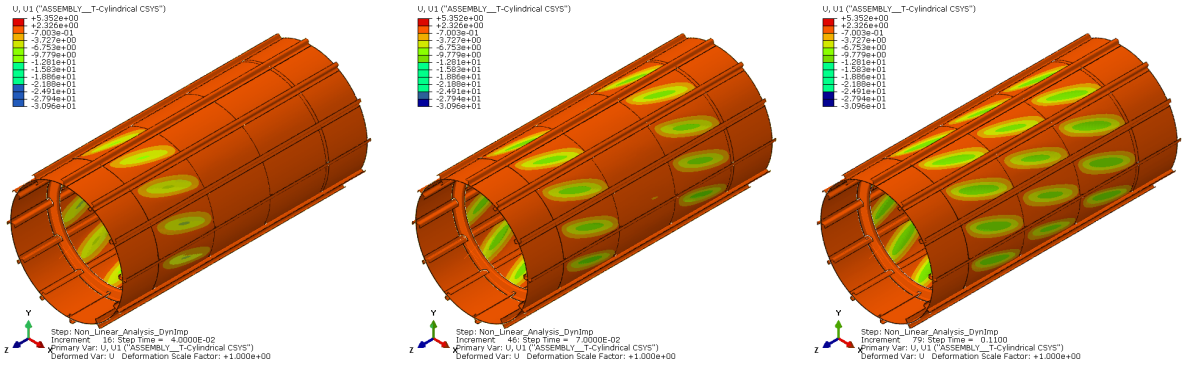

(a) First Buckled Bay **(b)** Second Buckled Bay **(c)** Third Buckled Bay

Figure 4.2: Consecutive buckling of different bays of Cylinder-1 (without imperfections)

Interestingly, two more load drops can be seen after this, the first one being similar in magnitude to the earlier one and the next one being very subtle. Looking at the deformation of the cylinder at these loads (see Figure 4.2), it can be observed that the three bays buckle at different applied displacements. This phenomenon may be explained by considering that the different bays have slightly different buckling loads despite having the same nominal dimensions. So, when the shear load applied on a bay reaches the critical value, it buckles, but the others do not. The load drop due to this bay buckling reduces the shear load on all the bays. On further loading, the second bay buckles with a corresponding load drop and the process repeats until the third and last bay buckles. The considerably higher buckling load of the third bay can be explained by the fact that the stringers and the rings alone would act like a frame structure, capable of taking some amount of torque.

This behaviour is very different from what was observed during the experiments where the buckles in most of the bays developed gradually and only a few bays showed ”snap buckling”, where the skin buckles all of a sudden. Furthermore, no load drops were observed and no sequential buckling was reported in the experiments, which indicates that the experiments had significant imperfections. It is known that the imperfections make the sharp bifurcation of equilibrium paths more gradual. Indeed, in a subsequent section, it will be seen that the addition of geometric imperfection on the model causes the sequential buckling to cease with the observation of gradual formation of buckles without load drops.

Figure 4.3 shows the radial displacement of the skin as the load in the stringer is increased. As soon as the skin buckles, a diagonally oriented half wave can be seen. As the load increases two secondary half waves can be seen on either side of the diagonal, which increase in magnitude. Another notable observation is that the skin deflection is radially inwards for essentially the whole of the buckled skin. This is consistent with the expectation that after buckling the diagonal tension effect tries to bring the skin into the plane defined by the two adjacent stringers. Figure 4.4 shows the view of a cross section made at the middle of the length of the cylinder, zoomed in to show the deformation between two stringers.

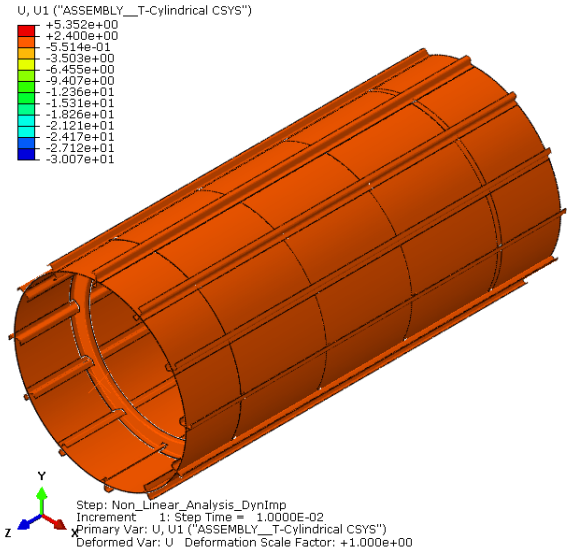

(a) Frame 1 | Twist = 0.0012 | Torque = 5.35 kN-m

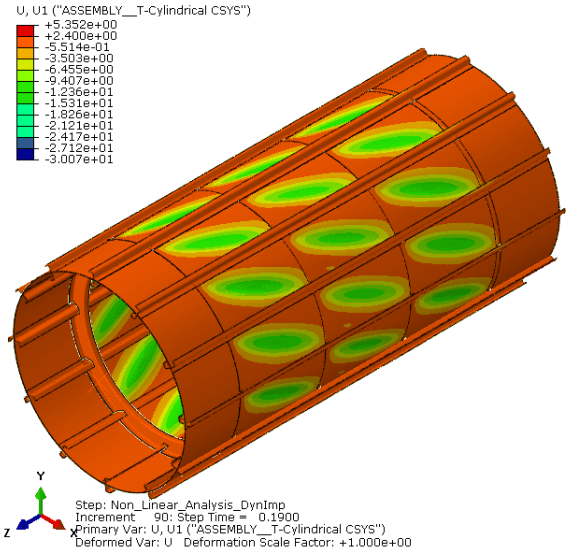

(b) Frame 19 | Twist = 0.0228 | Torque = 49.12 kN-m

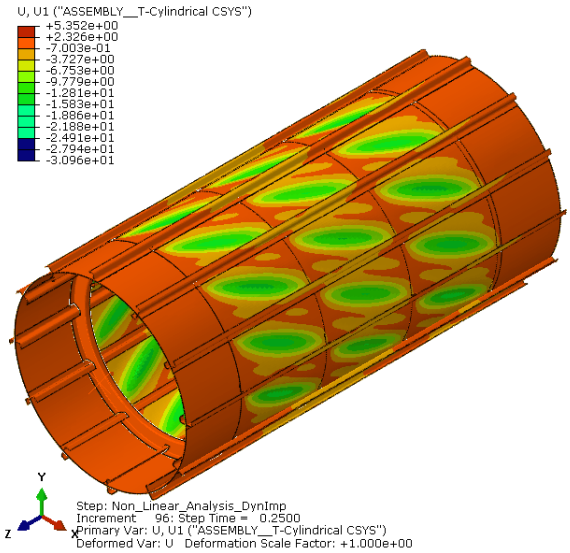

(c) Frame 25 | Twist = 0.03 | Torque = 59.06 kN-m

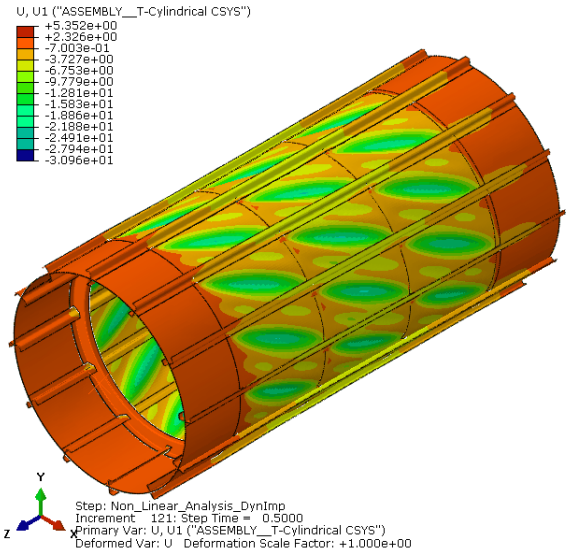

(d) Frame 50 | Twist = 0.06 | Torque = 81.724 kN-m

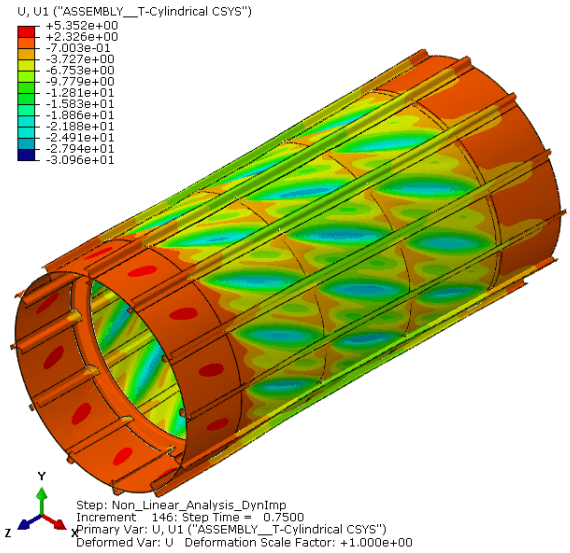

(e) Frame 75 | Twist = 0.09 | Torque = 91.77 kN-m

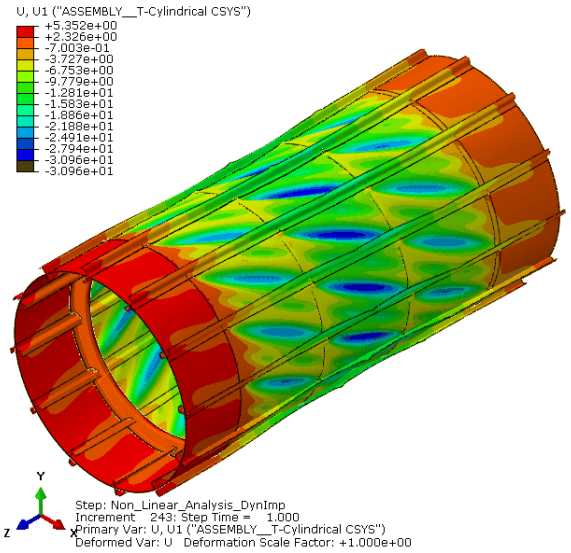

(f) Frame 100 | Twist = 0.12 | Torque = 95.62 kN-m

Figure 4.3: Radial Displacement of the model at different loads

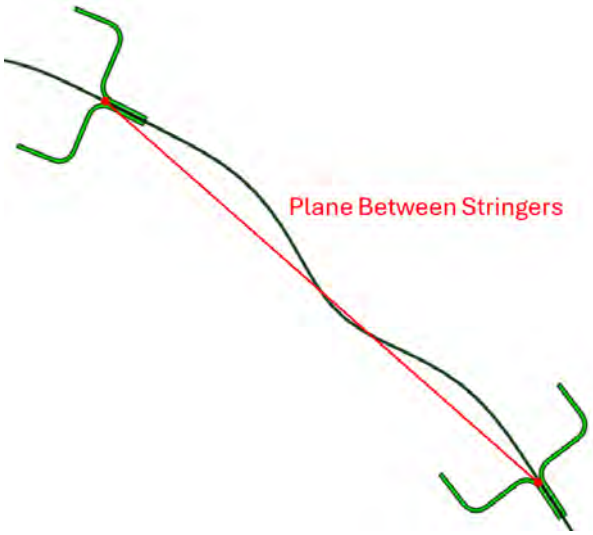

Figure 4.4: Cross Section of the Cylinder at the middle of the middle bay

4.1.1. Stringer Stresses

The stresses on the upper flange were calculated at 301 uniformly spaced cross sections for the inner and outer stringers and averaged to recreate the compressive stress measurement at a cross section as laid out earlier. The distribution of stresses in the inside stringer, the outside stringer and their average can be seen in Figure 4.5. Clearly, it can be seen that the inner stringer in under compression and the outer one is in tension due to the inward bending of the stringer. The distribution of the average can be seen for different loads in Figure 4.6a. Initially, the stringer is not loaded, but after buckling, compressive stresses can be observed on the stringer. The compression increases with the increase in load. Contrary to expectation of a peak compression at the centre [1], the compression is at a minimum towards the middle of the bay and peaks at the ring locations.

To compare the results to the experiments, the stress was extracted at different locations in the middle bay and averaged. The stresses were extracted at 20%, 50%, and 80% of the axial length of the bay for a single stringer. The reason to select only one stringer was because all the stringers had the same stress distribution. The stress in the middle of the stringer and that averaged over all the extraction locations was compared between different stringer and the same result was obtained (see Figure 4.7). The stresses at each of these locations and their average were plotted against the applied torsion and compared with the experimental observations (see Figure 4.6b). The trend of the stresses match pretty well with the experimental data. The fact that the compressive stresses are negligible while the cylinder remains unbuckled can be seen clearly. After that the compressive stress increases with the increase in applied load. However, the model seems to be considerably over-predicting the stresses, both on average and on comparing the maximum and minimum of all extraction locations.

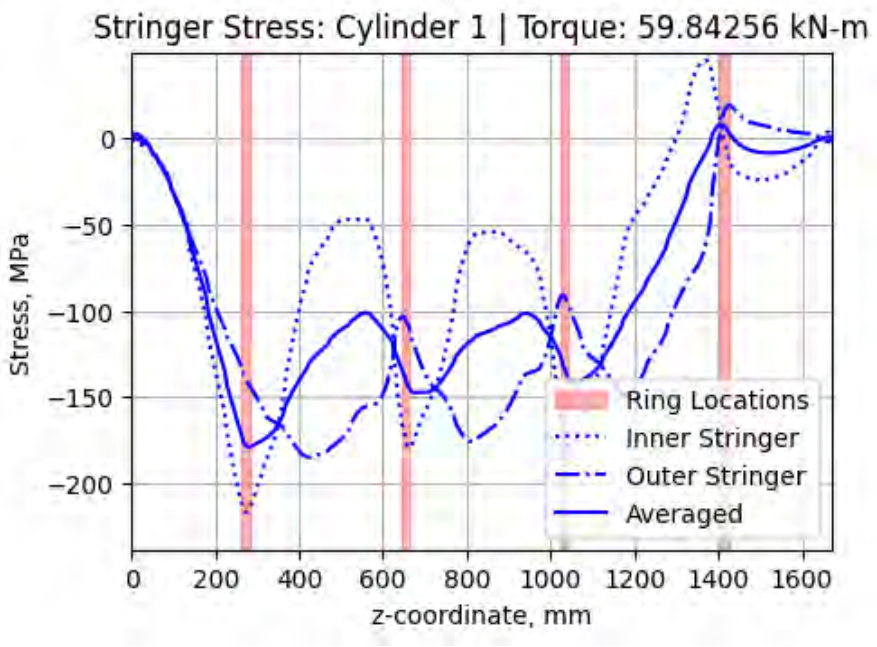

Figure 4.5: Stresses in the inner and outer stringers after post-buckling compared to the average value.

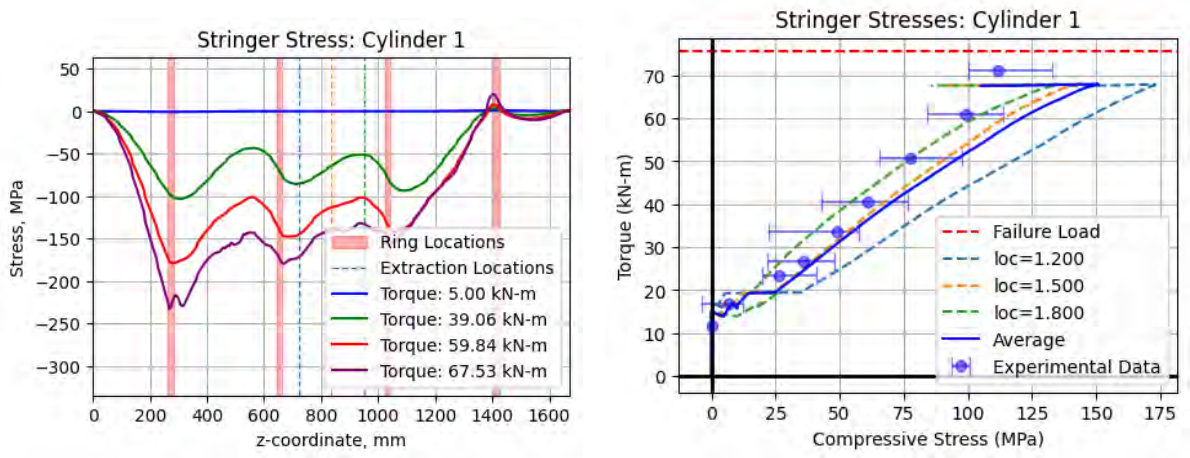

(a) Distribution of averaged stress over the length of the stringer

(b) Compressive stress vs applied torque at different extraction locations and their average

Figure 4.6: Development of stress in the stringers of Cylinder-1

Another difference compared to the experiments that become apparent are the sharp jumps in the graph during the buckling of different bays. In the experiment, due to imperfections, different bays buckled at different loads. But, on the torque vs stiffener stresses curve, a deviation from zero stress was observed gradually during buckling [1]. The results from the finite element model overshoot this point and on buckling, the stress jumps to a higher stress value. Further jumps can be seen when other bays buckle. This deviation in the behaviour of the finite element model is due to not accounting for imperfections. Thus, an effort was made to account for the imperfection, which is discussed in an upcoming section.

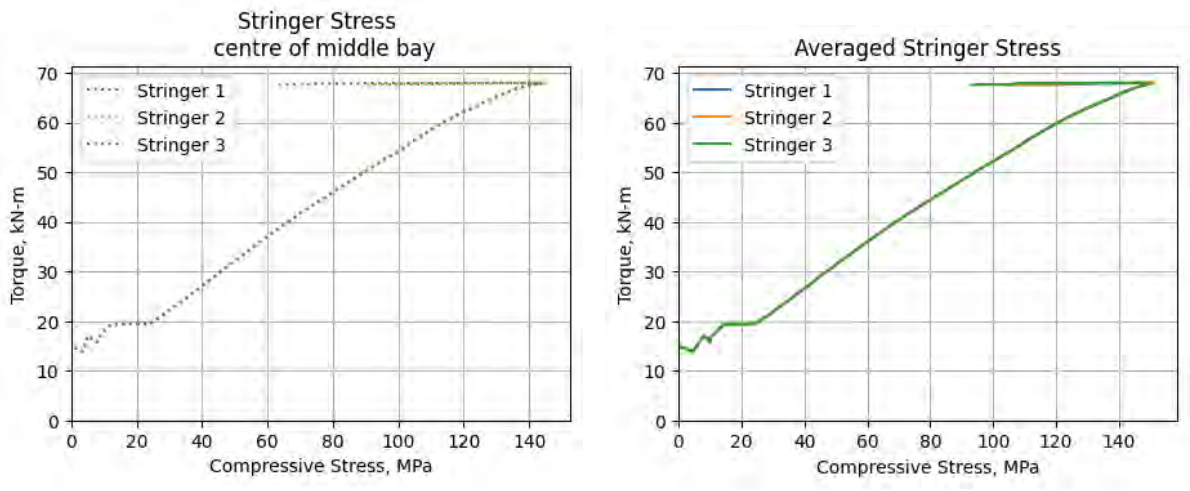

(a) Compressive stresses at the middle of three different stringers vs applied torque

(b) Compressive stress averaged over three locations for three different stringers vs applied torque

Figure 4.7: Comparison of stresses in different stringers of Cylinder-1

Finally, after loading the stringer to a very high load, a sudden drop in the stresses can be seen. This corresponds to the peak load in the torque-twist curve. And at this point, it was noticed that a crippling type of failure can be observed on the upper flange of the top stringer in the middle of the middle bay (Figure 4.8). The location of the failure corresponds to a minimum in average compression (see Figure 4.6a). So, the location of the failure would be explained by the additional compression on the upper flange introduced by the radially inward bending of the stringers in the middle of the bay. However, in the experiments, the kind of failure observed was the fracture of the web. Another observation is that the failure load for the cylinder in the experiment was higher. The occurrence of the crippling failure earlier than skin failure load of the cylinder likely arises from the over-prediction of compressive stresses in the FE model. In reality, the stresses in the stringers were likely lower and the skin had failed earlier than the load at which the upper flange would have crippled.

It should be noted that this FE model is not capable of predicting the skin fracture failure mode because the mesh on the skin is most likely not fine enough to capture the local stress concentrations with enough details. Furthermore, as the scope of this study is limited to the evaluation of loads on the stringer, efforts were not made to study the failure of any and hence, the discussion is limited to the earlier for all the cylinders.

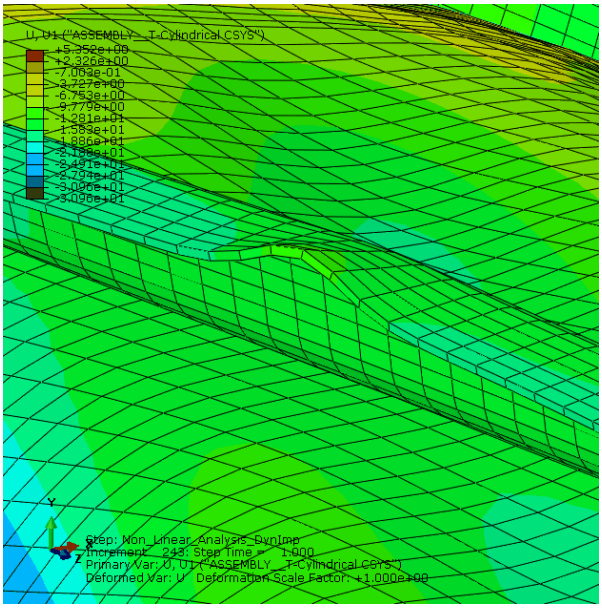

Figure 4.8: Crippling Failure on the Upper flange of the stringer in the middle bay

4.1.2. Ring Stresses

For the ring stresses, the results of the rings in the middle of the cylinder were studied. In a similar manner to the stringer stresses, the ring stresses were extracted from uniformly spaced locations along the circumferential direction. The extraction was from the elements adjoining the mean radius of the ring web as laid out earlier. The result for a three bays can be seen in Figure 4.9a, and for all bays can be seen in Figure 4.10. Again, it can be observed that the rings only get loaded after the skin buckles. Notably however, in this case, all of the ring is not under compression. There is considerable tension in the ring on going slightly towards the right from the stringer location. Going further in the direction of rotation, there is a compression peak near the middle of the ring. Then a local minimum in compression is followed by a secondary compression peak. This behaviour is considerably different than what was expected according to Kuhn et al [1]. Another noticeable trend is visible when looking at the graph for stress distribution on all of the ring (Figure 4.10). All the bays do not have the same behaviour. The stresses can be split into groups of three bays that show slightly different behaviour, that then seems to repeat four times.

To compare with the experimental data, the stress was to be extracted from positions where the strain gauges would have been placed. It is just mentioned that only three gauges were placed in every cylinder. Assuming that the experimenters would have placed the gauges in the middle of the bays, the stress is extracted from the middle of three bays of the ring and plotted with their average in Figure 4.9b. This time, the stress extracted from the rings match the stresses from the experiments very closely. In fact two locations exactly match the ring stresses, which is important in validation of the ring stresses. As in the experiments, three unknown locations were chosen, it may have been that the experiments missed the bay where the stresses would have been different.

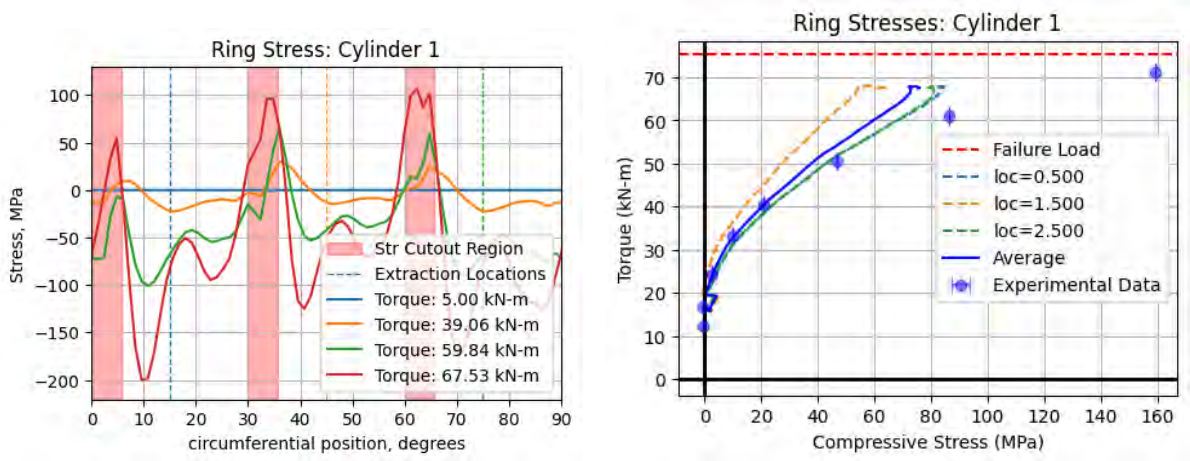

(a) Distribution of stress in the rings for three bays where the stresses are extracted

(b) Compressive stress vs applied torque in the ring (average of three extraction locations shown in the left figure)

Figure 4.9: Development of stress in the rings for Cylinder-1

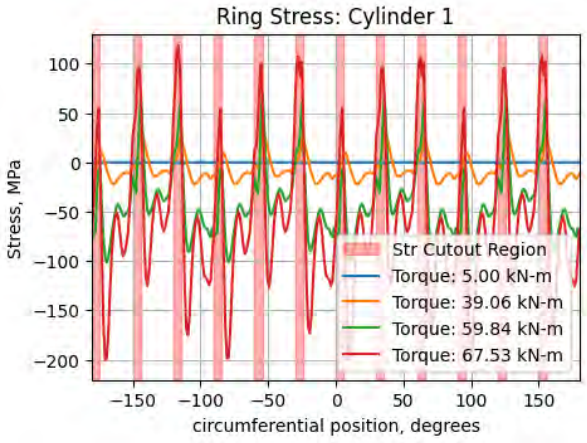

Figure 4.10: Distribution of stresses in the ring in all bays for the middle rings in Cylinder-1

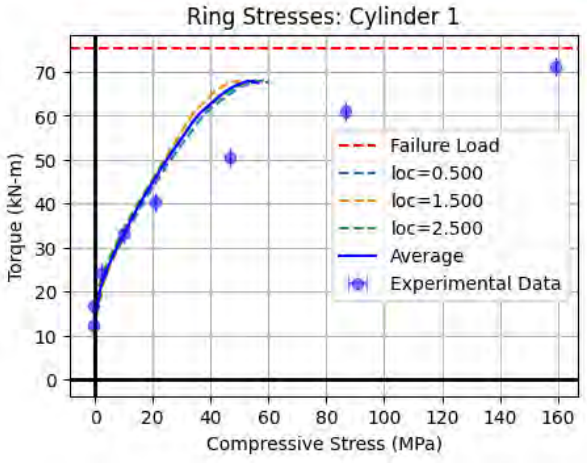

Figure 4.11: Stresses in the ring adjoining the doubled skin for Cylinder-1

In the case of the Cylinder-1, there are only two rings that adjoin a buckled bay on each side. So, it was assumed that the loading of both of them would be similar because of their similar position in the cylinders. The other rings would be affected by the unbuckled doubled region and would not have been used for the analysis. Stress extracted similarly for the ring adjoining the doubled skin is way lower in magnitude, which can be explained by the fact that the unbuckled skin is capable of supporting much more compression than a buckled skin, which would reduce the stresses in the stringer.

4.2. Effect of Imperfection

In the earlier study it was seen that the buckling of the bays occur all of a sudden at a value higher than what the experimenters had observed. So, it was judged important to take into account the imperfections that may have been present in the experiments.

Without the knowledge of the imperfections in the actual experiments, it was decided to use the buckling mode shapes as imperfections. To select the eigenmodes to be used as imperfections, the 25 modes were obtained from an eigenvalue analysis of the corresponding cylinder loaded using displacement control. It was found that all 25 eigenvalues were very close to each other in magnitude. The first mode had an eigenvalue of -3.86×10^{-3} and the 25th mode had the eigenvalue of -3.903×10^{-3}. Also, it was found that there were both negative and positive eigenvalues in the set. The mode shapes corresponding to the first two positive and negative eigenvalues can be seen in Figure 4.12 and they correspond to the rotation of the ends in either directions. It is also noticeable that different bays have different magnitudes of the buckling pattern. Furthermore, different numbers of half waves can be seen in different bays, some have 3 and some have 4 along the compression diagonal. Also, looking along the axis of the cylinders (see Figure 4.13), it can be seen that while there is no cyclic symmetry for individual bays, overall there is cyclic symmetry for four consecutive bays.

Finally, it was decided to superimpose the first positive and first negative buckling eigenmodes on the perfect model with different amplitudes. The choice of the modes to introduce the imperfection was driven by the fact that the half waves for the mode shapes in clockwise and anti-clockwise directions are aligned along the two diagonals of the skin bays respectively. So, to not create an imperfection field that is aligned with only one of these directions, the mode shapes of buckling in both directions were chosen. It was also not decided to use higher positive and negative modes because all modes were very similar in the bays and may have led to the cancellation of modes in some bays.

The following study would analyse the influence of the magnitude of imperfections. Note that this study is not meant to be a detailed analysis of imperfection sensitivity for curved skin-stiffened panels under post-buckling. Instead, the results would only be used to gauge the severity of imperfection sensitivity of the cylinders under consideration and how it affects the validation. In the study, different behaviour was observed for cylinders that had 3 post buckled bays and cylinders that had 6 post-buckled bays. The results are presented in this section.

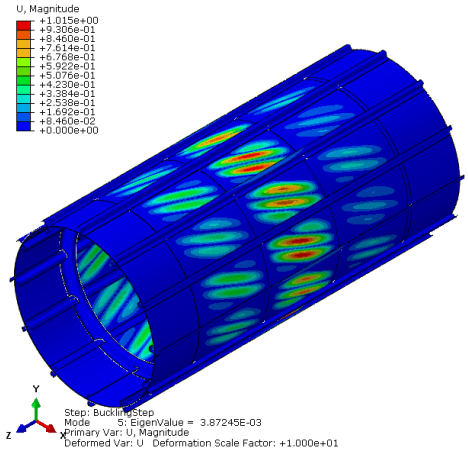

(a) First Positive Eigenvalue =

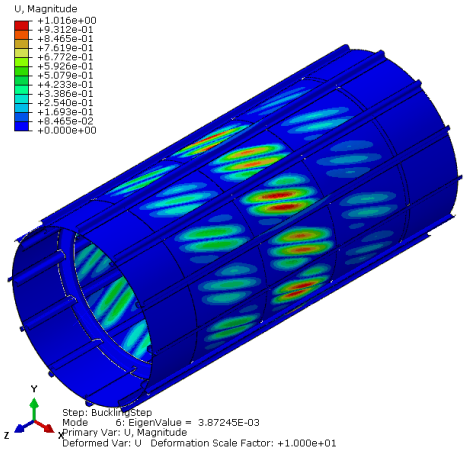

(b) Second Positive Eigenvalue =

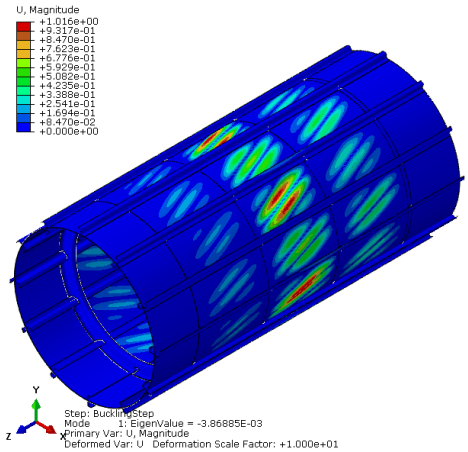

(c) First Negative Eigenvalue =

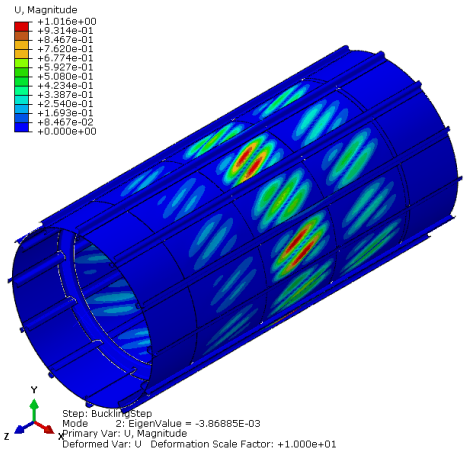

(d) Second Negative Eigenvalue =

Figure 4.12: Mode shapes corresponding to the first two positive and negative eigenvalues for Cylinder-1 (deformation scale factor=10)

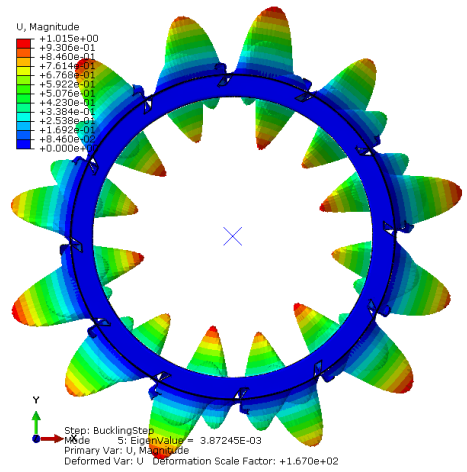

(a) First Positive Eigenvalue

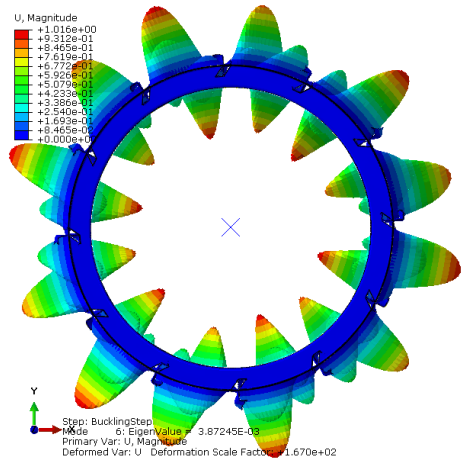

(b) Second Positive Eigenvalue

Figure 4.13: Axial view of the eigenmodes for the first two positive eigenvalues (deformation scale factor = 167.05)

4.2.1. Loading Curve

The loading curves (torque vs twist curves) for Cylinder-1 and Cylinder-2 are presented in Figure 4.14 and Figure 4.15 along with an accompanying figure showing the curves near the buckling point[1]. The legend "IMPF: X.XXX*t" indicates models for which the imperfection magnitude is X.XXX times the thickness of the skin. In both the cylinders the effect of imperfection is visible on the buckling load. Instead of a sharp buckling load characterised by a sharp load drop, the transition between the linear and post-buckled regime is gradual for all the tested values of imperfection, which is more akin to what was observed in the experiments compared to the perfect cylinder. On increasing the imperfection magnitude, it can be seen that the transition region becomes even larger. For the post-buckled domain, there is very little perceptible effect of the imperfections, which is in line with what was observed for unstiffened curved plates [19]. Further confirmation on the last observation can be drawn by looking at Figure 4.16 which compares the toque-twist curve of all perfect cylinders with those for cylinders with imperfection magnitude equal to the skin thickness. However, as it will be seen in the next section, the stresses that develop on the stiffeners are sensitive to imperfections.

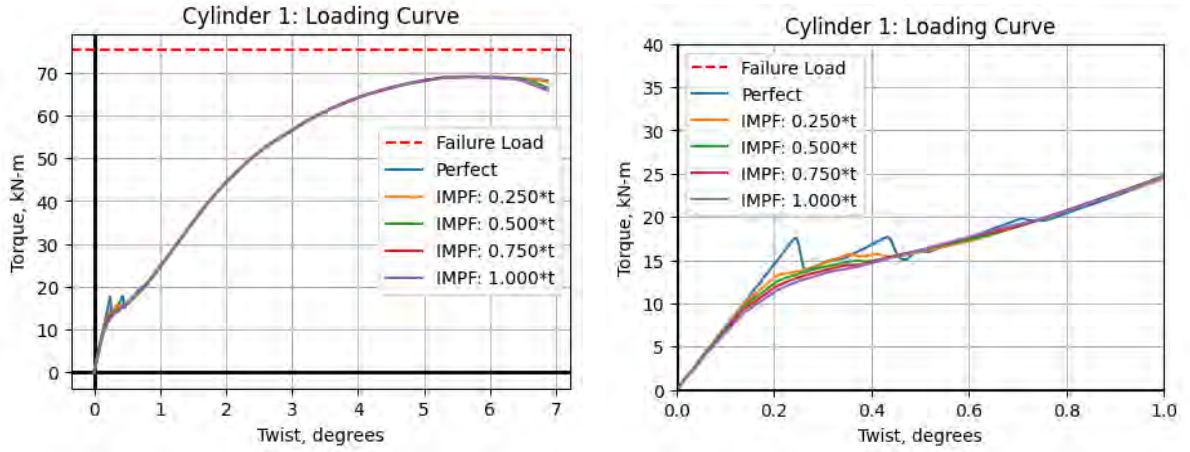

(a) Whole plot

(b) Zoomed in at the buckling point

Figure 4.14: Torque vs Twist curves for cylinder 1 with different magnitudes of imperfection modelled

4.2.2. Effect on the Stiffener Stresses

For the stringer stresses extracted in the same manner as in the last section, there was a very significant effect of imperfection for Cylinder-1. Looking at the average stresses and the stress extracted at the middle of stringer-1 Figure 4.17, the imperfection sensitivity becomes apparent. For imperfect cylinders, the point of deviation of the stresses from zero lowers a bit. Also, the transition to post-buckling stresses becomes gradual.

[1]The curves shown in this use results from models that did not use the converged mesh. The approximate mesh size used in the skin was 7.5 mm. This is the case for all graphs that compare multiple magnitudes of imperfection (Figure 4.15, Figure 4.17, Figure 4.18, Figure 4.22, Figure 4.23). It was decided against re-running these simulations as the conclusions drawn from these are expected to be independent of the mesh

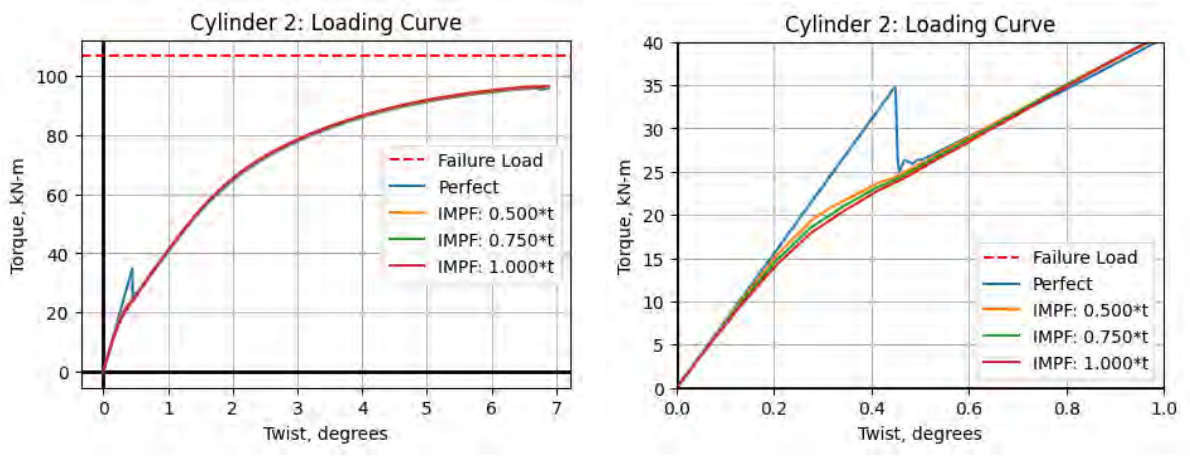

(a) Whole plot **(b)** Zoomed in at the buckling point

Figure 4.15: Torque vs Twist curves for cylinder 2 with different magnitudes of imperfection modelled

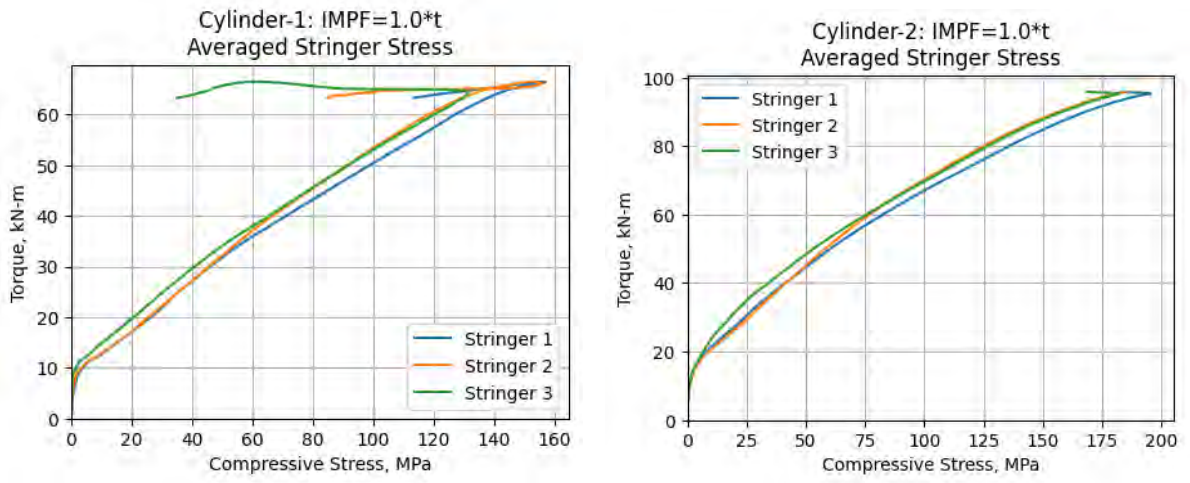

(a) Cylinder-1 **(b)** Cylinder-2

Figure 4.19: Differences between the stresses in different stringers with overlaid imperfection magnitude equal to skin thickness

Another noticeable trend apparent in this study is that there seems to be a jump in stress corresponding to the buckling of the third bay, which is now gradual for different magnitudes of imperfection. Another phenomenon that was noticed in the stringers was that there is different stress distribution in different stringers (see Figure 4.19a). The reason for this behaviour is likely the fact that the buckling mode shapes used for modelling the imperfections are not symmetric. The magnitude of the half waves are different in different bays (as seen earlier). This likely causes the difference in stresses in different stringers for the imperfect model.

Again, it can be seen that the introduction of load into the stringers is earlier and gradual. However, for post-buckling, the story for Cylinder-2 is quite different. There is very little imperfection sensitivity for the stresses in the stringer as seen from the graphs for stringer stresses averaged over the extraction locations and at the middle of the stringer (see Figure 4.18). Similarly

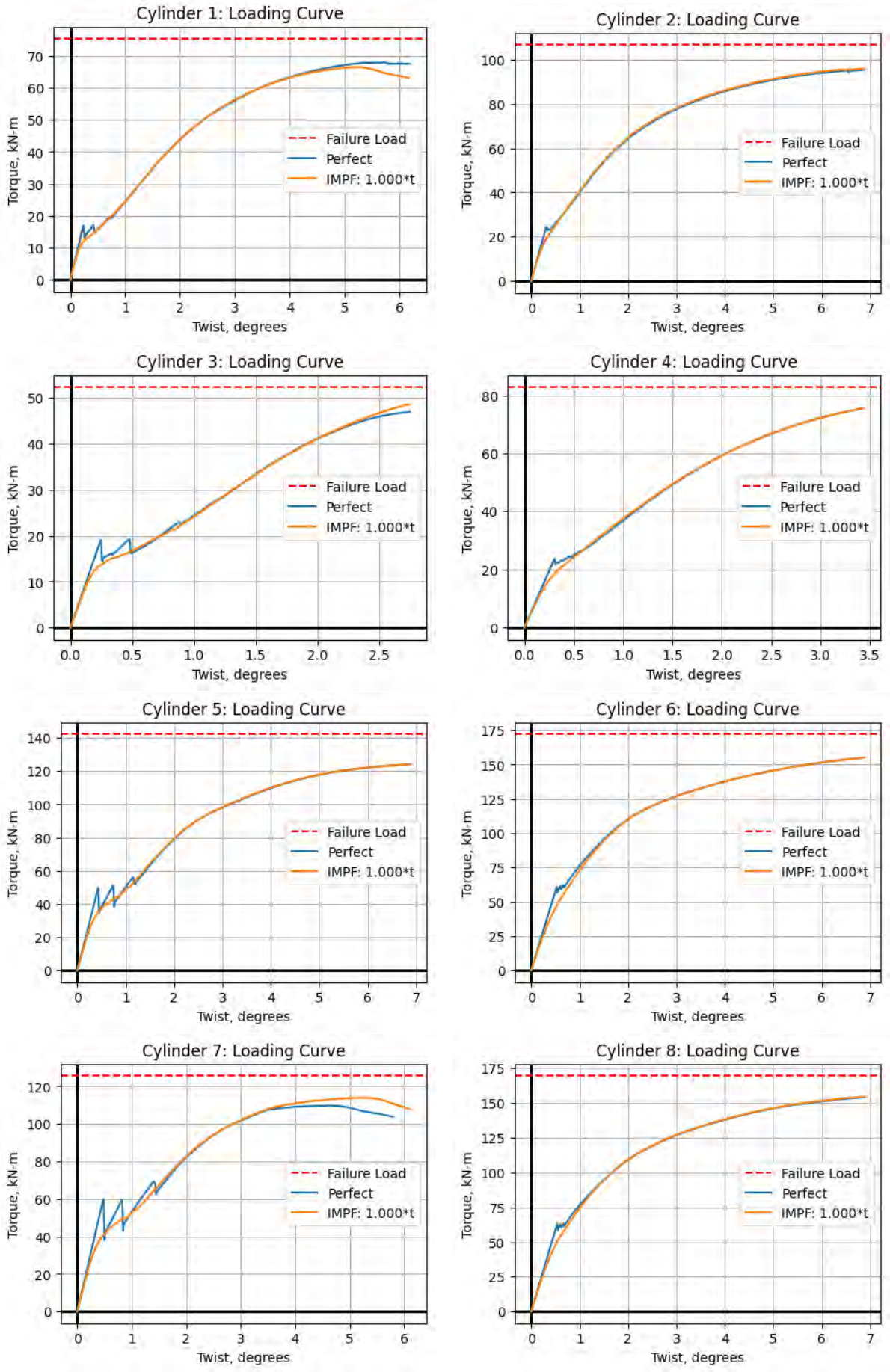

Figure 4.16: Torque vs twist curves for all perfect cylinders and with imperfection magnitude equal to the skin thickness

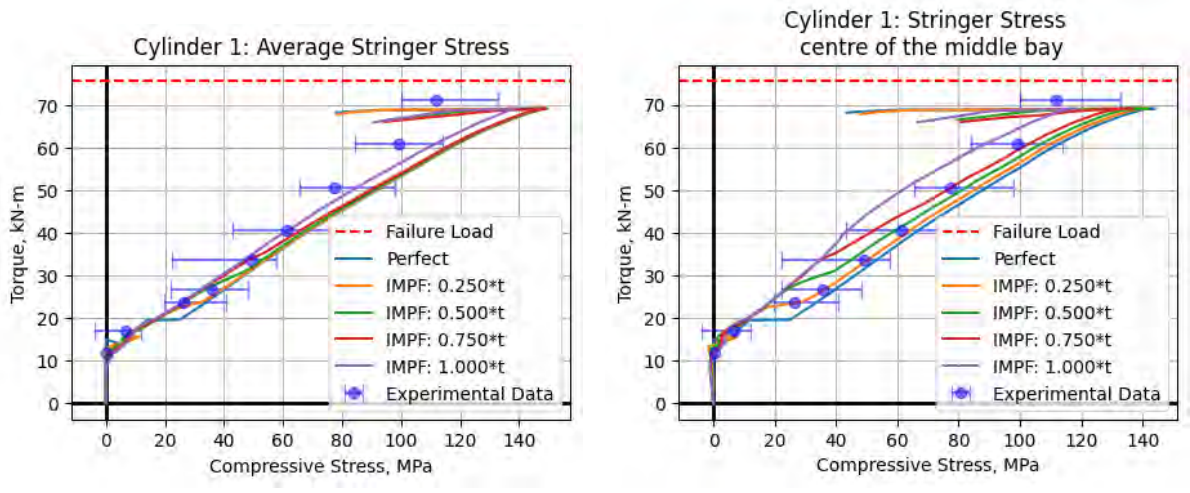

(a) Average of the three extraction locations for stringer-1 **(b)** At the middle of stringer 1

Figure 4.17: Effect of imperfection magnitude on the stresses in the stringers for Cylinder-1

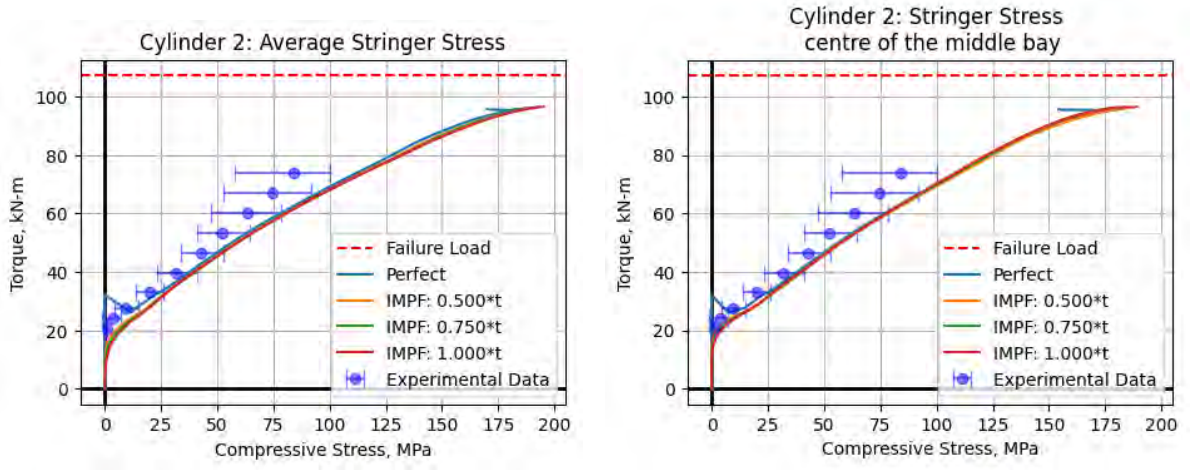

(a) Average of the three extraction locations for stringer-1 **(b)** At the middle of stringer 1

Figure 4.18: Effect of imperfection magnitude on the stresses in the stringers for Cylinder-2

to Cylinder-1, there is differences in the stresses of different stringers as seen in Figure 4.19b, arising from similar reasons.

To gauge the effect on all cylinders, it was decided to perform an imperfection analysis with the maximum imperfection used in this study i.e., equal to the skin thickness. Smaller imperfections were not studied as the analysis was only aimed at gauging the severity of imperfection sensitivity, and it is evident that the magnitude of the imperfection just makes the transition between linear and post-buckled regimes more gradual. This observation is assumed the same for all other cylinders.

The result of the study can be seen in Figure 4.24. Some degree of imperfection sensitivity is apparent in all the stringers. In all cases the general trend of the stresses is same as that of the perfect cylinders. A difference may be noticed between the cylinders with three bays (1, 3, 5, and 7) and those with six bays (2, 4, 6, and 8). In the earlier, the imperfection sensitivity is more noticeable and the stresses are decreased while in the latter, the imperfection sensitivity is less severe, and the stresses are in general higher than the perfect cylinders. Also, for some cases (4, 5, 6 and 8), the imperfection seems too severe as the start of deviation of the stresses from zero begins much earlier compared to both the perfect case and the experiments suggesting that the actual imperfection would have been much lower in magnitude. From this study, it may be qualitatively said that the imperfection magnitude does have a strong influence on the final stress response of the cylinder. Furthermore, the fact that the asymmetry in the overlaid mode shapes cause different stresses in different stringers suggests that the stress response is also sensitive to the shape of the imperfection.

For the stresses in the rings, like the stringers, the effect of the imperfections are different for different cylinders. For cylinder-1, there is very low imperfection sensitivity as seen from the graphs (Figure 4.22). But for Cylinder-2, the imperfection sensitivity causes a very apparent change in stresses (Figure 4.23. The average stresses do not seem to change as drastically, but for the stress extracted at the middle of bay 0, the behaviour changes completely. The latter might be the effect of the applied imperfection mode shape changing the starting point of the cyclic symmetry seen in the groups of three bays which was found even for perfect cylinders.

From the same motivation as for the study of imperfections on the stresses in the stringers, the effect of imperfection of the magnitude equal to the thickness of the skin was studied on the stresses developed in the rings for all cylinders as seen in Figure 4.25. Significant imperfection sensitivity was seen in all cylinders except cylinders 1, 5, and 7 for the deep post-buckling response. Again it may be concluded that there is a significant effect of the imperfection magnitude on the ring stresses. Furthermore, in a very similar vein to the stringers, there may be significant effect of the imperfection shapes, as it was seen in Cylinder-2, that the stresses in a specific bay may differ based on the imperfection shape on the bays that influences it.

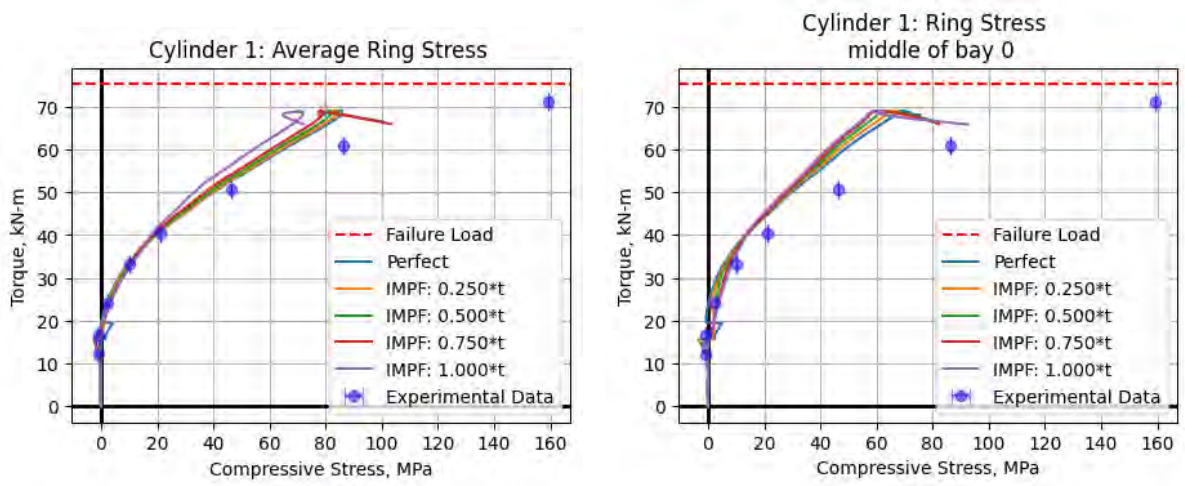

(a) Average of at the middle of bays 0, 1, and 2

(b) At the middle of bay 0

Figure 4.20: Effect of imperfection magnitude on the stresses in the ring for Cylinder-1

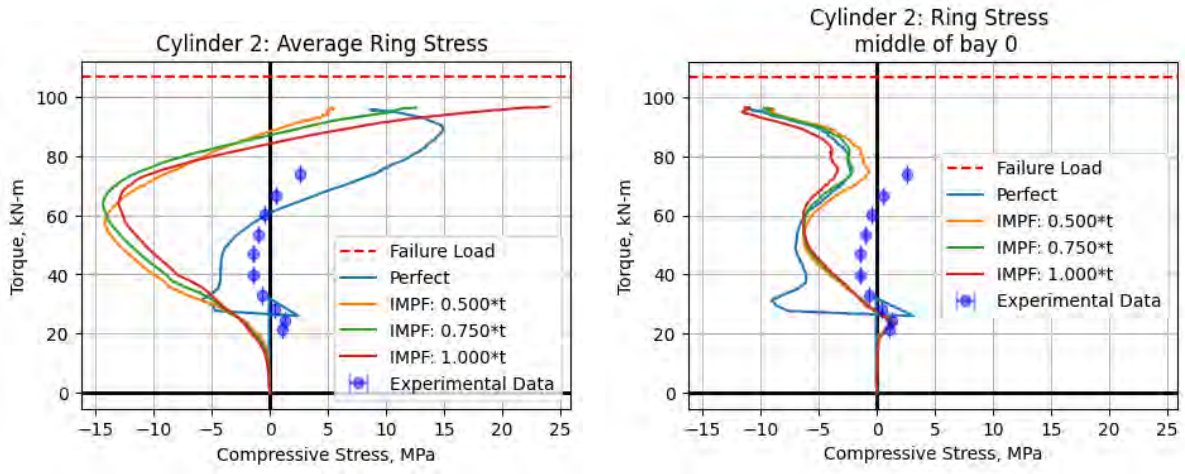

(a) Average of at the middle of bays 0, 1, and 2

(b) At the middle of bay 0

Figure 4.21: Effect of imperfection magnitude on the stresses in the ring for Cylinder-2

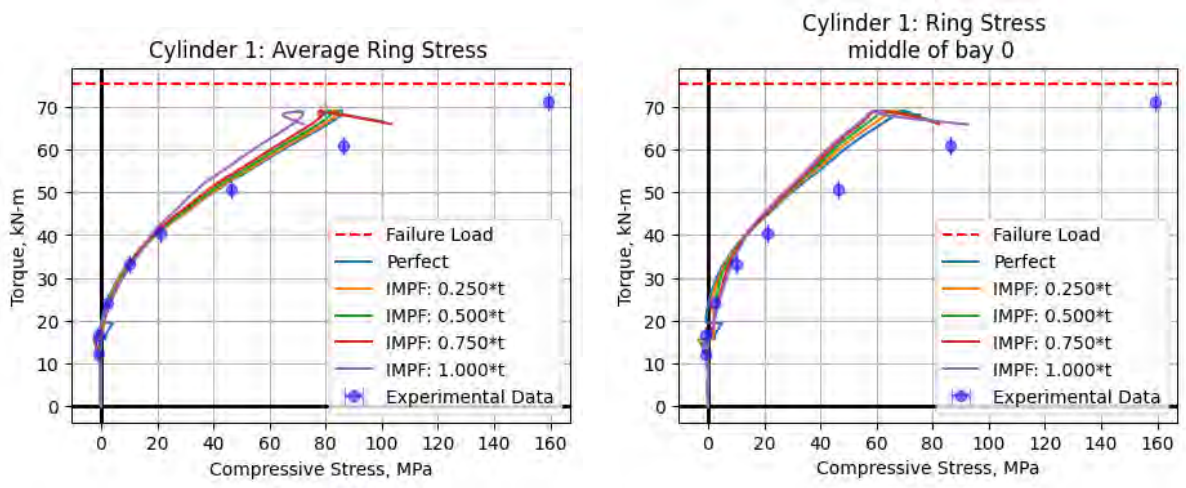

(a) Average of at the middle of bays 0, 1, and 2

(b) At the middle of bay 0

Figure 4.22: Effect of imperfection magnitude on the stresses in the ring for Cylinder-1

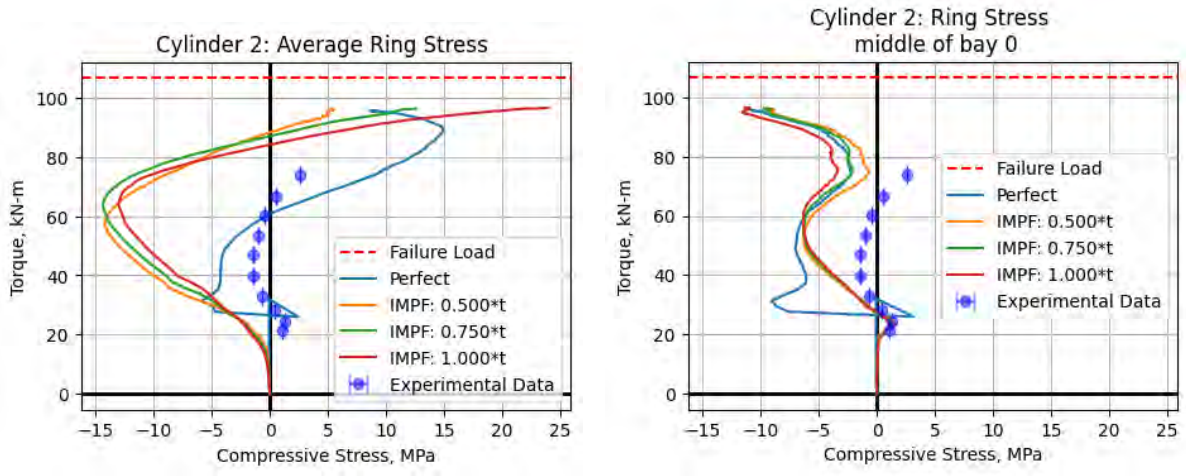

(a) Average of at the middle of bays 0, 1, and 2

(b) At the middle of bay 0

Figure 4.23: Effect of imperfection magnitude on the stresses in the ring for Cylinder-2

4.3. Other important effects

The overall aim for this chapter is to establish a validated model that has the same behaviour as the experiment and outputs the same results as the experiments. However, there are differences observed between the FEA results and the experiments, which are believed to arise from the model not taking into account details that are not available from the experiment report. This section presents two important effects observed in the FE models and how they could have been important in the original experiments.

4.3.1. Effect of constraining axial contraction of the cylinder

During the initial development of the modelling framework, it was needed to decide on whether to allow the axial movement of the loaded end or restrict it. To make the decision, analyses were run with both the boundary condition and the effects of constraining the axial contraction is

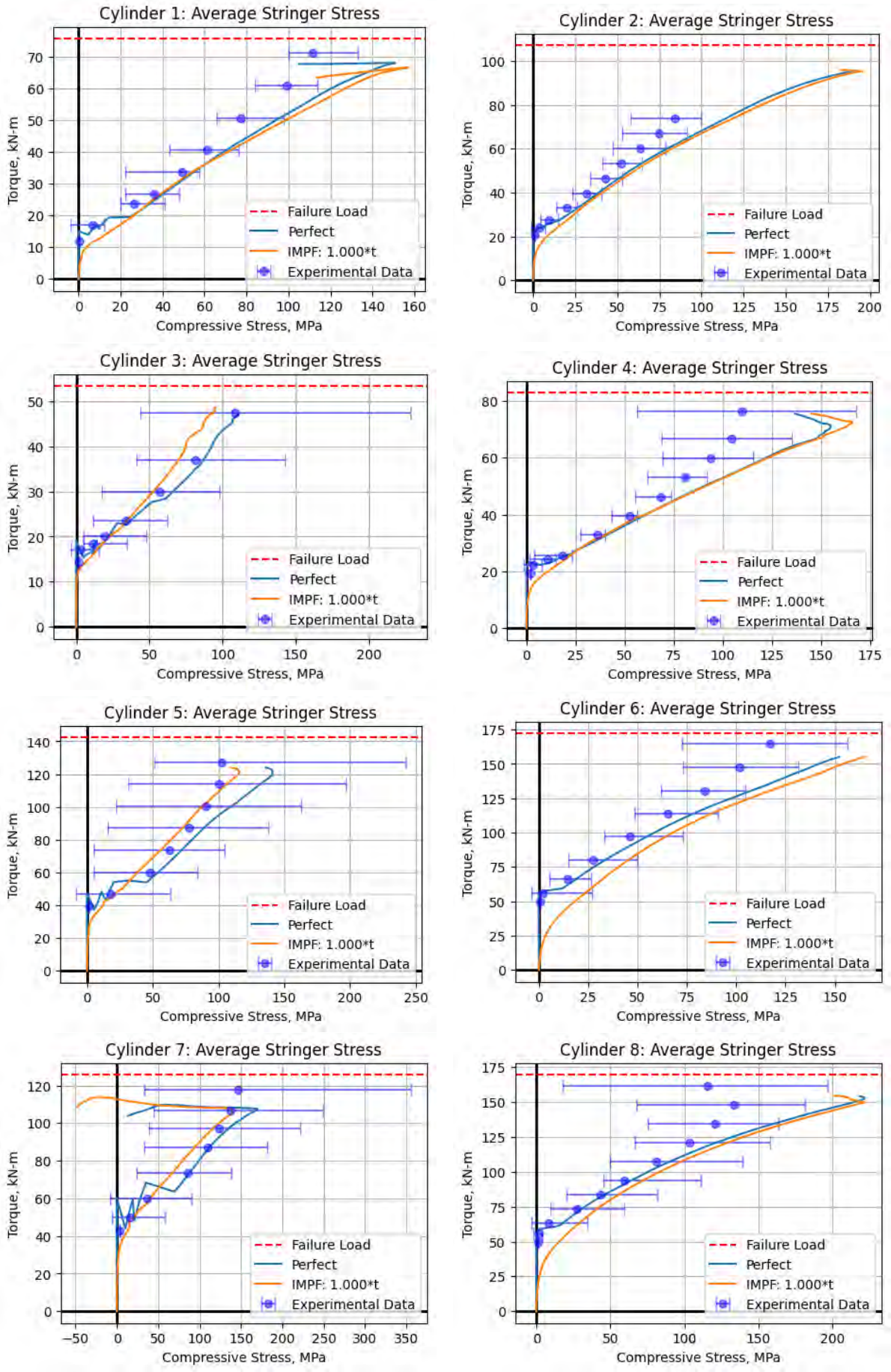

Figure 4.24: Comparison of virtual testing and experimental testing results for the stringer stresses in all cylinders

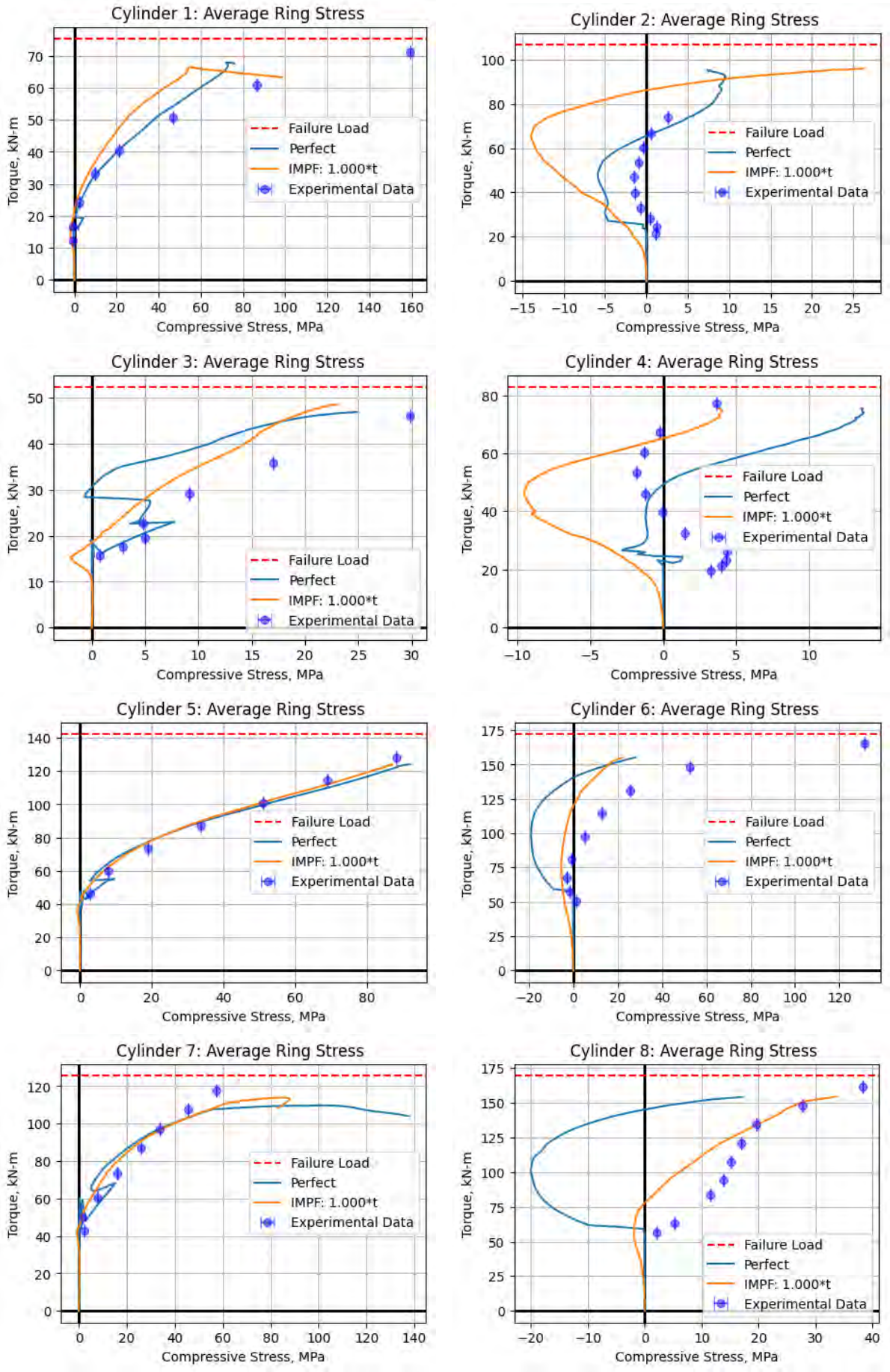

Figure 4.25: Comparison of virtual testing and experimental testing results for the ring stresses in all cylinders

presented here. The restriction of the loaded end of the cylinder was found to have immense impact on the behaviour of the Cylinder under post buckling. Looking at the loading curve (Figure 4.26), it can be seen that the curves match until the cylinder buckles. After which, the cylinder with fixed ends has a much more stiffer post-buckling response. This can be explained by the fact that the restriction in the axial contraction does not provide the alleviation of the stress in the post-buckled skin that would have been allowed if the ends could come closer to each other. The tension generated in the skin causes a reaction force at the ends due to them not being allowed to move axially, which can be seen in Figure 4.27.

The biggest difference in the behaviour can be seen on the stresses in the stringers. The compression developed in the stringer is negligible compared to the same cylinder where the axial contraction is allowed. This can be seen in Figure 4.28. Looking at the distribution of the stresses along the length of the stringer (Figure 4.29), it can be seen that on an average, the stress is very low. In fact, there even is tensile stresses in the stringers in the middle of the bay. Neglecting the bays except the middle bay because of them being affected too much by the doubled skin, it seems like the only load on the stiffener is due to the local variation of the shear flow transferred between the skin and the stringer. For the stresses in the rings, it seems that there is a slight increase (see Figure 4.30. This can be attributed to the change in the diagonal tension field in the skin.

Finally, observing the correlation between stresses calculated by the FE model and the experiments, it is apparent that allowing the cylinders to contract axially seems to model the compression observed in the stringers in the experiments more accurately. So, in all the analyses in this study, the cylinder's loaded end is allowed to move along the axial direction.

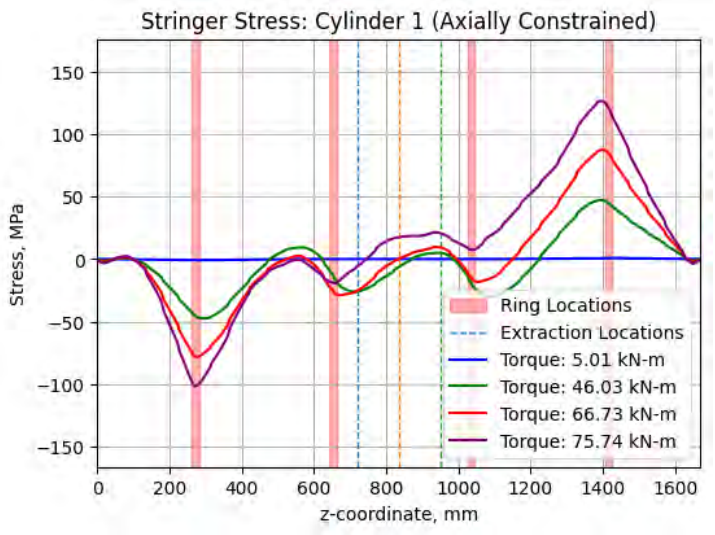

Figure 4.29: Distribution of Stresses in the stringer for Cylinder-1 with the ends restricted to move in axial direction

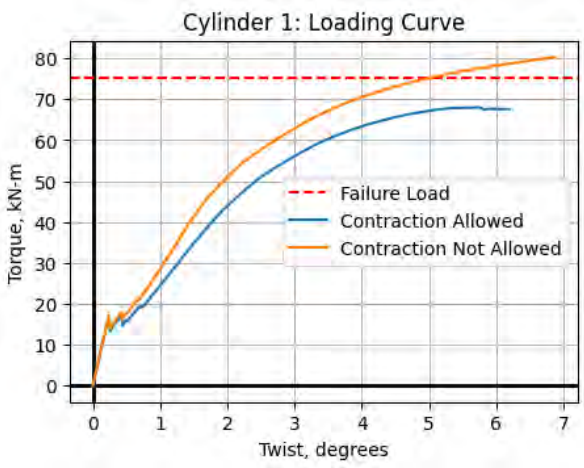

Figure 4.26: Effect of constraining the axial movement of the loaded end on the loading curve

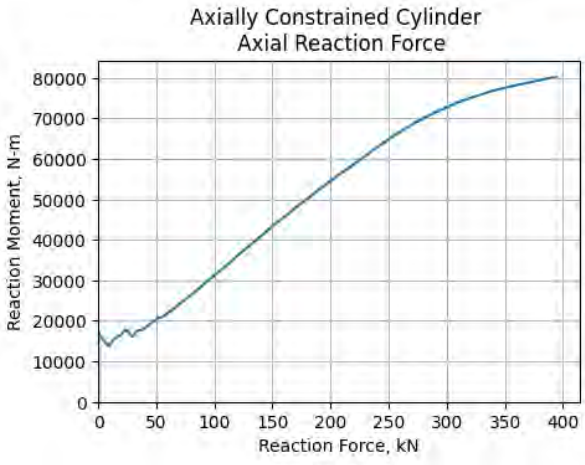

Figure 4.27: Reaction force created at the loaded end of the cylinder after the buckling of Cylinder 1 with restricted contraction in axial direction.

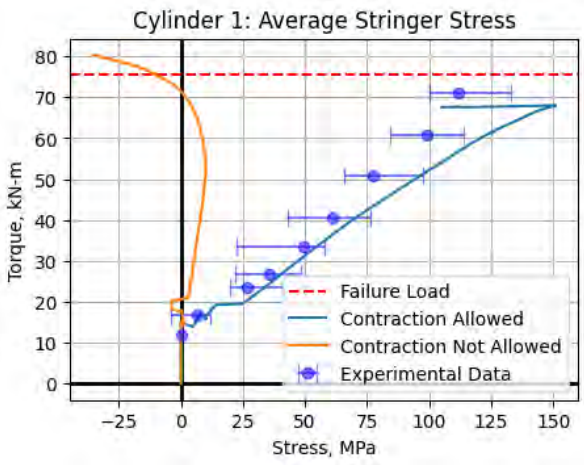

Figure 4.28: Effect of constraining the axial movement of the loaded end on the stringer stresses

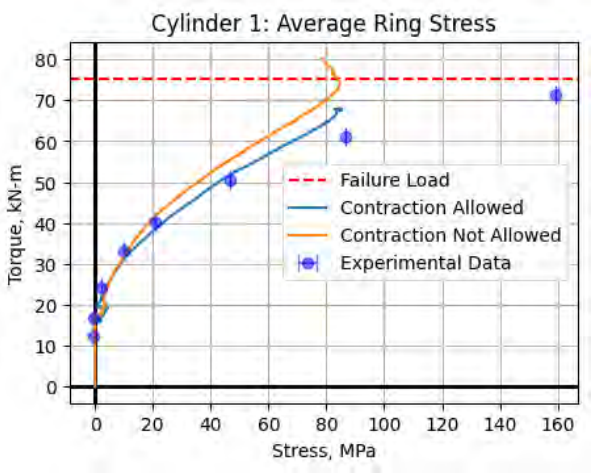

Figure 4.30: Effect of constraining the axial movement of the loaded end on the loading curve

4.3.2. Sensitivity of ring stresses to the positioning of extraction location

In the experiment report, no indication was given as to where the strain gauges were placed on the rings. Earlier, it was seen how the stress measured is different in different bays and here, results of a study is presented that found significant sensitivity of the extracted stresses that was found when the extraction location was changed slightly from the presumed middle of the bay location. Take for example the case of Cylinder 2, for which case multiple extraction locations around the middle of the bay is shown in Figure 4.31a, and the corresponding extracted stress from the locations are shown in Figure 4.31b. Assuming that the cylinder in experiment showed similar behaviour, it can be reasoned that even a slight change in the extraction location can cause a drastic change in the extracted stresses. This adds yet another layer of uncertainty for the validation of the model.

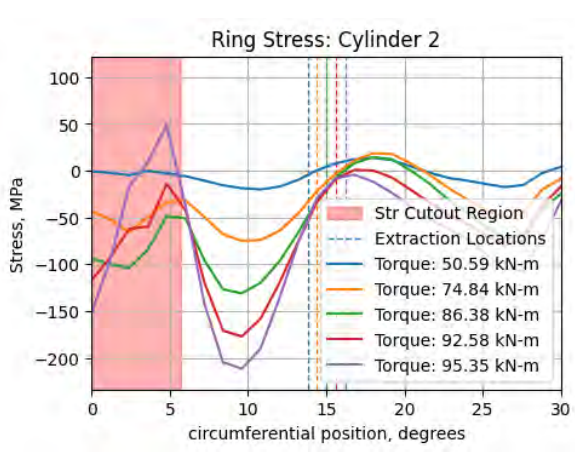

(a) Extraction locations within a bay

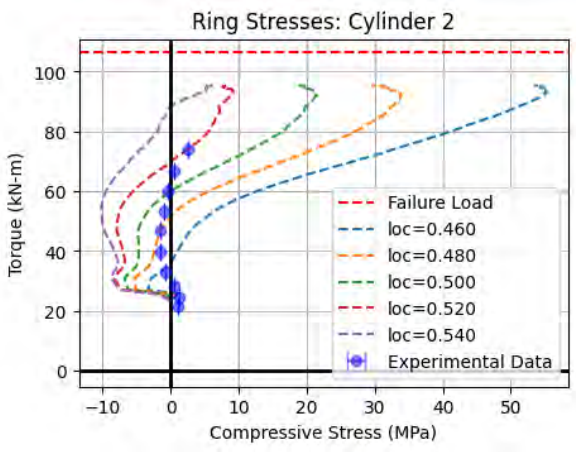

(b) Stresses at extraction locations

Figure 4.31: Sensitivity of ring stresses to the positioning of the extraction location in Cylinder-2

4.4. Discussion and Validation

In this chapter, the virtual testing framework was used to recreate the set of tests run at NACA [28, 6] in the development of the semi-empirical method [1]. The developed framework is aimed at performing further analyses to learn more about diagonal tension. So, it is important to analyse how accurately the virtual testing approach developed compares with the experiments. In this section, the correlation of the virtual testing results with the experimental results is judged and analysed.

4.4.1. Validation of Ring Stresses

For the discussion of the results and whether the model is validated or not, it would be appropriate to discuss the results for the rings first because they show remarkable agreement with the experiments. Significant imperfection sensitivity was found on the results, so the results for both perfect and imperfect cylinders were compared with the experimental observations (Figure 4.25). The correlation between the experiments and the FEA results were very close for some cylinders (Cylinders 1, 5). For cylinders 2 and 4, the experimental observation of stresses were very low, which was unexpected for the experimenters and prompted them to suspect that the strain gauges were not functioning properly [28, 6]. But remarkably, the results from the virtual testing model show results that are similarly low in magnitude and also in a broad sense, match the trend seen in the experiments, however with significant difference in the exact values. The results from virtual testing show that the measured stresses were not erroneous and shows that indeed the behaviour of the experiments are captured. What seems to be happening at the extraction location is that there is a superposition of compression and bending stresses due to the shear force provided by the skin and a possible shift in neutral axis due to the support of the skin is reasoned to make the stress at the extraction location very low.

For the other cylinders, better correlation was found when the other rings were used instead of the middlemost rings (Cylinders 3,6,7, and 8) as seen in Figure 4.32. For cylinders with 4 rings, this ring corresponds to the last ring and for cylinders with 7 rings, this ring is one ring towards the loaded end from the middle-most ring. Furthermore, there was significant sensitivity to the placement of the strain gauges for some cylinders, where changing the location slightly in the ring will change the stress plot drastically as seen earlier. Also, changing the bay where the stress is extracted changes the graphs significantly because of the the stresses not being the same in all rings as seen in subsection 4.1.2. This sensitivity is so high that by careful placement of the stress extraction location and averaging, the results from the FE analyses can perhaps be ”fit to match” the experimental results. However, such an approach will be contrived, and no concrete verdict may be given for the validation of the model for the outputs that show high sensitivity. In addition to the above, significant imperfection sensitivity adds another layer of uncertainty as it was found that imperfections significantly affect the results, but accounting for them is not possible due to them not being measured in the original set of experiments. However, for cylinders that do not show such a high level of uncertainty, the

model can be said to be validated. In the view of the above, it can be safely said that while the full recreation of the experimental result is practically impossible, the current modelling approach shows good correlation with the response of the experimental cylinders within the range of possibilities caused by the uncertainties.

4.4.2. Validation of Stringer Stresses

Again, due to the imperfection sensitivity of the stringer stresses, The stringer stresses obtained from the finite element model are in general over-predicting the stresses compared to the experiments (see Figure 4.24). For almost all the cylinders, the finite element model seems to be close to the experimental results after the early transition between the linear and post-buckled regime. And deeper into the post-buckling regime, the finite element model seems to over-predict the stresses. For those models that were tested to high enough loads, this over-prediction seems to precipitate crippling of the stringers at loads significantly lower than the loads at which they failed in the experiment (Cylinders 1, 2, 4, 5, and 7. Note the drop in stresses at high loads).

There are similar sources of uncertainty in the experimental data for the stringers that were present for the rings, namely the unknown imperfection in the geometry and the unknown exact locations of extraction of the stresses. However, as the experimental observations for the stringers were extracted from a large set of extraction locations, the average stress over all the extraction location would not be too sensitive to the exact placement of the strain gauges. This and the relatively low imperfection sensitivity of average stress, it is unlikely that the two reasons stated above would cause the deviation from the experiments as seen in the FE model. However, for stringers, there is another source of uncertainty in the stresses, which is the boundary condition at the ends of the cylinders. It was discussed in subsection 4.3.1, that fixing the axial movement of the loaded end does not allow the stringer to be loaded in compression. Looking at the image of the testing jig (see Figure 3.3), it is possible that there was some restriction on the axial movement of the loaded end, which could have reduced the compression load in the stringers. This restriction could have reduced some amount of compression from the stringers.

4.4.3. Remarks

The differences between the experimental results and the results of this study are reasoned to arise from two main sources. First is the inaccurate modelling of known parameters and the second source are the uncertainties on experimental data, such as exact positions of strain gauges (Figure 4.33). It is believed that the latter is the main source of deviation for the stresses with relatively small modelling errors resulting mainly from the finite element mesh. For the stringers, the main source of deviation seems to arise from the unknown imperfection a speculated unknown restraint provided by the testing jig at the loaded end, given its significant effect on the loading of the stringers. For the rings, the uncertainty caused by the unknown positioning of strain gauges is even higher given that there were only three locations where the stresses were extracted from. Despite this, remarkable correlation was seen assuming the

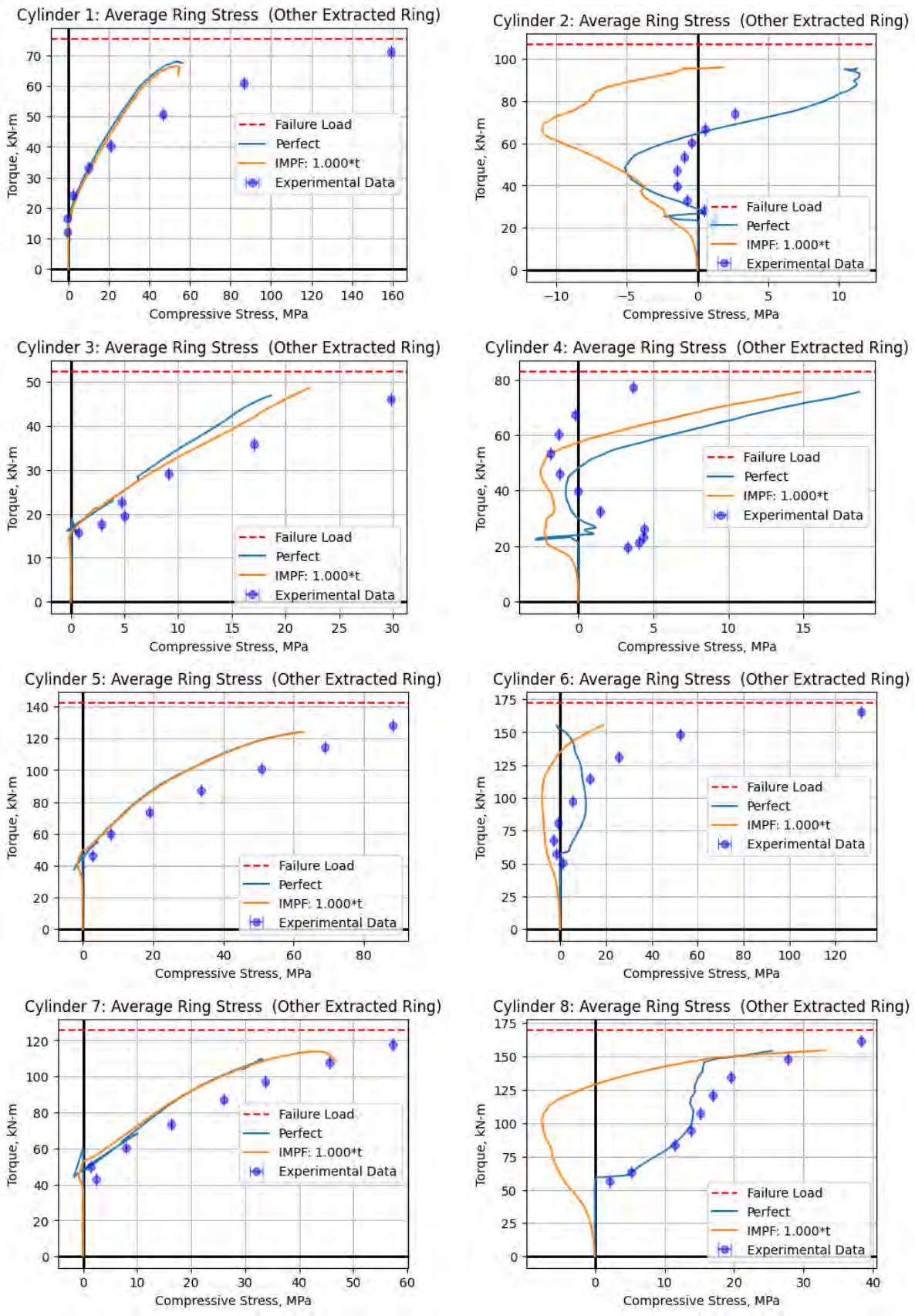

Figure 4.32: Comparison of virtual testing and experimental testing results for the ring stresses in the second extracted ring in all cylinders.

extraction location was in the middle of the bays. Additionally, in both cases, there is significant effect of imperfections on the developed stresses, which cannot be exactly recreated because the imperfections was not measured. Furthermore, the exact material properties used in the experiments was not reported, and the Ramberg-Osgood relationship might not represent the plasticity accurately.

The observations made in this study emphasise the need for accurate experimental data to be reported for development of more accurate virtual testing models. The exact locations of the strain gauges and the detailed description of the testing setup are essential to recreate the results in any complicated structure. And specifically for the case of diagonal tension, in the view of sensitivity to imperfections, efforts should be made to measure and report the imperfection field. Taking into the account the uncertainties from the experiments and enough confidence in the modelling of known parameters as some insensitive outputs (like ring stresses for cylinders 1 and 5) closely match the experiments, the following conclusion may be made. While the virtual testing approach cannot be judged completely validated, the results are within the range of possibilities created by the unknowns to warrant its use to study the load transfer mechanism in diagonal tension, which will be discussed in the coming chapter.

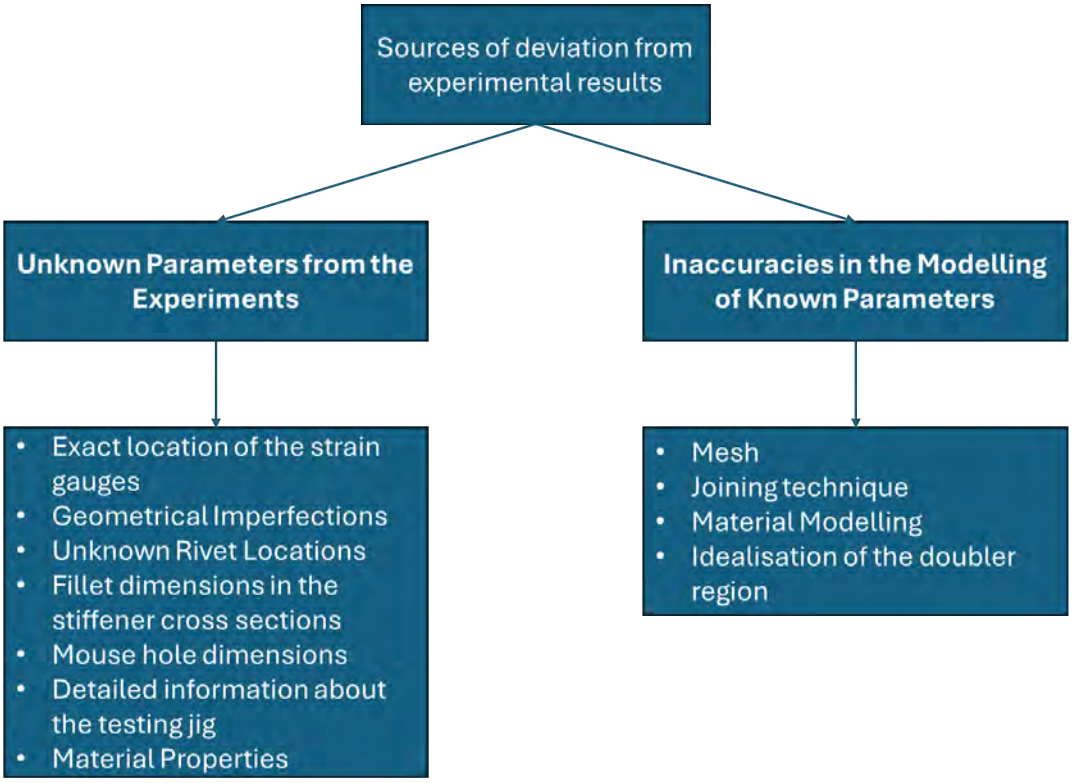

Figure 4.33: Sources of deviation of the FEA results from the experimental results

5

Loading of the Stiffeners under Diagonal Tension

The last chapter concluded with the establishment of a virtual testing framework that could be used for the analysis of load transfer in diagonal tension. The main loads generated in diagonal tension is the compression in the stiffeners which are known as primary loads, and there are loads that act transverse to the axes of the stiffeners causing bending known as secondary loads. In this chapter, a post processing approach is developed based on the ”Free Body Cut” feature in ABAQUS CAE [35] that will be used to calculate the force and moment distribution in the stiffeners. The extracted distributions will then be analysed to gain a better understanding of the load transfer mechanism under diagonal tension.

5.1. Post-Processing Approach

The detailed stress analysis of any structural element involves the extraction of their internal loads, which are the axial and shear forces, and the bending and torsion moments. The following focuses on the stiffening elements of the stiffened cylinders being investigated: stringers and rings. A post processing methodology is developed to reconstruct the internal forces and moments at any cross section of a stiffener, based on outputs that are already available in commercial finite element software. In ABAQUS, section forces (SF), section moments (SM) and element coordinates can be readily extracted, and are defined as follows [35],

$$(SF1, SF2, SF3, SF4, SF5, SF6) = \int_{-\frac{h}{2}}^{\frac{h}{2}} (\sigma_{11}, \sigma_{22}, \sigma_{12}, \sigma_{13}, \sigma_{23}, \sigma_{33}) dz \tag{5.1}$$

$$(SM1, SM2, SM3) = \int_{-\frac{h}{2}}^{\frac{h}{2}} (\sigma_{11}, \sigma_{22}, \sigma_{12})\ z\ dz \tag{5.2}$$

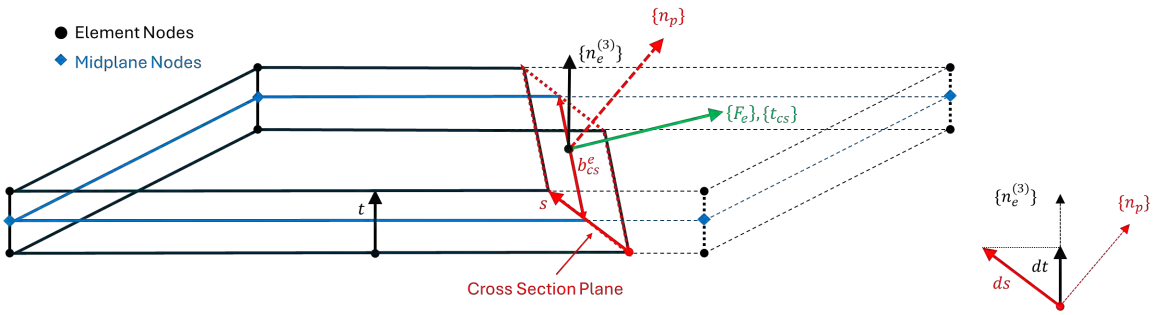

Figure 5.1: Forces on the cross section of an element

where, h is the thickness of the element

For any element intersected by a plane, the traction on the element cross section, $\{t_{cs}\}$ on the cross-section surface can be calculated from the stress tensor, $[\sigma_e]$ and the normal unit vector to the plane, $\{n_p\}$ as follows (refer Figure 5.1),

$$\{t_{cs}\} = [\sigma]\{n_p\} \tag{5.3}$$

The total force on the cross section due to the element, $\{F_e\}$ can be calculated assuming that the stress is constant over the width of the cross section (which is a fair assumption for linear elements with a single integration point as used in this study) using the following integration,

$$\{F_e\} = \int_{A_e} \{t_{cs}\} dA = \int_{-\frac{s}{2}}^{\frac{s}{2}} [\sigma_e]\{n_p\} b_{cs}^e ds \tag{5.4}$$

where s is the thickness along the cross section, and b_{cs}^e is the width of the cross section.

Knowing the direction cosine in the thickness direction of the element ($\{n_e^{(3)}\}$), the relationship between s and t can be established as follows:

$$ds = dt \frac{1}{\sqrt{1 - (\{n_e^{(3)}\} \cdot \{n_p\})^2}} \tag{5.5}$$

Thus, the force can be written as:

$$\{F_e\} = \int_{-\frac{h}{2}}^{\frac{h}{2}} [\sigma_e]\{n_p\} b_{cs}^e \frac{1}{\sqrt{1 - (\{n_e^{(3)}\} \cdot \{n_p\})^2}} dt \tag{5.6}$$

Combining Equation 5.6 and Equation 5.1, the total force on the element cross section can be calculated from ABAQUS field output as shown below,

$$\{F_e\} = \frac{b_{cs}^e}{\sqrt{1 - \left(\{n_e^3\} \cdot \{n_p\}\right)^2}} [SF_e]\{n_p\} \tag{5.7}$$

where,

$$[SF_e] = \begin{bmatrix} SF1 & SF3 & SF4 \\ SF3 & SF2 & SF5 \\ SF4 & SF5 & SF6 \end{bmatrix}$$

Similarly, the moment on the mid-plane of the element can be calculated using the following integral (t is length along the element normal),

$$\{F_e\} = \int_{-\frac{h}{2}}^{\frac{h}{2}} [\sigma_e]\{n_p\} b \frac{1}{\sqrt{1-(\{n_e^3\}\cdot\{n_p\})^2}} \, t \, dt \tag{5.8}$$

Combining Equation 5.8 and Equation 5.2, and assuming that the moments due to variation in out-of-plane stresses are negligible, the total moment of the element cross section can be calculated from ABAQUS output as follows,

$$\{M_e\} = \frac{b_{cs}^e}{\sqrt{1 - (\{n_e^{(3)}\} \cdot \{n_p\})^2}} [SM_e]\{n_p\} \tag{5.9}$$

where,

$$[SM_e] = \begin{bmatrix} SM1 & SM3 & 0 \\ SM3 & SM2 & 0 \\ 0 & 0 & 0 \end{bmatrix}$$

If there are 'N' elements in the cross section, the total force on the cross section can be calculated by summing the contributions due to all the elements in the stiffener that are intersected by the plane (The intersection of a plane with a set of elements in the stringer is shown in Figure 5.2),

$$\{F_{cs}\} = \sum_{i}^{N} \{F_e^i\} \tag{5.10}$$

To calculate the moments with respect to a point on the cross section, the contribution of the elements' cross section force and moments can be summed over 'N' elements as shown below,

$$\{M_{cs}\} = \sum_{i}^{N} \left(\{M_e^i\} + \{r_e^i\} \times \{F_e^i\} \right) \tag{5.11}$$

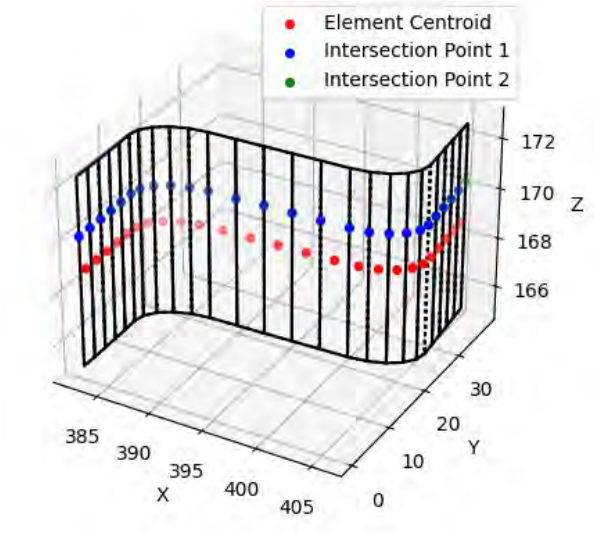

Figure 5.2: Visualisation of the calculation of intersection points in the custom post processing script. Image shows the intersection of a plane with a set of elements of the stringer.

5.2. Analysis of Primary Loads

To visualise the load transfer in the cylinders, Figure 5.3 shows the free body diagram for the cylinders before and after buckling assuming a pure and uniform diagonal tension field in the cylinders. The three squares show the skin bays with the rightmost one showing the bay with doubler that is present at the ends of the cylinders. The horizontal and vertical rectangles show the stringers and rings adjoining each bay. Note that the diagram considers the skin below the stiffeners to be a part of the stiffeners.

In the unbuckled case, along all the edges of the skin, the load transfer is due to the shear in the skin. There would be an effect of the stiffeners acting like a frame structures but that is neglected in the figure. Thus, before buckling there is no forces introduced except those that arise due to the frame action of the stiffeners. After post-buckling, the buckled skins would develop a diagonal tension field, which is shown by the green diagonal arrows. In reality, it would be a combination of the pure shear and diagonal tension. Kuhn et al [1] use an analogy between the stringers and rings of a diagonal tension cylinder to the flanges and uprights of a diagonal tension beam to derive the theory for primary stresses assuming uniform diagonal tension. The stiffeners get loaded due to the diagonal tension field trying to pull the adjacent stiffeners closer to each other, which will be counteracted by the stiffeners in the orthogonal direction. The assumption of pure diagonal tension enforces a condition of uniform traction applied on the stringers which makes the compression in the stiffeners uniform and does not introduce any secondary bending on them. In reality, due to significant pure shear action and the flexibility of the stiffeners, there would be secondary bending effects and local variation in the axial stresses. These effects are not well understood and analogous formulae to flat webs were used to correct for the supposed local variations.

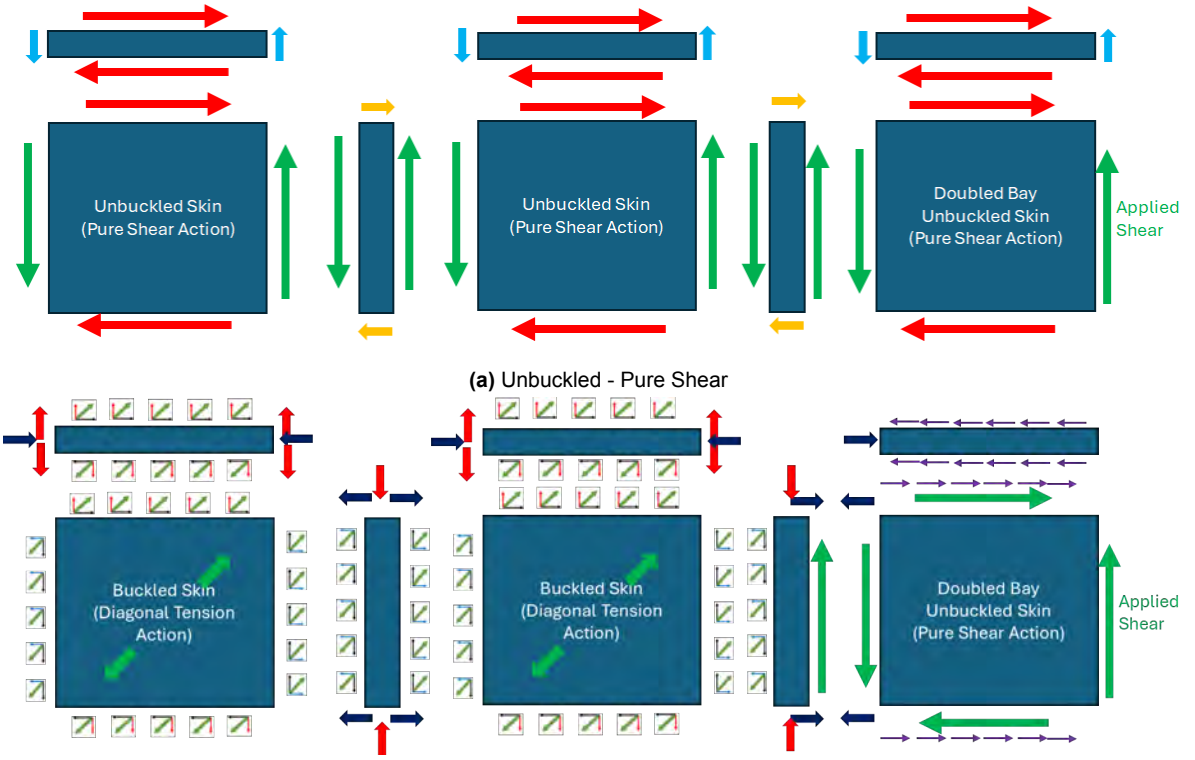

(a) Unbuckled - Pure Shear

(b) Buckled (pure and uniform diagonal tension in the buckled bays)

Figure 5.3: Free body diagram of in-plane forces for different skin bays and stiffeners of the cylinder

The virtual testing model developed in the previous section provides and opportunity to understand these effects more in depth. For the analysis, results from the perfect cylinders were used so because the exact imperfection is unknown. Given the imperfection sensitivity of the stresses, performing the loads analysis on them would add an effect of unrealistic imperfections. The results presented here are generated using the model with the same mesh which was considered converged in the previous chapter, which was indeed found to be converged for the axial loads as is discussed in section C.2 of Appendix C.

Implementing the post-processing approach laid out earlier in Python, the free body forces on the stringer was calculated at uniformly spaced cross sections along the length of the stringer. This allows the visualisation of the axial force, the shear force components, and the bending and twisting moments all along the stringers. Analysing these forces as the load on the cylinders are increased, provides insights into the load transfer mechanism, especially the local variation of the loads. The force and moment distributions were compared to the deformation pattern on the skin of all cylinders with the aim of finding a correlation with the load distribution. The discussion is split into two parts. This section discusses the primary loads, which are the axial compression in the stringers and the rings. Furthermore, the special case of cylinders with ends restricted from moving in the z-axis are discussed to gain further insights. The secondary loads that cause the bending of the stiffeners are discussed in the next section.

For easier readability of the graphs presented in the upcoming sections, it was decided to

normalise the torque with the buckling torque calculated from the non-linear analysis as seen in Table 4.1. It is also recommended to look at Appendix E that show the section force distribution over the skin for all cylinders and a corresponding graph for the radial deformation of the skin.

5.2.1. Stiffener Axial Loads

The axial load distribution on the stringer (along the z-axis of the cylinder) can be seen in for all cylinders in Figure 5.5. For all the cylinders the first curve corresponds to the stresses in an unbuckled state and shows essentially unloaded stringers. After buckling,it can be observed that most of the stringer is loaded under compression, which increases as the torque increases. For all cylinders, it is evident that the absolute peaks occur at the locations of the rings. However, the load distributions differ significantly from each other and may be classified into three categories. The first being the 4-ring cylinders that show highest compression in the middle bay, with the peaks at the ring locations being essentially equal in magnitude. For the 7-ring cylinders, two cylinders (2 and 4) show an overall maximum at the middle-most ring (Ring-4). Finally, there are two cylinders (6 & 8) that show compression increasing and decreasing in alternate bays. Furthermore, the local variation in the loads become stronger for cylinders 1 to 5 and 7, but conversely, seem to reduce for cylinders 6 and 8.

The loading mechanism for the overall compression of the stringers seems consistent with the theory of curved diagonal tension [27, 28, 1], whereby the diagonal tension field in the post-buckled skin pulls the rings closer to each other (as it can be seen at the last ring in Figure 5.3b). But due to the stringers resisting this action, they become loaded in compression. The increase in the compression from the ends of the stringers to the first ring location can again be explained by the fact that the diagonal tension effect tries to contract the cylinder skin axially. Due to the boundary condition, the loaded end of the skin is free to contract in the axial direction. And because the stringer is riveted to it, it gets ”pulled” by the skin (and pulls on the skin simultaneously). This shows up as a gradual increase in the compression of the stringer when going from the end to the beginning of buckled region. Another phenomenon noticed is that the peak at the ring location closer to the loaded end is much smaller than the one at the fixed end. In fact, tension and compression of equal magnitude observed at these locations respectively (Figure 5.4b). The explanation lies in the circumferential bending of the stringer caused by the differing stiffness in the as shown in Figure 5.4. Due to only the bottom flange joining the skin, the bending deformation is introduced there, which causes the material at the neutral axis to compress when the ’Y’ section is bent upwards at the ring towards the fixed end and tense up when the section is bent down on the ring towards the loaded end. However, the local distribution of the stresses with the peaks at the rings is completely different to the assumption in the theory of incomplete diagonal tension, where a peak is expected at the centre of the stringer bays due do less support expected from the skin towards the middle of the bay.

The axial loads in the rings would be along the θ-direction of the cylinder. In a way similar to that of the stringers, cross sections were calculated at different θ values and the free body

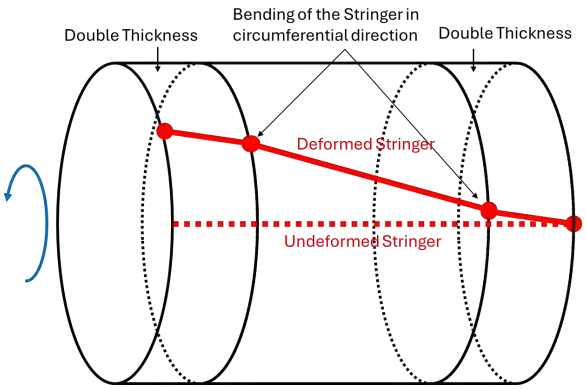

(a) Visualisation of the deformation of the stringer when the cylinder is twisted assuming uniform stiffness of the single thickness region

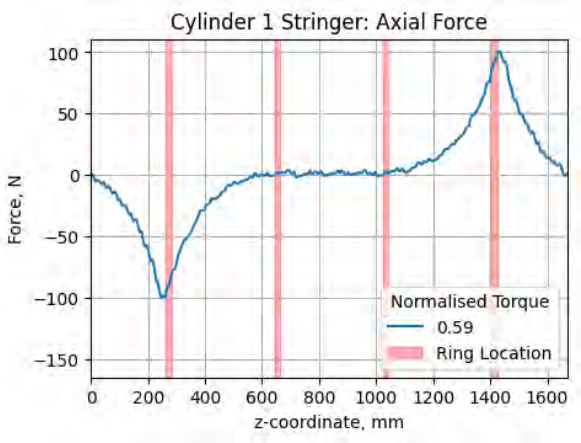

(b) The axial force distribution in the stringer before buckling

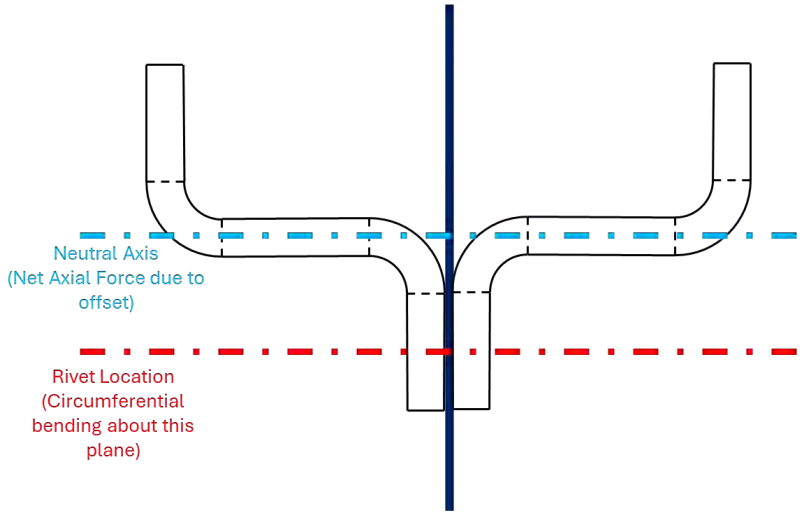

(c) Visualisation of axial force generation in the stringers at the location of change of thickness of the skin due to the introduction of the circumferential bending away from the neutral axis

Figure 5.4: The circumferential (in-plane) bending of the stringer at the location of the change in thickness

forces on them were calculated. The distribution of the ring axial forces are shown for the middle-most ring for all cylinders in Figure 5.6. It is clear that the rings get loaded after the skin buckles. After that the compression on the ring increases on average. A big difference between the results for the rings is that the compression sharply drops at the locations of the stringers. This drop is almost till zero for all the 7-ring cylinders and Cylinder-3. For the rest of them, there is some compression force at the stringer locations. This behaviour may be explained by the fact that the load transfer from the stringer to the ring does not take place all at once at the stringer location. The transfer takes place through the skin, which needs some length of the skin-ring joint to transfer the load to the ring via shear, which will be discussed further in the next section.

In a similar thread to the stringers, different distribution of the compression is seen in different cylinders. Moreover, there is a difference between the early and late post-buckling regimes. For the 4-bay cylinders, the compression peaks towards the middle of the bays and this in-

crease seems to get more drastic with increasing load. However, for the 7-ring cylinders, initially, multiple local peaks and valleys are apparent in the distribution. On increasing the loads, going into deep post-buckling, the local peaks are no longer as prominent and a peak towards the first stringer becomes apparent for all cases, except Cylinder-6 where the location of the peak in deep post buckling is closer to midway between stringers. In any case, the distribution of the loads on the ring do not seem to match the maximum in the middle assumption of Kuhn et al [1, 28], especially for early post-buckling. While the maximum is in-between the stringer locations, there seems to be significant deviation from the expected maximum right in the middle of two stringers.

As the loads on the stiffeners are provided by the skin, the deformation pattern was plotted on the skin for early and late post-buckling loads in Figure 5.7 and Figure 5.8 respectively. On a first glance, there seems to be a correlation between the deformation pattern and the load distribution on the stiffeners. It becomes apparent that any increase and decrease in the compression of the stiffeners at any location is related to the difference in deformation pattern in the skin in the adjacent bays on either side of the stiffener. This correlation is most visible for the stringer and ring loads for the cylinders with 4 rings. In all cases, there is a dominant diagonal half wave of negative radial deformation that connects on the corners that opposite along the tension diagonal. So, taking the example of the stringer, towards one ring location, there would be the main half wave adjoining on one side and on the other end, there would be the main half wave of the other wave connecting on the other side. And on the opposite side of where these half waves connect, there is very little deformation of the skin. These two adjoining regions transfer loads to the stringer differently and thus cause the local variation.

This effect of different deformation in adjacent skin bays can be seen on all stiffeners of all the cylinders. The multiple increases and decreases of the compression in the rings of cylinders with 7 rings correlates to the multiple half waves connecting on either side of the rings to create this effect. Furthermore, this effect explains the alternating increases and decreases of the compression in adjacent bays for cylinders 6 and 8. It is apparent from Figure 5.7 that there are two diagonal half waves in every bay. And for adjacent bays, the order of the inwards and outwards half waves are flipped (along the θ-direction). Due to the specific deformation pattern, within a bay on either side of the stringer there is only one of these half waves that connect (unlike for 4-ring cylinders where there were main half wave only connected towards one side of the bay). This causes monotonous change in loads in each bay. The increase and decrease in adjacent bays is explained by the fact that the order of occurrence of half waves are flipped.

The conventional understanding of the local variation in compression comes from the theory of flat diagonal tension [37] where it was postulated that the skin is able to take more compression near the corners of the bays because of the lower deformation at those locations and thus, alleviates compression from the stiffeners. The correction for the maximum stress as shown in Equation 2.15 and Equation 2.16 were originally developed for flat webs and were

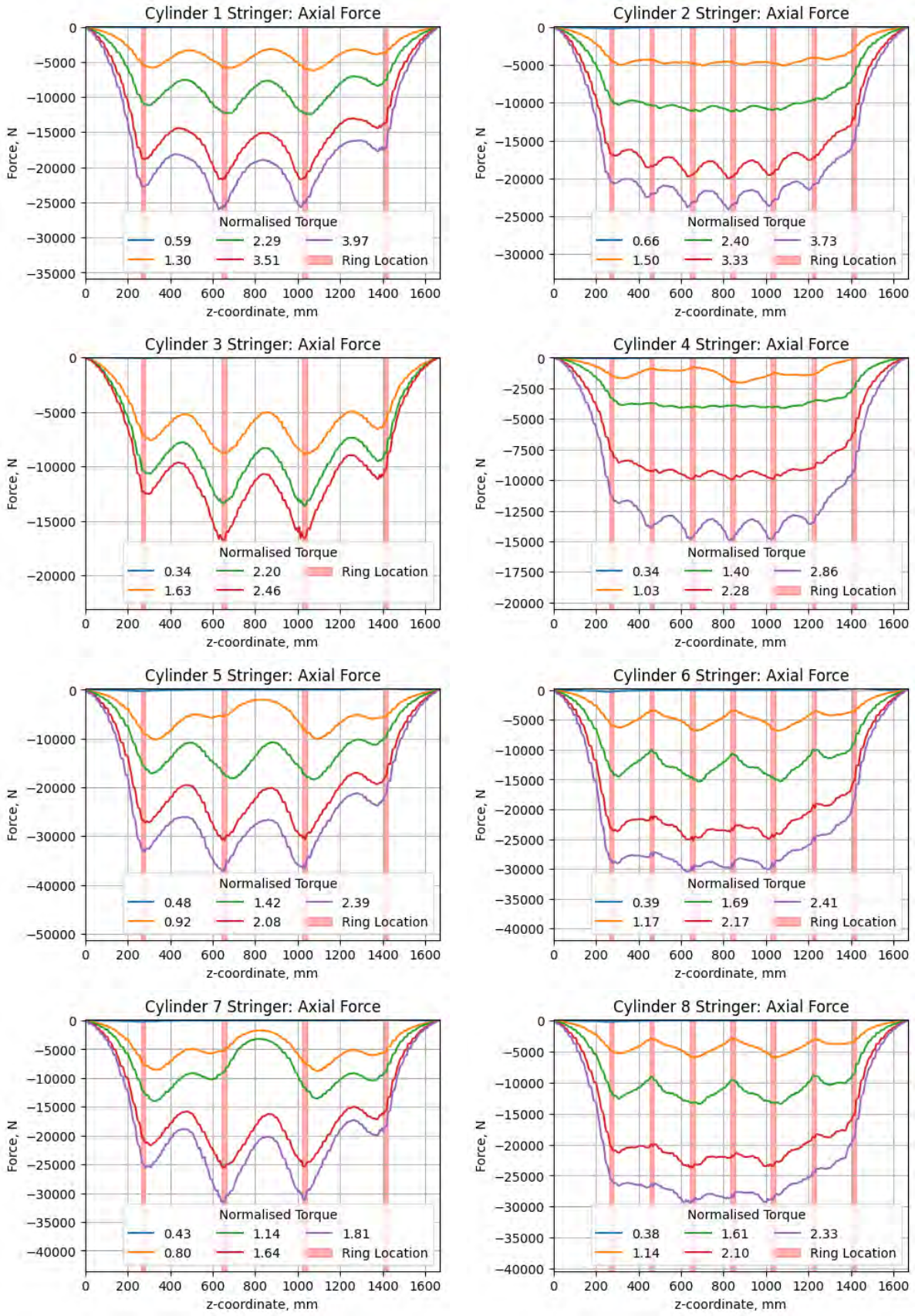

Figure 5.5: Axial force in stringer at different loads for all perfect cylinders

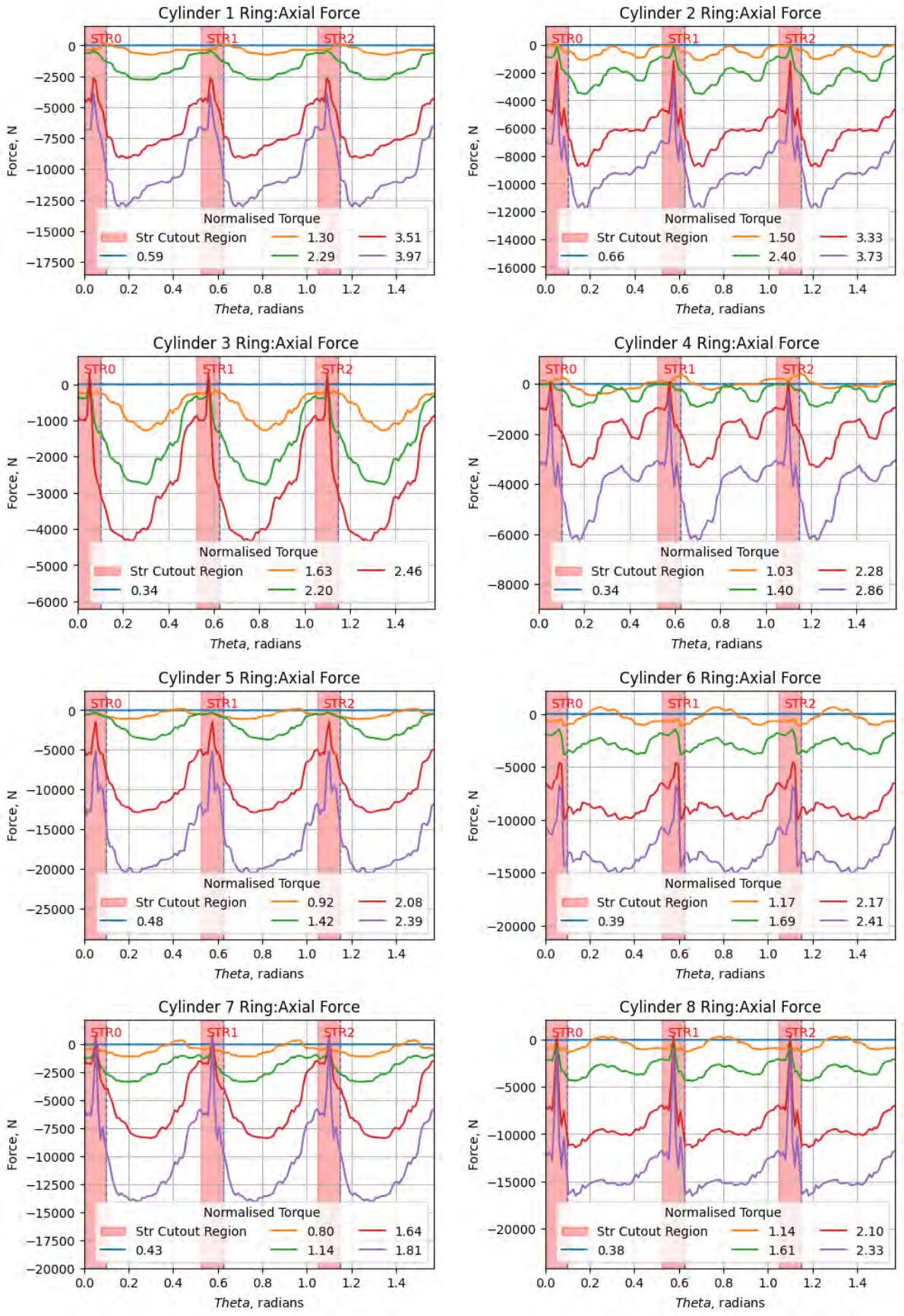

Figure 5.6: Axial force in three bays of the middle-most ring at different loads for all perfect cylinders

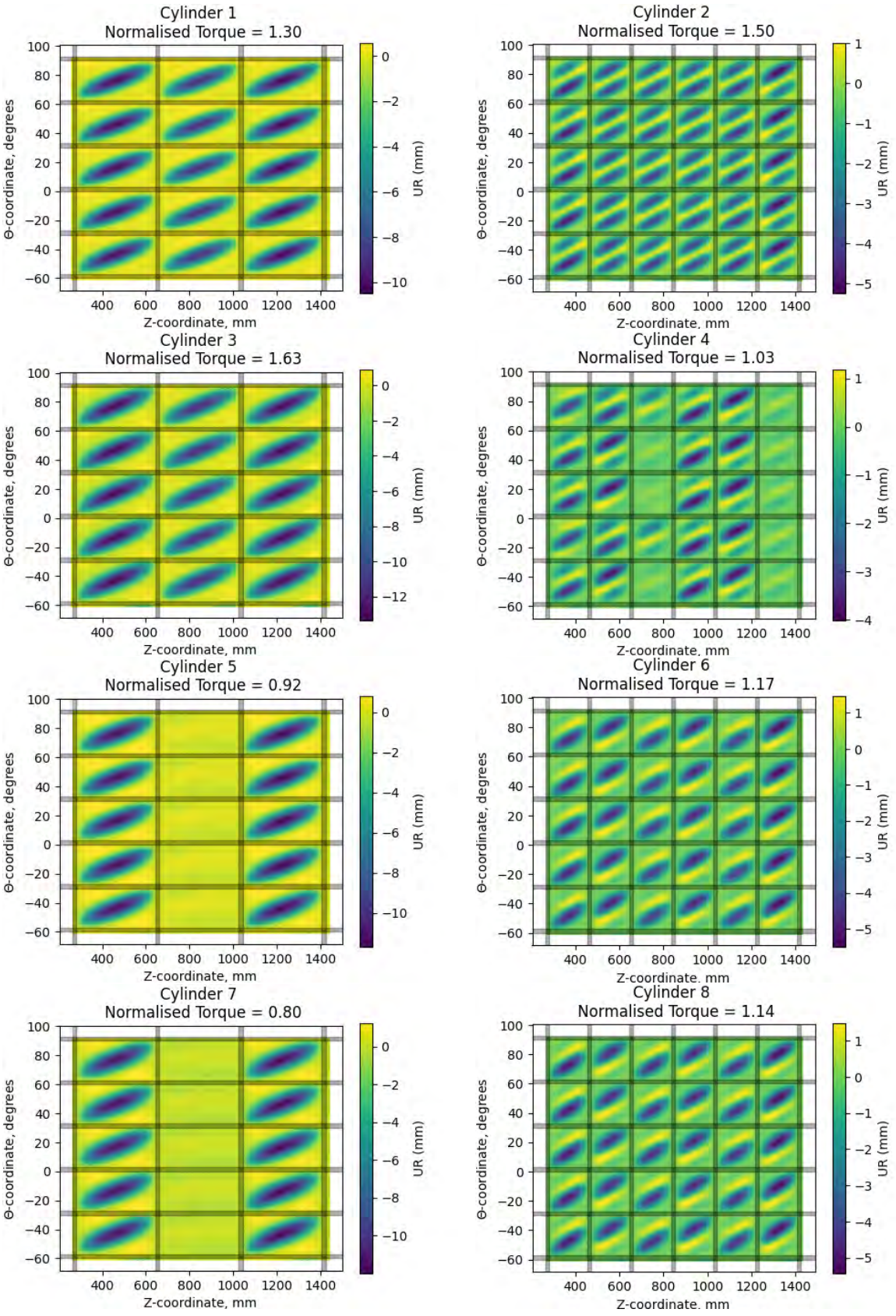

Figure 5.7: Deformation pattern on the skin during early post-buckling (Note that some cylinders show buckling only in a few bays due to the sequential buckling)

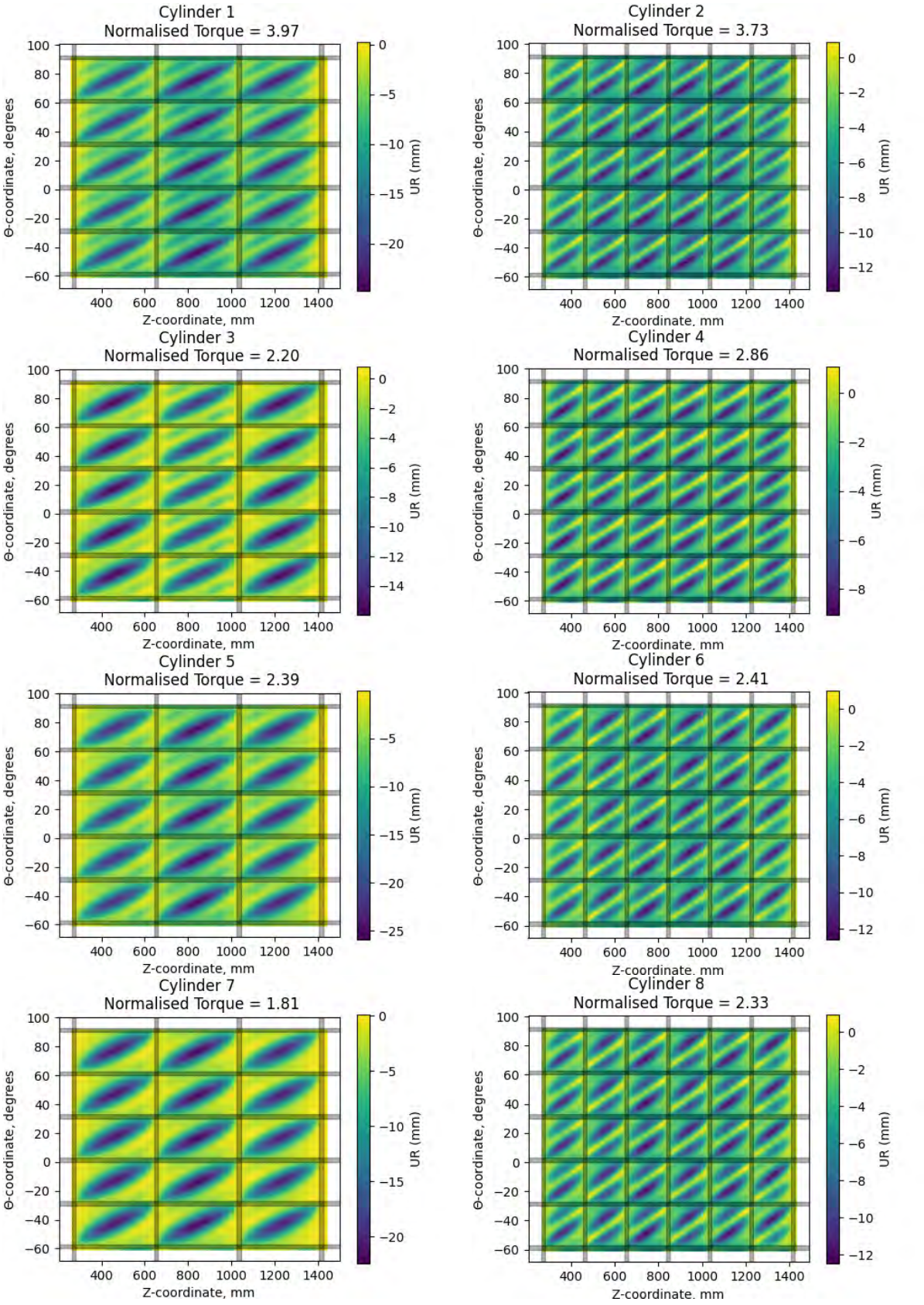

Figure 5.8: Deformation pattern on the skin during deep post-buckling

extrapolated to curved diagonal tension [1] without any presented experimental evidence. This exact behaviour and explanations seems plausible only for the case of ring loads in deep post-buckling according to the results from virtual testing, where an overall compression is seen along the whole ring with peaks in compression near the middle of the bays. However, for early post buckling, this expected behaviour is only seen in the 4-ring cylinders, whereas in 7-ring cylinders in which the middle of the bay has a minima in compression. Moreover, significant portions of the ring are in tension, which counters the traditional understanding where the whole ring should have been in compression with the reduced skin support at the middle of bay causing a minima. Furthermore, a similar explanation for the variation in stringer stresses was initially considered in this study, which correlates the fact that there is a region of low skin deformation adjacent to the middle of the stringers (see Figure 5.7 and Figure 5.8) in each bay that corresponds to a higher ”effective width” and thus explains the locally low compression at the location. However, looking at the axial loads for cylinders 6 and 8 (Figure 5.5), adjacent bays have similar distribution of the region with low deformation, but there is an overall increase/decrease in the loads all along the bay. Furthermore, a similar analysis of the cylinder with restrained axial movement (which was created during the development of the validated model) shows a similar variation of in the axial load without any significant compression (see Figure 5.9). Clearly, the explanation of the reduced compression using the effective width does not seem accurate as no tension should be generated on the stiffeners if it was accurate. So, further analysis was needed into the load transfer mechanism, which is discussed in an upcoming subsection.

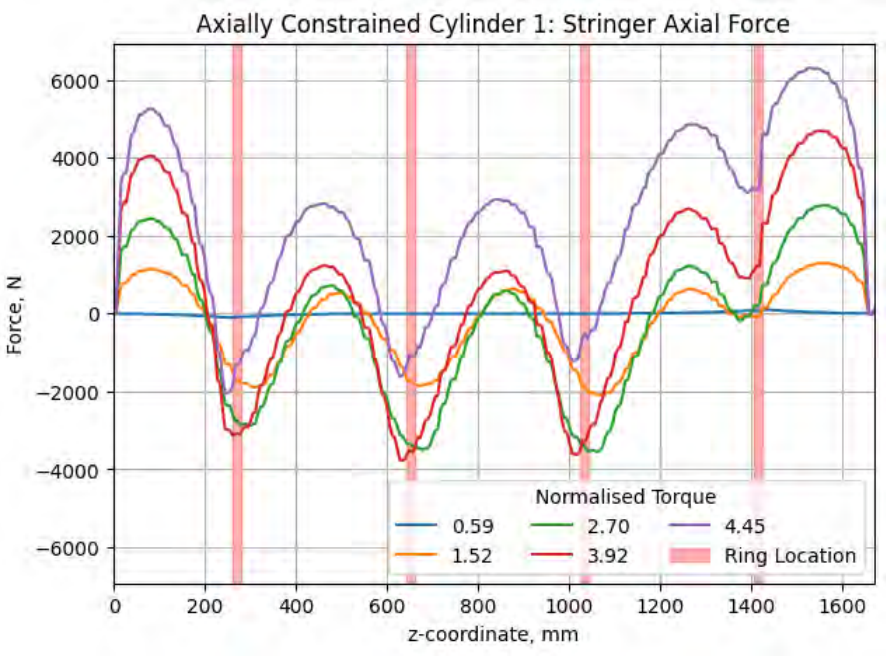

Figure 5.9: Axial force (Z-Force) on a stringer of constrained Cylinder-1 at different loads. The first curve corresponds to unbuckled state, others are under post-buckling.

5.2.2. Understanding the load transfer mechanism and local variations

The previous section discussed the axial load distribution along the whole length of the stiffeners, both in an overall sense and also looked into the local distribution. This section aims to answer the question as to how these loads are generated. The local distribution of the loads studied in the last section do not seem to conform to the conventional understanding of the load transfer mechanism. Mainly, the assumption of the compression generated by the rings being alleviated by the skin was found to not match the results. Thus, this section aims to answer two questions. First, how is the compression generated on the stringers? And second, what causes the local variation in the axial loads?

The answer to the first question is simple, and it conforms to the conventional understanding. The compression in the stiffeners are generated due to them counteracting the pull the diagonal tension field creates on the orthogonal stiffeners, which increases with loading as the tension field on the skin becomes stronger. This was clearly visible on the loads on the rings as a clear increase in the compression was seen at the stringer locations, which counteracts the tendency of the skin to contract circumferentially. For the stringers, this was seen as a sharp increase in compression at the end of the unbuckled bays, which remain on an average over the bays more-or-less constant, albeit that there is some minor increases in average loads towards the middle of the cylinder. However, results from the axially restrained cylinders provide a cautionary example for the analysis of diagonal-tension panels where the pull created by the diagonal tension field can be counteracted by factors other than the compression in the stringers, which in this case was the reaction force provided by the restraint in axial movement. In a practical case, this could mean that the pull due to tension field gets divided into compressing the stiffeners in the orthogonal directions and other load transfers such as into a very stiff boundary or into an adjacent unbuckled skin, which can attract a lot of the compression away from the stiffeners.

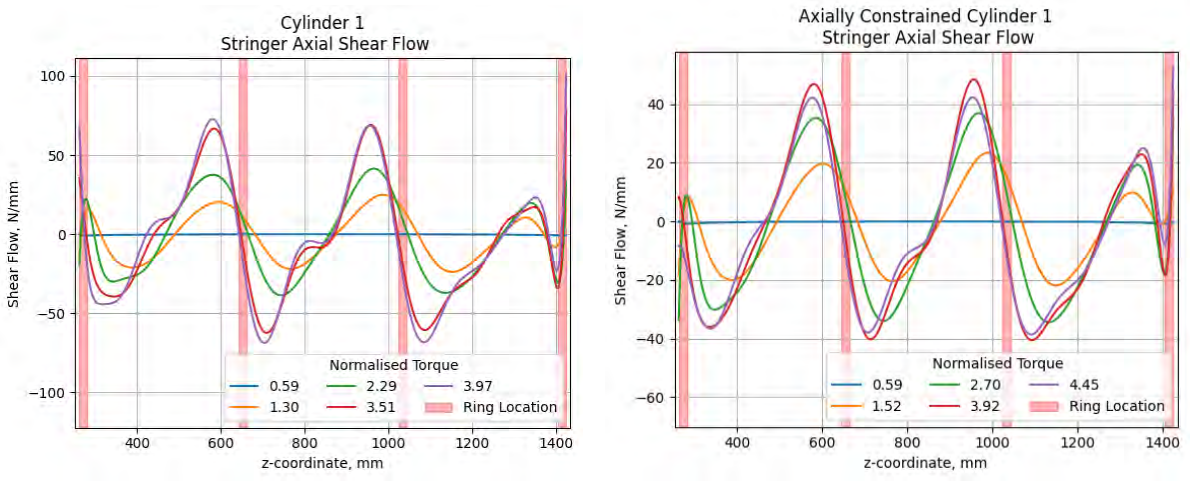

(a) Contraction Allowed

(b) Contraction Restricted

Figure 5.10: Axial shear flow introduced into the stringer due to the skin

To answer the second question, the focus of the discussion should be taken to the observation

that the changes in the axial loads correlate with the deformation pattern on the skin. For the discussion, the results from Cylinder-1 would be analysed. To visualise the load transfer better, the shear flow (q_{ax}) was calculated from the axial load distribution using the following formula:

$$q_{ax} = -\frac{dF_{ax}}{dz} \tag{5.12}$$

where, F_{ax} is the axial force.

Because the loads were introduced discretely at the rivet location and the fact that multiple cross sections over the same group of elements result in the same axial force, the distribution was stepped. So, a Fourier series with 8 half waves was fit on the data to get a smooth curve to perform the differentiation. It is to be noted that due to the loads being introduced at discrete locations of the rivets, the treatment of the shear flow as continuous is not representative of reality. However, considering that the rivets on the stringers are very closely spaced, analysing the shear flow as continuous provides a useful tool to analyse the load transfer mechanism and is representative of a limiting case of infinitely many rivets. The shear flow distribution can be seen in Figure 5.10 for Cylinder-1, both with the ends free and ends fixed along z-axis. Again, it can be seen that the shear flow only occurs after the buckling has begun and increases in magnitude as the load increases. In the first half of the bays for both cases, there is a net negative shear flow, which means that the stringer is being pulled towards the first ring, which will add tensile forces to the stringer in addition to the load that is introduced to the stringer, which we see as a reduced compression in the unrestricted cylinder and actual tension in the restricted cylinder. The shear flow in both cases are remarkably similar, although a bit higher in magnitude for the unrestricted cylinder. This observation completely negates the effective width argument for local variation adopted from results for flat webs [37, 1]. Instead, it seems like the shear flow introduced into the stiffeners is a characteristic of the curved skin under diagonal tension.

To further see the details of the load transfer mechanism, the deformation pattern and corresponding shear stress are plotted for 50% of the applied twist in Figure 5.11 and Figure 5.12. Comparing the radial displacement plots and the in-plane shear plots, it is clear that there is high in-plane shear force present in the skin wherever the deformation of the skin is low. In other regions, there is a much lower value of shear stress, and at the locations where the main diagonal half wave connects, there is a minimum of shear. Considering that the traction introduced in the axial direction of the stiffeners is due to the shear component of the stress, it becomes apparent that the differential in shear stress on the two sides of the stringers pull add shear flow from the centre to either ends of the bays, thus adding compression into the stringer. This is visualised in Figure 5.11 and Figure 5.12 where when the adjoining skin has low deformation one one side and high on the other corresponding to high and low shear section forces. In a similar manner, the shear stress along the rings add compression through shear flow from the ends of the bay to the centre, which can be seen as a small region of high negative and positive shear at the corners of the skin bays. Figure E.3 shows the shear sec-

tion force distribution for all cylinders corresponding to their radial displacement in Figure E.4 where similar correlation may be noticed.

Looking at the distribution of the principal stresses in both the cases (Figure 5.13a, Figure 5.14a), the state of diagonal tension can be understood more in-depth. The principal stress along the tension diagonals seem to have lower magnitude along the half wave where there is high deformation. Furthermore, looking into the plots for the minimum in-plane principal stresses (Figure 5.13b and Figure 5.14b), the effect of the skin can be further analysed on the loads introduced in the stiffeners. Firstly, high compression can be seen in the skin near the ring along the axis of the ring, which reduces in magnitude going closer to the middle of the ring bay. This confirms the hypothesis that the compression in the rings is developed rapidly as the load is transferred through the skin (This is also seen as spots of high compression in the circumferential section force distribution for all cylinders in Figure E.2). Furthermore, comparing the distribution of the principal stresses in the skin adjacent to the stringers between the two cylinders, it can be seen that the principal stress component in compression is aligned more with the axis of the ring and is higher in magnitude, which can also be seen in the axial section force distribution for all cylinders (Figure E.1 as bands of compression along the stringers, which would suggest an ”effective width” phenomenon. However, the very similar nature of the of the shear flow (as seen in Figure 5.10a and Figure 5.10b) along the stringers suggests that the apparent ”effective width” effect on the stringers is just due to the shear flow transfer due to the shear stress distribution on the skin.

5.2.3. Comparison with Semi-Empirical Method

Using the post-processing methodology herein developed, a better estimate for the stiffener stresses could be calculated over the entire cross section by dividing the axial forces with the cross section area [1]. The stress was averaged over the middle-most bay in the stringers and a single bay in the ring, and plotted for all cylinders along with the peak stress value respectively in Figure 5.15 and Figure 5.16, where they are compared with the expressions used in the semi-empirical where the average stress along the bay is calculated using Equation 2.12 and Equation 2.13 and the maximum stress is calculated using Equation 2.15 and Equation 2.16.

The observations may be categorised between those for 4-ring cylinders and those for the 7-ring cylinders. For the latter set, the average stress extracted from virtual testing is always higher than the values predicted by the semi-empirical method for both the stringers where the under-prediction was to the order of 20-50% and for the rings the semi-empirical method predicts almost half the values calculated from FEM. For 4-ring cylinders however, the deviation is not too high. For the stringer stresses, for some cases (cylinder 5 and early post buckling of cylinder-1) the graphs almost coincide and for other cases, there is significant under-prediction of around 30% by the semi-empirical method. The ring stresses are in the general vicinity of

[1] It is to be noted that the stresses extracted from the stringers in this way are very close to those extracted using the post-processing methodology used for validation, implying that the extraction method used for the experiments were not far from the true average over the cross section

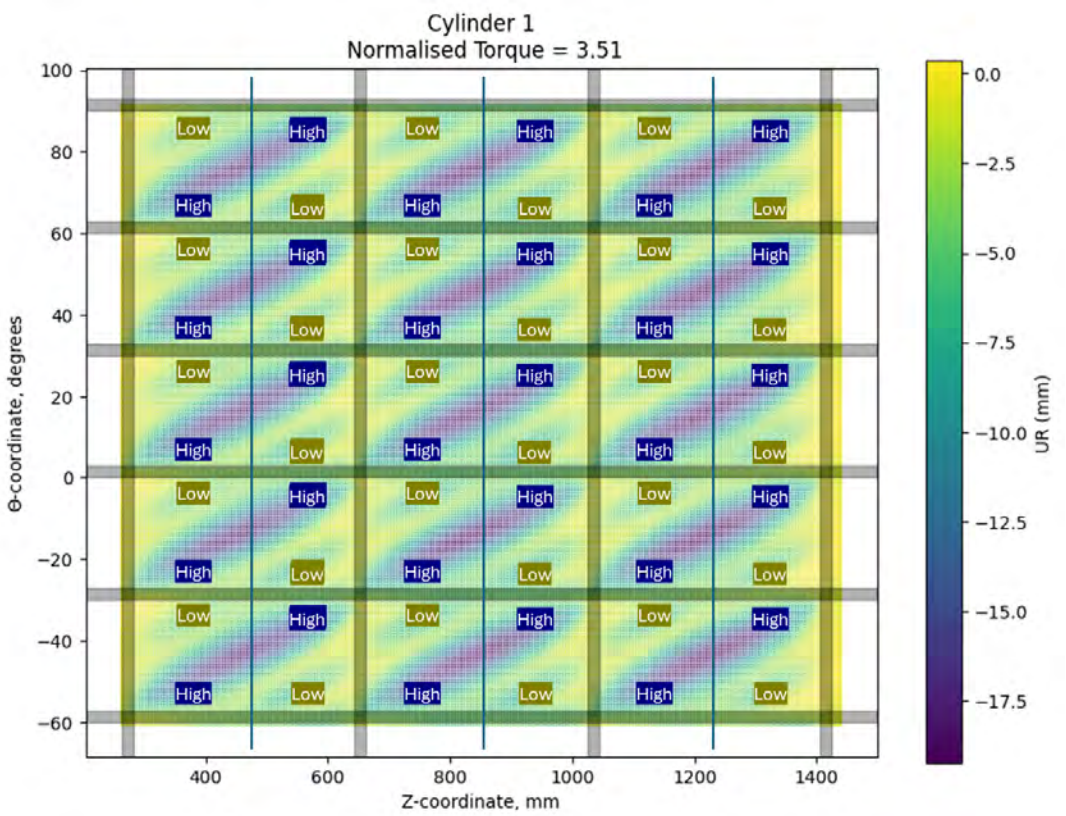

(a) Radial Displacement Contour Plot

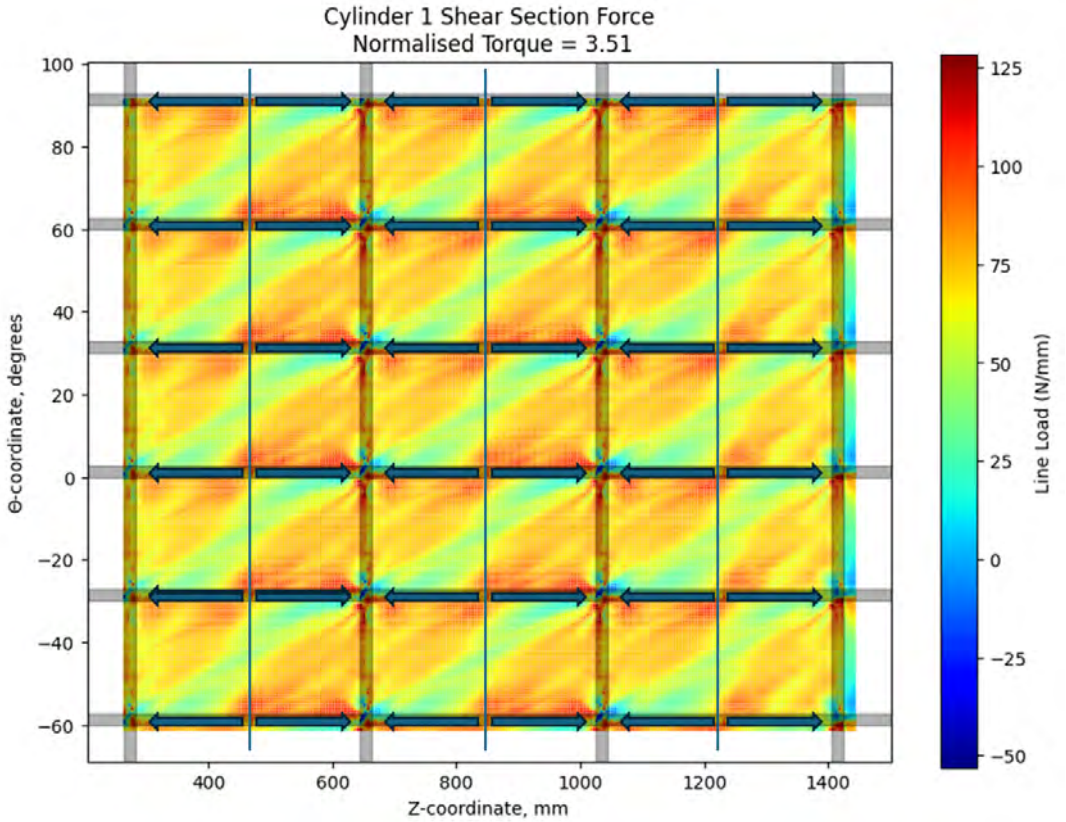

(b) In-Plane Shear Section Force Contour Plot. The arrows denote the direction of shear flow added to the stringer due to the shear section force distribution on the skin.

Figure 5.11: Load Transfer Mechanism into the stringers for Cylinder-1

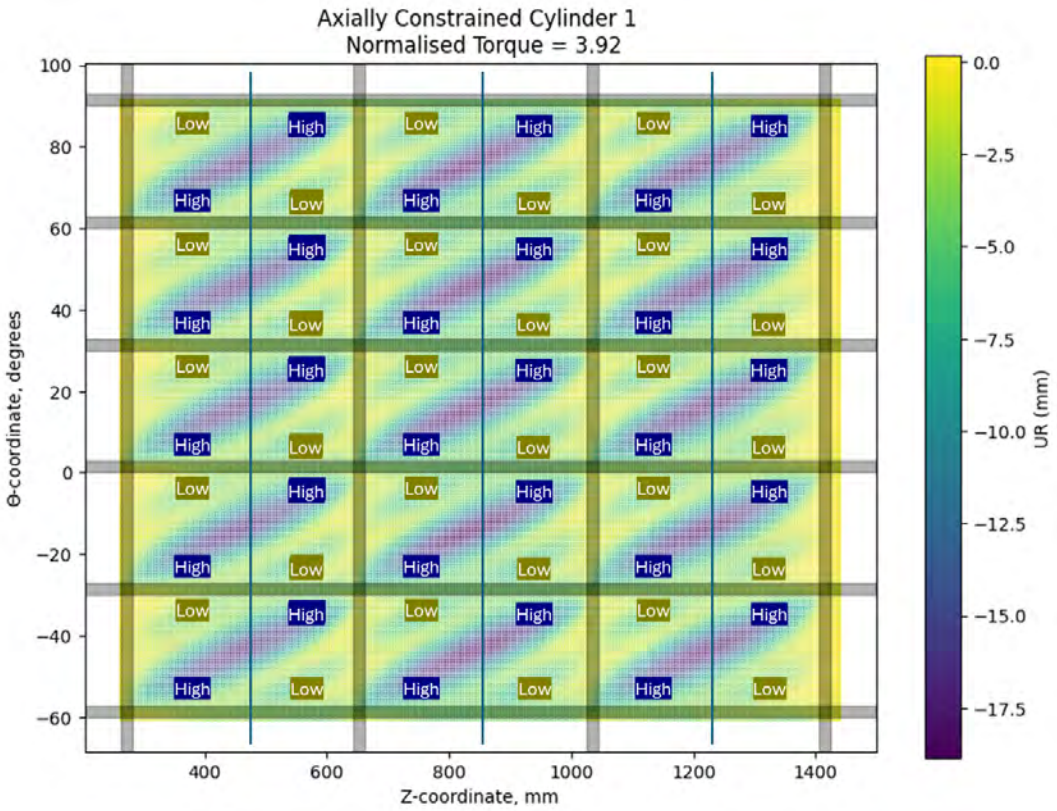

(a) Radial Displacement Contour Plot

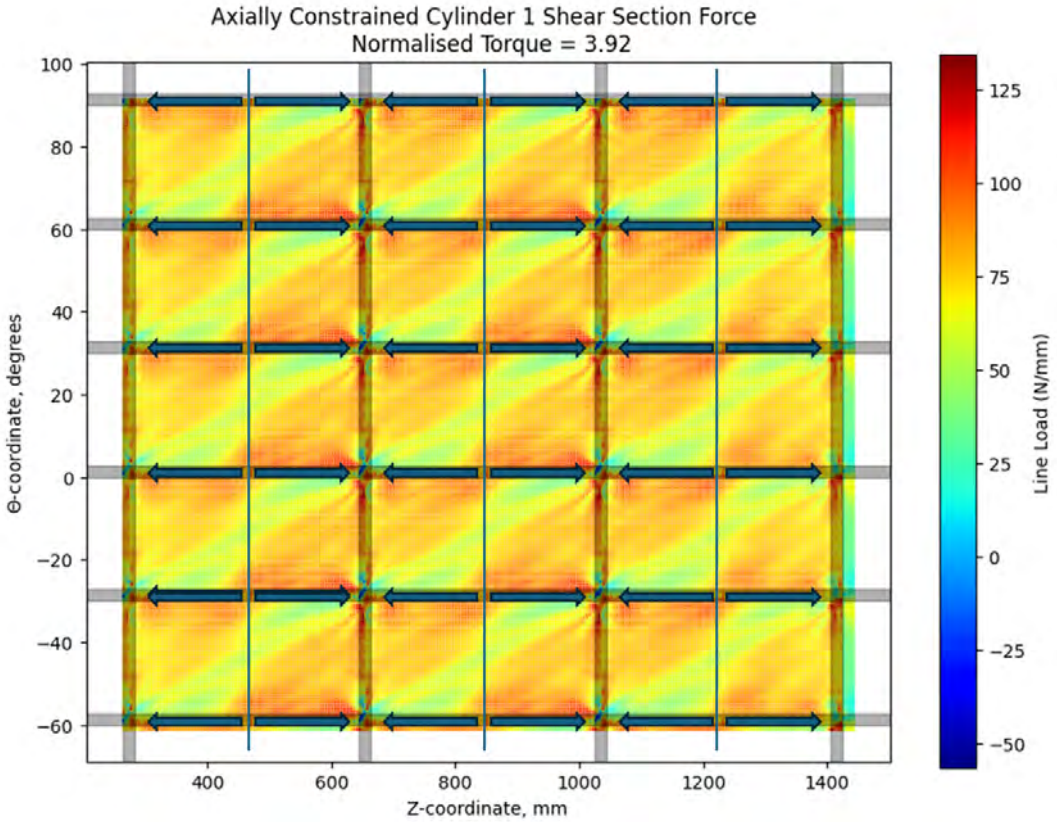

(b) In-Plane Shear Section Force Contour Plot. The arrows denote the direction of shear flow added to the stringer due to the shear section force distribution on the skin.

Figure 5.12: Load Transfer Mechanism into the stringers for Cylinder-1 with axial contraction restricted

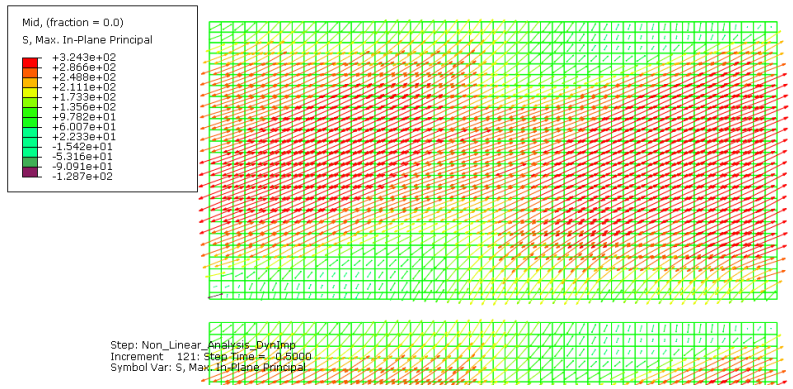

(a) Maximum in-plane principal stress

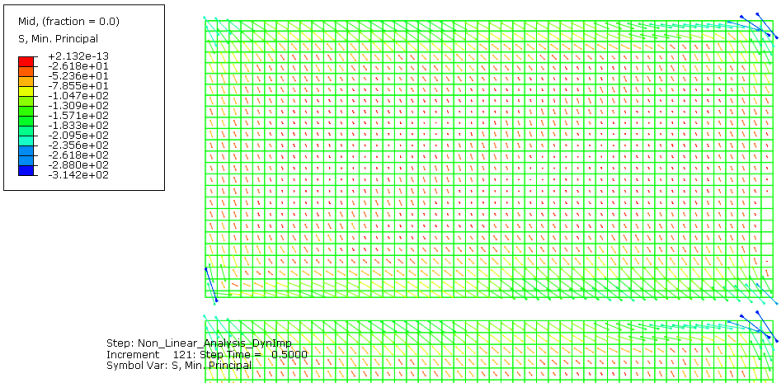

(b) Minimum in-plane principal stress

Figure 5.13: Principal Stress components in the bays of Cylinder-1. Normalised Torque = 4.47

the FEM predictions, with the semi-empirical method in general predicting higher stresses in a wide range of around 10-15% (cylinder 7) to even around 60-80% (for) than FEM until high loads are reached, when the correlation becomes better again. It is to be noted that for the stringer stresses for all cylinders and the ring stresses of 4-ring cylinders, the semi-empirical method is closer to the experimental data which is to be expected as the method was developed based on the experiments and would fit their results. However, for 7-ring cylinders, the semi-empirical method is neither close to FEM nor experiments (to be noted that experimental readings were not at the neutral axis), raising questions on the method's general applicability.

Furthermore, the correction for the maximum stress seems to be of a similar magnitude and trend in stringers of 4-ring cylinders and rings of cylinders 5-8, but are significantly different in magnitude for the rings of cylinders 1-4 and do not show the same trend in the stringers of 7-ring cylinders. In stringer of cylinders 2 and 4 there is very little difference in average and maximum, except at high loads, and for cylinders 6 and 8, the difference is maximum and average stress becomes lesser as load is increased. In the context of the observations of the local variation of axial loads, this is expected as they were found to conform more to the deformation pattern in the skin compared to the assumption of a peak at the middle of each bay.

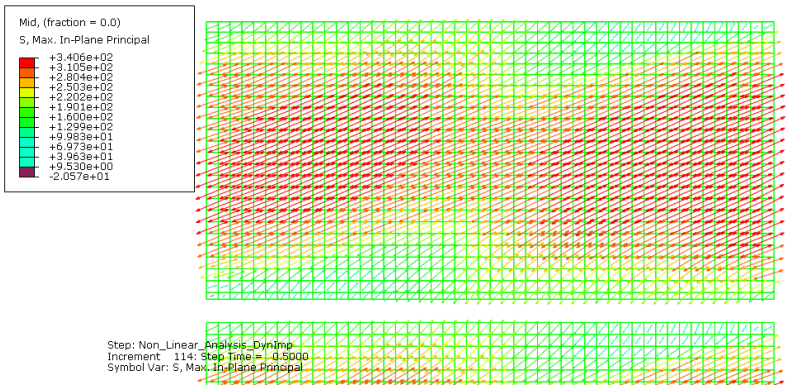

(a) Maximum in-plane principal stresses

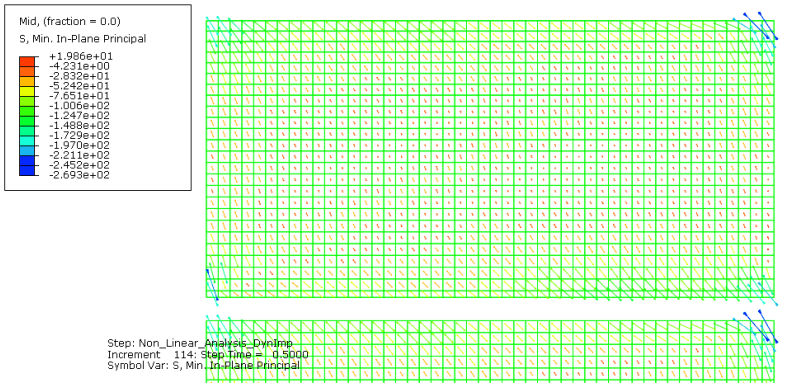

(b) Minimum in-plane principal stresses

Figure 5.14: Principal Stress components in the bays of Cylinder-1 with axial restriction. Normalised Torque = 4.99

5.2.4. Remarks

Using the developed post-processing methodology to evaluate the axial forces in the stiffeners, the load transfer mechanism was studied in-depth. From the understanding of the load transfer, the effects of the diagonal tension in the skin on the loads in the stiffeners can be separated into a global and local effect where the final loads on the stringers could be thought of as an average load created by the global effect of diagonal tension. And the local variations is caused by the local effect of diagonal tension. These effects are explained as follows:

- **Global Effect**: A bay under diagonal tension applies a pulling force on the adjacent bays. If the adjacent bays are unbuckled, or have a diagonal tension field not as high in magnitude, there is an unbalanced force on the interface between the two regions (for reference, see Figure 5.3b, where there is an unbalanced inwards pull on the ring between the unbuckled and buckled bays). This unbalanced force should be counteracted by other structural elements. For the case of the NACA cylinders, the unbalanced force was counteracted by the stringers undergoing compression and providing a reaction force; whereas for the case of the NACA cylinder with a hypothetical restriction in the axial contraction, it was the boundary condition by means of an axially-oriented reaction force (which was observed in Figure 4.27).

- **Local Effect**: The local effect of the diagonal tension refers to the variation in loads created in the adjacent stiffeners due to the shear flow transferred into them. This completely depends upon the deformation pattern that develops in the skin after local buckling, which as seen earlier, determines the shear flow transfer into the stiffeners.

From the comparison between the virtual testing results and the semi-empirical method, taking the observations at face value (assuming them to be the reality) would suggest that the semi-empirical method is in-general inaccurate and significantly un-conservative, perhaps underestimating the diagonal tension loads. However, in the view of the uncertainties related to the experimental parameters, it will be unwise to comment on the quantitative results for the average axial loads as it is unclear how close the results are to an actual experiment. However, with the backing of qualitative observations and understanding of the local variation of the axial loads as developed in the last section, the correction factor used for the calculation of the maximum stress (Equation 2.15 and Equation 2.16) may be rejected as they are inaccurate even in their predicted trends (of the maximum load to be proportional to the average). According to the developed understanding of the load transfer mechanism, any analysis of the local variation in the axial loads must take into account the deformation pattern in the skin. The last statement is bolstered by the fact that for the cylinder with restrained axial contraction, despite the small loads generated on average, the local variation was of a similar magnitude. This observation may be generalised to say that the local effect of diagonal tension is largely independent of the average axial load generated in the stringer be it from only the global effect of diagonal tension or a combination of the global effect and external loads. The last inference can be the basis for a study to better understand the stresses in a combined compression and shear loading case, where the loading on the stringers is a combination of the global effect caused by the diagonal tension and external compression.

5.3. Analysis of Bending of Stiffeners

In addition to the primary compressive loads on the stiffeners, there are secondary forces acting on them perpendicular to their axes due to the forces in the skin. For the cylindrical structures herein investigated, the shear forces acting on the stringers and rings may be decomposed into two components, one that acts radially inwards and the other that acts in the plane of the skin. Consequently, these forces create bending moments in the stiffeners. In literature, Kuhn et al (1952) [1] have discussed the effect for only the radially inwards bending of the stringer, without any discussion about the radial bending of the ring and the bending in the plane of the skin for both kinds of stiffeners (stringers and rings). In the study that is presented in this section, the developed post-processing methodology is used to calculate the shear forces and bending moment distribution in the stiffeners, which are further analysed and compared with the existing literature to establish an understanding of the load transfer mechanism. For the sake of clarity, only the results for radial bending of stringers are shown in line with the text, with the rest of them shown in Appendix D. Furthermore, the radial bending moment will be compared with the expression suggested in the NACA method. For other

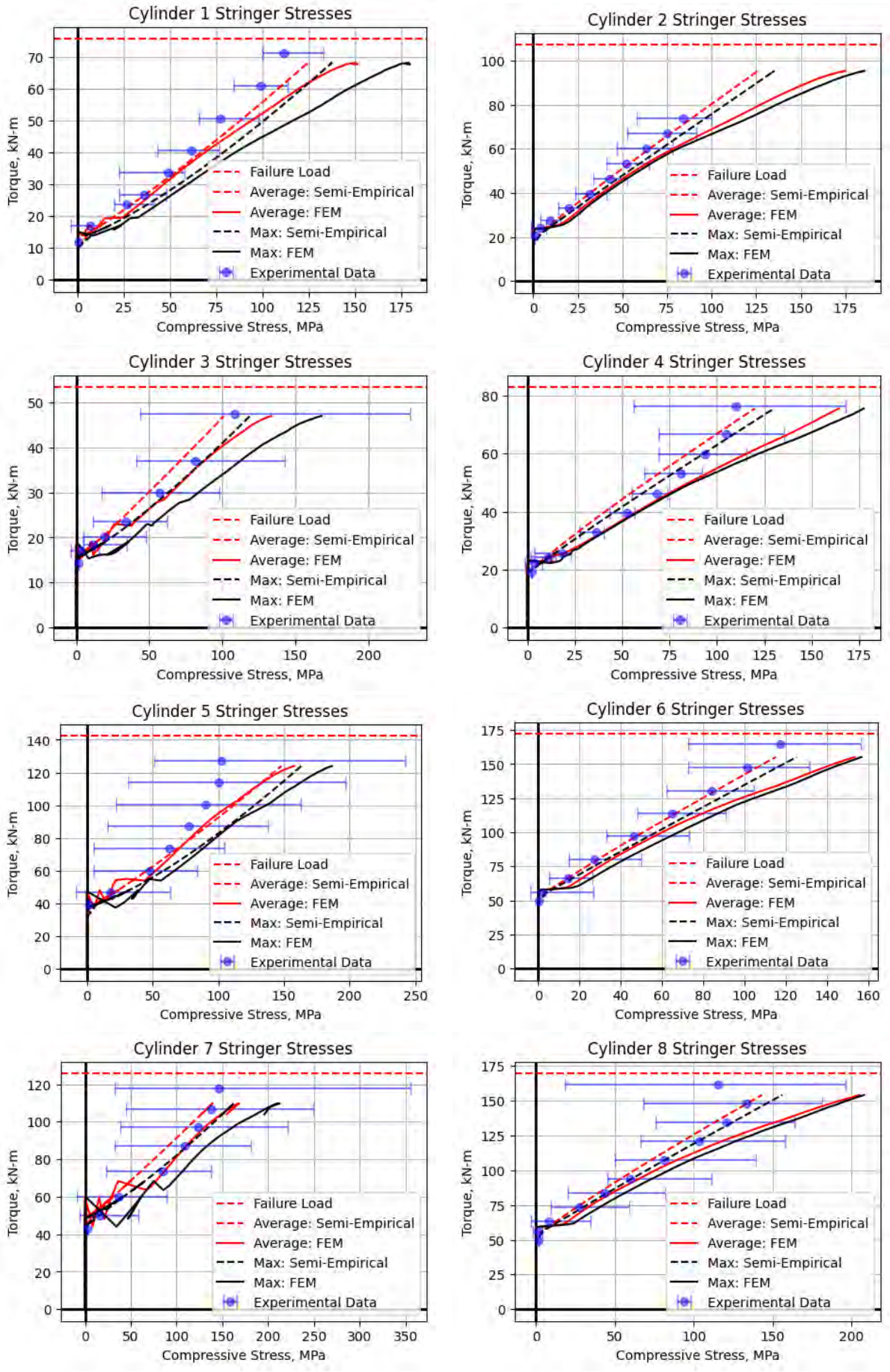

Figure 5.15: Comparison of average and maximum stringer averaged stress along the middle bay calculated by FEM and the Semi-Empirical Method

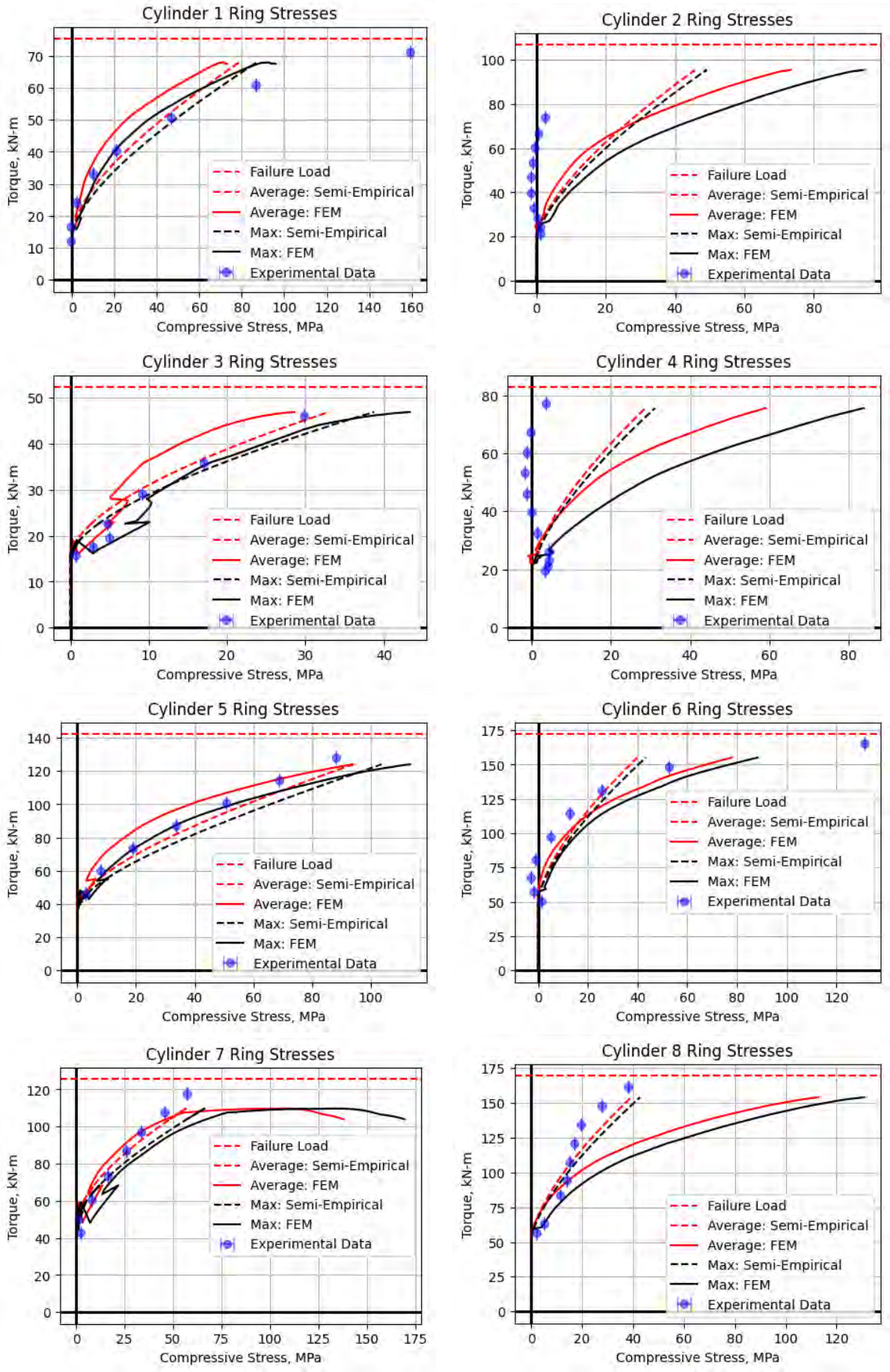

Figure 5.16: Comparison of average and maximum ring stress along the bay calculated by FEM (averaged over the whole cross section) and the Semi-Empirical Method

bending effects, only qualitative observations were made considering the significantly jagged nature of the curves due to the presence of the rivets, and due to the suspicion that the results are not fully converged for these specific outputs (the shear force and bending moments), as discussed in section C.2 of Appendix C.

5.3.1. Stringer Radial Bending

The distribution of the bending moment about the mid-plane of the skin for the stringer of each cylinder is plotted in Figure 5.17. Based on the results, some general observations may be made. First and foremost, it can be seen that the bending moment is nearly zero before buckling and only starts to increase after buckling of the skin. Second, it can be seen that for most cases, there is a distinct change in the slope of the bending moment curve at the ring locations (except for cylinder-2 under high loads, where the slope is relatively unchanged), and it mostly coincides with a local minimum in bending moment. In general, this minimum increases in magnitude as the post buckling load is increased, which indicates that there is a net bending moment along the length of the whole stringer, which is expected because there is a net inward force on the stringer due to the ”flattening” behaviour of the skin.

For the local distribution, the theory of pure diagonal tension predicts a primary peak (in magnitude) at the ring locations and a secondary peak at the middle assuming polygonal rings and that the stringer acts like a beam fixed on both ends with a distributed load applied [1]. But for a practical case, under considerations of circular rings and flexible stringers, and considering some sparse experimental data, the recommended value for the primary peak was reduced to half. Taking the maximum amplitude along the middle-most bays from the virtual testing results and comparing with the theory of pure diagonal tension and the semi-empirical method (Figure 5.19)[2], it can be seen that the correlation is bad for the 4-ring cylinders, with neither the trend nor the magnitude matching either of the expressions. The correlation is relatively better for 7-ring cylinders, with the expression from the semi-empirical method being closer to the results of cylinders . However, looking at the bending moment data from the virtual tests (Figure 5.18), it becomes clear that the location of the peaks do not match the expected primary peak at the rings and for most cases, neither the secondary peak at the middle of the bay (except cylinder 1).

Furthermore, it is also apparent that for most cylinders, the distributions are different in different bays and there seems to be an overarching trend across them. For example, for cylinders 4, 6 and 8, a smaller magnitude of the bending moment is observed towards the middle bays, for cylinders 3,5 and 7, there is maximum bending moment in the last bay, and for cylinders 2, 3, and 7, there are low moment in the middle bays. It is suspected that this global trend perhaps arises due to the different rings providing different reaction moments to the stringer. This behaviour of the bending moment distribution makes it difficult to concretely comment on the loading mechanism except the qualitative observation of a radially inward bending moment

[2]expression for pure diagonal tension uses Equation 2.24 and the semi-empirical method uses the same expression divided by 2

as it is difficult to correlate it to the skin deformation pattern.

The graphs for the shear force distribution (see Figure 5.18) in the beam provides some more insights into the loading[3]. The radial shear force distribution show in general and in most cases an overall increasing shear force in every bay[4], followed by a sharp change in shear force, which is the characteristic behaviour of a beam loaded with a distributed load. However, the increase seen is not monotonous and there are regions where the shear force decreases, which indicates a radially outwards distributed load in the region. Also, for most of the cases, the distribution in the bay changes sign somewhere somewhere in between the rings, which corresponds to the local peaks in the bending moment distribution as seen in Figure 5.20. It is precisely these zeros in the shear force distribution that are the locations of local minima and maxima for the bending moment (according to Euler-Bernoulli beam theory). For most cases, the bending moment minima coincide with the sharp decrease in the shear force at the rings. and the maxima correspond to the change in sign of the shear force seen at some location between the rings.

The exact distribution has a varies significantly between cylinders as location of the maxima is different for different cylinders. In a very egregious case, for cylinder 2 (see Figure 5.21), the maxima in every bay is very close to the ring towards the loaded end (corresponding to a sharp increase in the shear force). This suggests that the deformation pattern in adjacent skin panels affects the radially inwards loading. Moreover, there is a notable difference in the distribution in different bays that is most apparent for the 7-bay cylinders, with cylinders 2 and 4 being the most egregious. For cylinder 2, careful observation of the drops in shear force distribution suggest that different rings provide different magnitudes of support counteracting the inwards bending, suggesting that in addition to the local deformation pattern, there is a deformation pattern of the cylinder as a whole that dictates the inwards bending of the stringers. In fact, a cumulative effect of these two phenomena can be seen in cylinders 6 and 8 where the apparent ”flipped” nature of the deformation pattern on the skin in adjacent bays (Figure 5.8) seem to correlate with the roughly anti-symmetric trend of shear force distribution about any ring (Figure 5.18). It was attempted to correlate the skin deformation pattern to the shear force distribution however, no detailed correlation could be established as seemingly similar deformation patterns in the 4-ring cylinders result in vastly different shear force distributions.

In the view of the above discussion, it becomes apparent that the bending moment and to a slightly lesser extent, the shear force distribution on the stringers can be influenced by the deformation pattern on the skin, both along the whole cylinder and also locally. Under this consideration, for any analysis of the stringer, it becomes unwise to use an expression for the

[3]An analysis using the idealisation of the load transfer as a line load distribution would be a better way to visualise the loads, given that the stringer has a high density of rivets (calculated by differentiating the shear force along the length, as done for the axial loads). However, due to the stepped and jagged nature (due to the presence of rivets, exacerbated due to the sharp changes at the ring locations) of the curve, numerical differentiation could not be done as a good fit could not be found for the data using either a polynomial or a Fourier series.

[4]This might be difficult to note for Cylinders 2 and 4 given their varying distribution over different bays, but there is always a net positive increase from the end of the drop at the location of the first ring to the start of the drop of the second ring

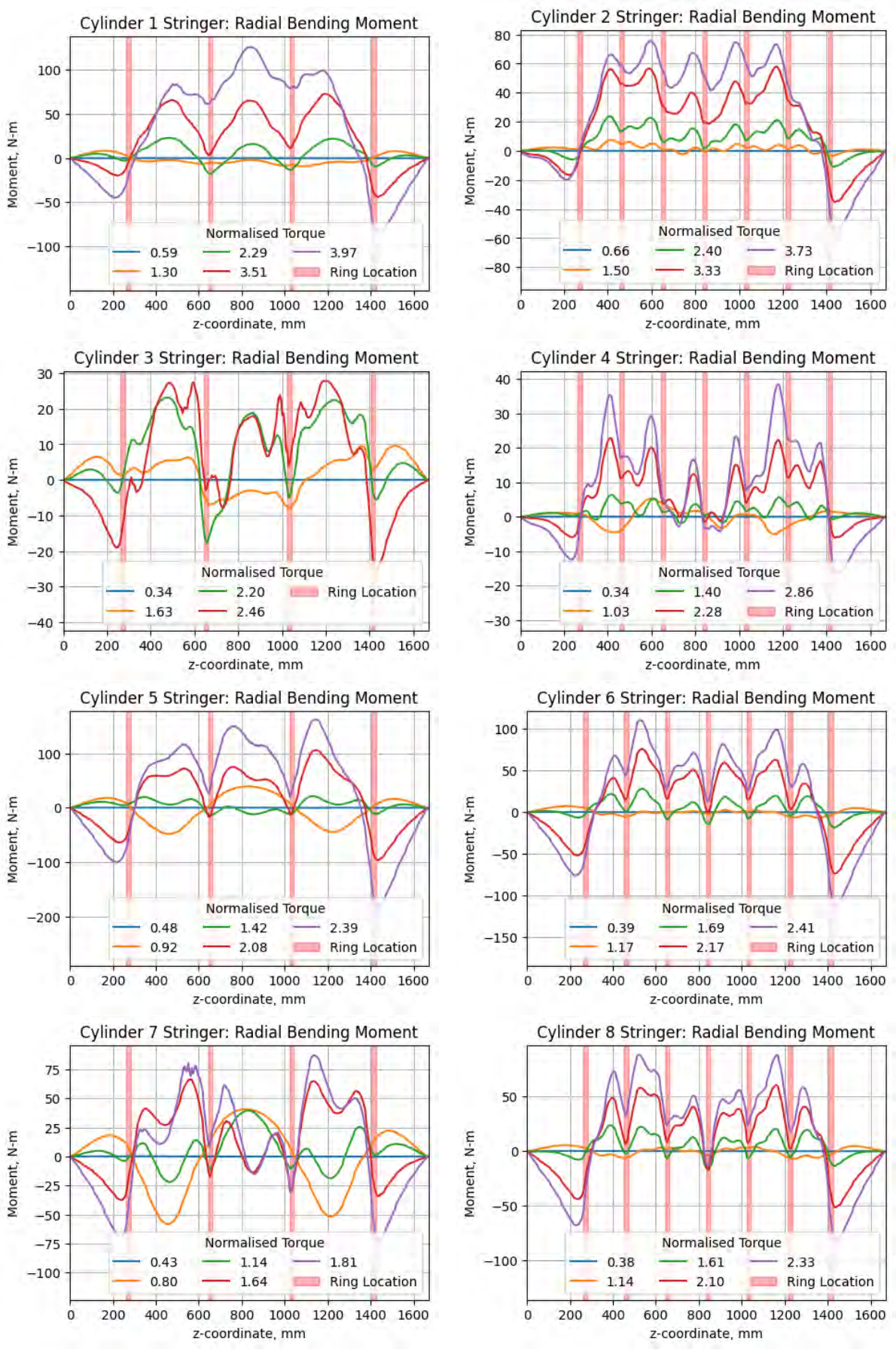

Figure 5.17: Radially inwards bending moment in the stringers at different loads for all perfect cylinders

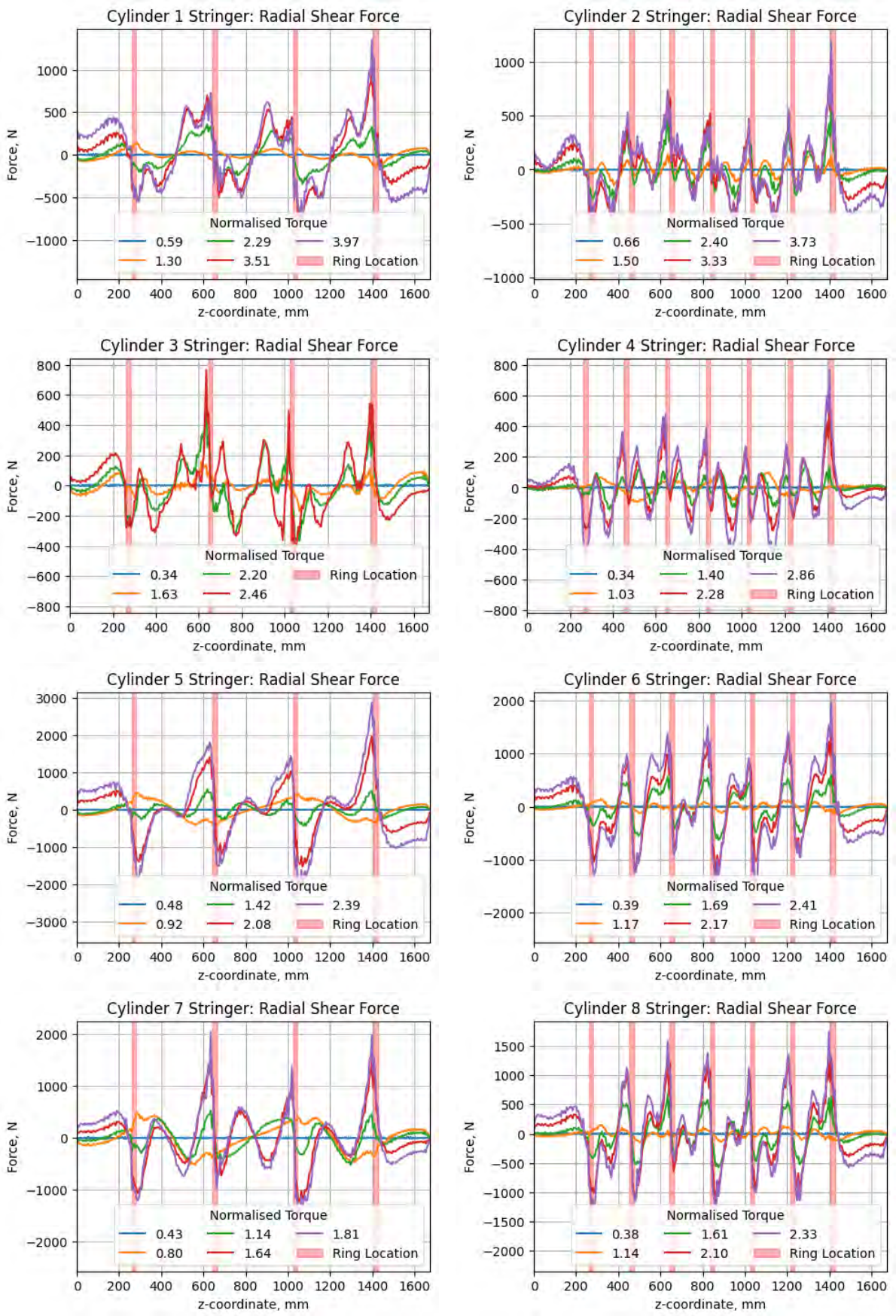

Figure 5.18: Radial shear force in the stringers at different loads for all perfect cylinders

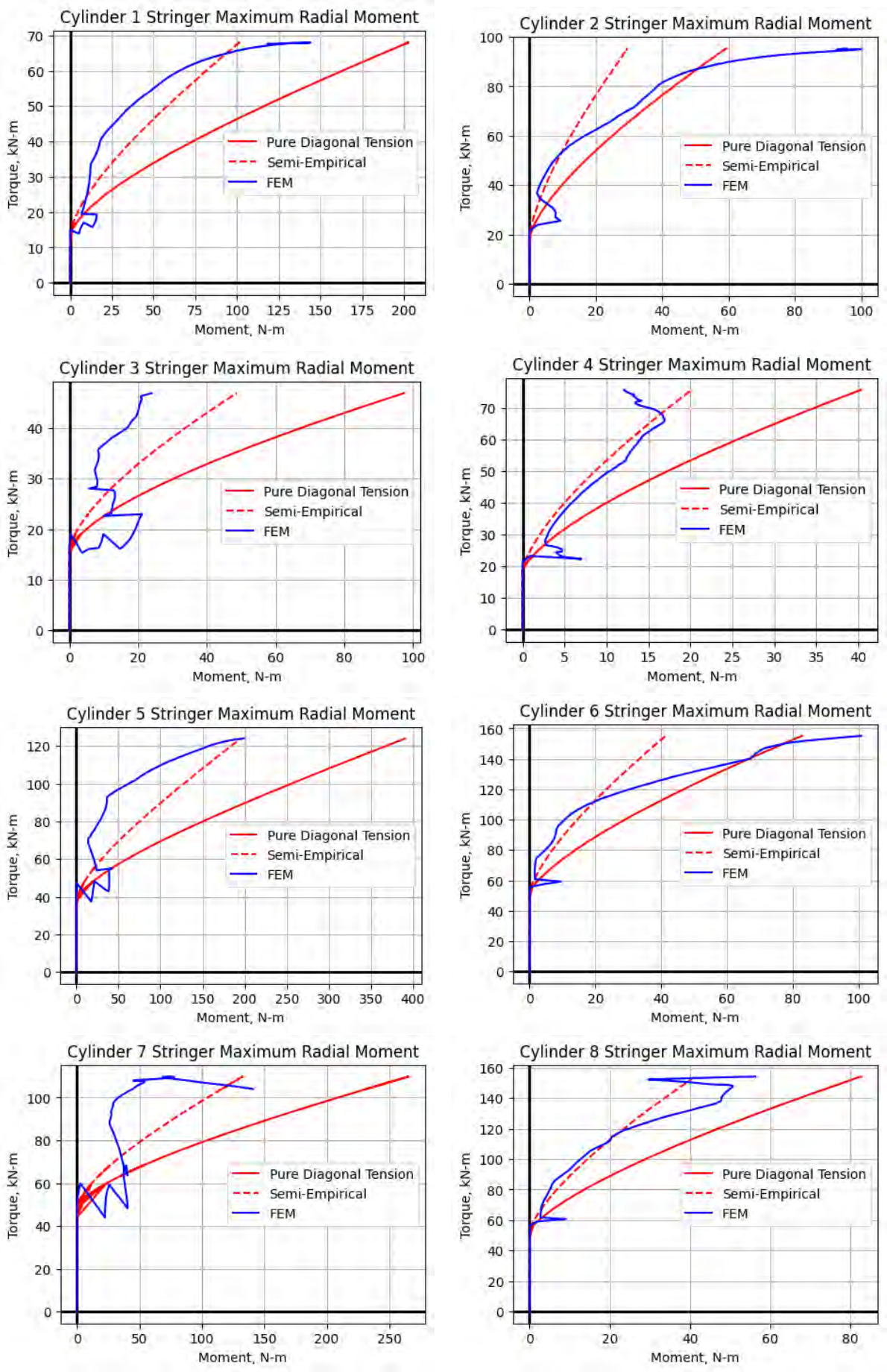

Figure 5.19: Comparison of maximum stringer moment (about the skin mid-plane) along the length calculated from FEM results and the theory of pure diagonal tension

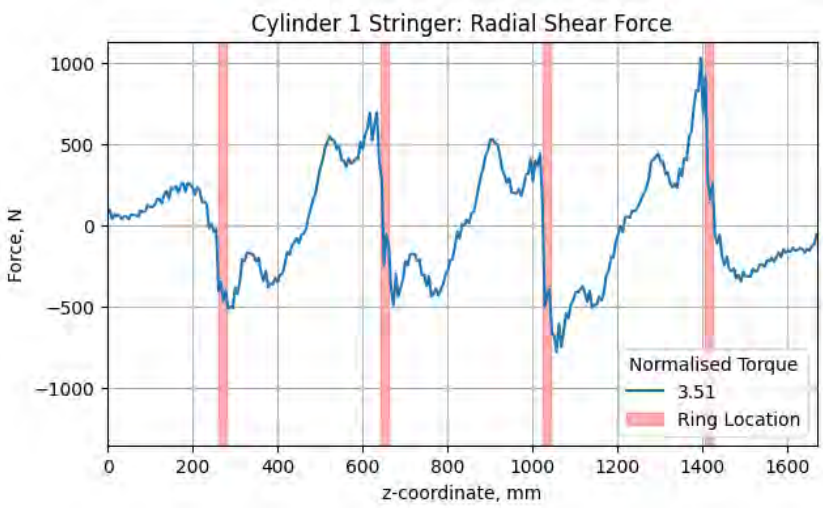

(a) Shear force distribution (R-force)

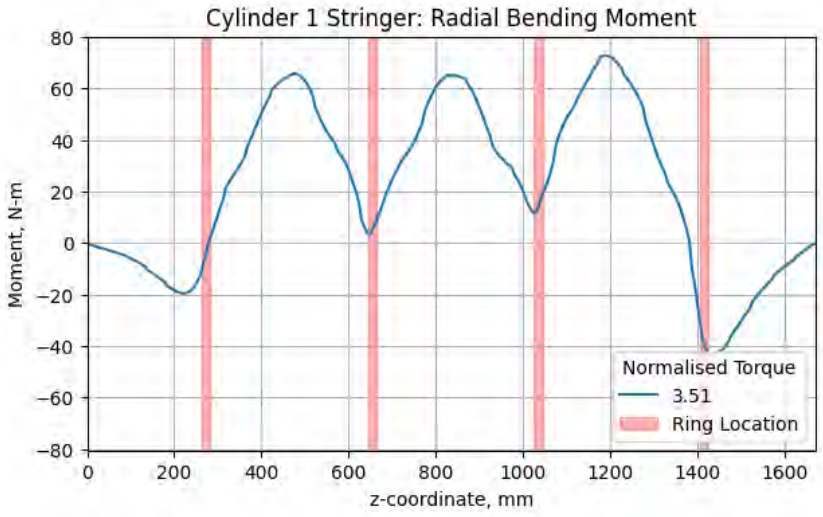

(b) Bending Moment Distribution (Θ-moment)

Figure 5.20: Shear force and bending moment distribution for the radially inwards bending of the stringers in Cylinder-1

peak moments (Equation 2.24). Ideally, the analysis should be done using a typical line load distribution along the length of the stringer where the bays have buckled, however calculating it from the results of the virtual tests was unfeasible and likely, would have been inaccurate as well given the uncertainty present in the established virtual testing model. Moreover, such a load distribution would depend on the post-buckled shape of the skin (in a similar manner to the ”local effect” as discussed for the axial loads), which is difficult to predict without performing a non-linear analysis. However, such an analysis might not even be needed as for practical cases where the stringer is only on one side of the skin, the off-axis introduction of compression loads might affect the moments on the stringers more than the inward pulling of the skin. Perhaps this is why for all the versions of the semi-empirical method found in later literature [26, 33], the secondary bending is not taken into account for failure calculations, both for crippling and Euler buckling of the stringer. Moreover, as the empirical failure models used

in the design methods are fitted to data from experiments where secondary bending would have affected the failure in some minor part, it is likely that the effect gets accounted for due to the data fitting.

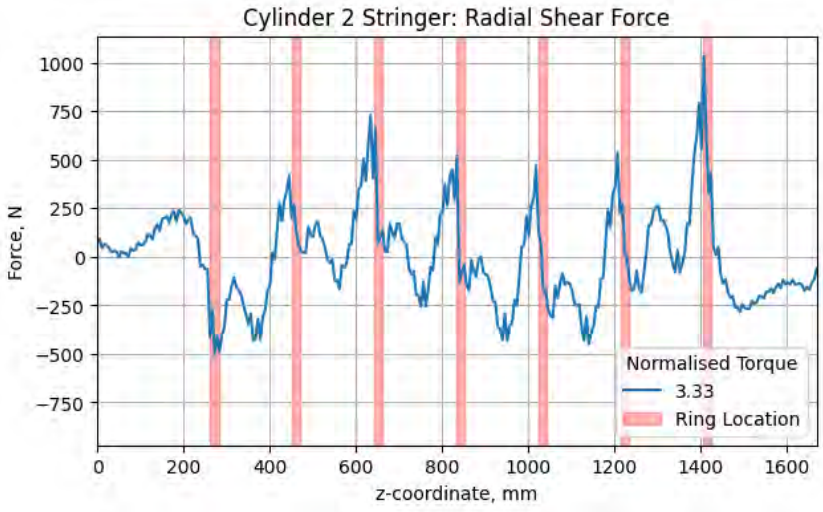

(a) Shear force distribution (R-force)

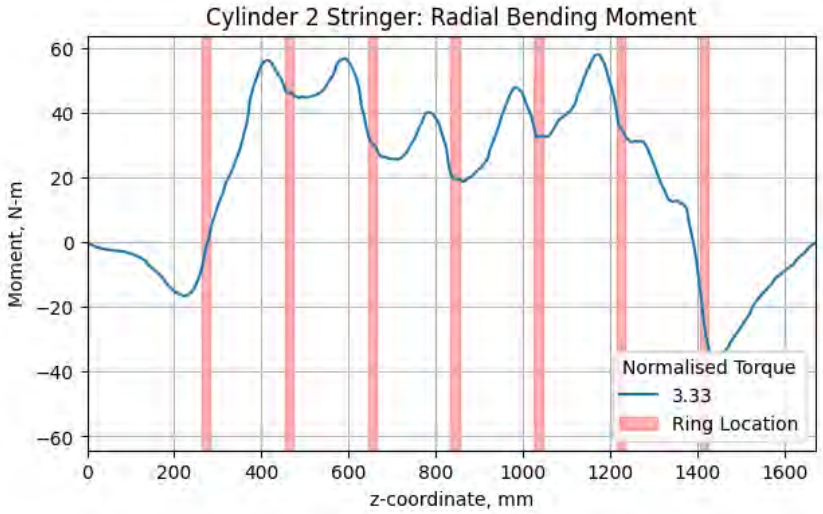

(b) Bending Moment Distribution (Θ-moment)

Figure 5.21: Shear force and bending moment distribution for the radially inwards bending of the stringers in Cylinder-2

5.3.2. Stringer In-Plane Bending

There is another component of the secondary bending load present in the stringers which is the bending in the circumferential direction (also referred to as in-plane bending in the text). The graphs for the bending moment in that direction can be seen in Figure D.1[5]. From the graphs, it can be observed that there is indeed significant bending in the circumferential direction, although lower in magnitude compared to the radial bending. In all figures, there can be seen that there is a significantly higher bending moments present at the first and the last ring, which

[5]Note that the convergence of this distribution is in doubt (see section C.2)

is caused by different deflection of the stringer due to the difference in stiffness between the doubled region and the subsequent bending of the stringers at these locations as shown in Figure 5.22. In fact, this effect is also seen before buckling as seen in Figure 5.22b, which would be even more pronounced after buckling as the shear stiffness of the buckled skin greatly reduces, and a larger fraction of the torsion loads are redistributed to the stringers in the form of in-plane shear loads that create in-plane bending moments.

Furthermore, it can be seen in Figure D.1 that the distribution of the bending moment over every bay is broadly similar, which is easier to observe in the results for 7-ring cylinders, which shows a repeating trend in every bay, which can also be seen in the distribution of the shear force over the length (Figure D.2). Over different cylinders, the trend for bending moment may be categorised into a set containing all the 4-ring cylinders and the 7-ring cylinders, in which the earlier set shows a more monotonous increase in bending moment from the first ring going towards the second which is then sharply reduced to around zero at the ring locations. Whereas, for the 7-ring cylinders, a local minima is perceptible towards the middle of the bay which may be correlated with the higher number of half waves seen in the skin for these cylinders. The trend of in-plane shear forces on the stringers is similar for all cylinders. From the first ring to the next, the shear force decreases and shoots up at the ring locations indicating that there is on average a net force on the stringer in the circumferential direction due to the skin which is counteracted by reaction forces at the ring locations.

The bending moment development could be attributed to the differential in the shear traction at different regions along the length of the stringer as was seen for the axial loads, which would cause a net bending moment in the circumferential direction. The most likely explanation for the net force in the circumferential direction is the difference between the applied shear and normal traction on either side of the skin. This hypothesis was attempted to be checked using the circumferential section force plot in the skin as seen in Figure E.2, however, only a slight difference may be observed in the value on either side of the stringer and it is difficult to say whether there will be net force in any direction. Confirmation of both the hypotheses would require comparing the distribution of shear and normal traction on either side of the stringer, which is not feasible from the current results due to the discrete nature of load transfer through the rivets.

5.3.3. Ring Radial Bending

In the theory by Kuhn et al [1], nothing was mentioned about the secondary bending on the rings except for the case when they are floating. So the present study attempted to characterise and analyse the radially inwards bending of the ring. The bending moment distribution about the centroid of the ring cross section was calculated and plotted in Figure D.3, which however does not coincide with the neutral axis of the ring. In fact, it can be observed that for cylinder 3, the moment at the centroid of the ring cross section is very similar to the axial force distribution (Figure 5.6) indicating significant deviation of the extraction location from the neutral axis. Furthermore, the load case is complicated due to the curved shape of the rings

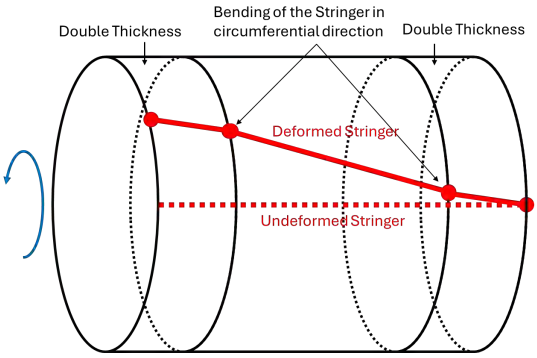

(a) Visualisation of the deformation of the stringer when the cylinder is twisted

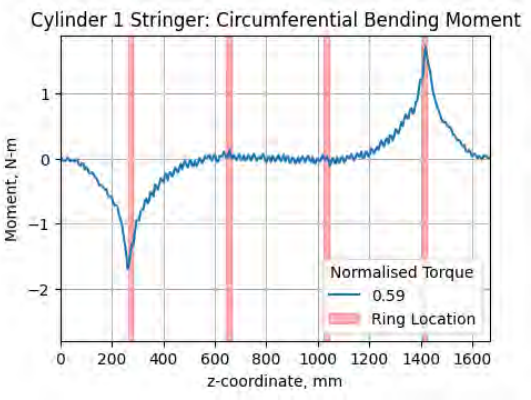

(b) The circumferential (in-plane) bending moment distribution of the stringer before buckling

Figure 5.22: The circumferential (in-plane) bending of the stringer at the location of the change in thickness

and the off-neutral axis load application as the shear flows from the skin to the flange of the ring, due to which the axial force distribution would have significant effect on the bending moment. Moreover, it is also known that for curved beams, the neutral axis and the centroidal axis do not coincide as the material that is radially inwards is stressed more than material that is radially outwards.

Under the above considerations, it was deemed wise to just look at the radial shear force distribution as shown in Figure D.4, where it can again be observed that most of the load is generated after buckling. Here, difference between different cylinders are clearly visible as all 4-ring cylinders show saw-tooth-like behaviour about the x-axis with a consistently monotonous decrease in shear force in each bay. On the other hand for the cylinders with 7 rings, while an overall decrease in shear force is noted over the bay, the trend is not monotonous with strong increases in shear force noted in certain regions, which again correlates with the multiple half waves on the 7-ring cylinders. This is an indication that the inwards force depends on the deformation pattern of the adjacent skin panels, where the regions of increase and decrease in the shear force correlate with different half waves. Furthermore, looking at the distribution of the section force in the axial direction of the cylinder (Figure E.1) which is responsible for the pulling of the ring in the axial direction, it can be seen that there are regions of slight compression along the rings (especially prominent for cylinder 4 where substantial greenish blue regions may be seen adjoining the rings). It is reasoned that this compression causes the increase in the radial shear force because instead of the skin pulling the ring in, at these locations the rings are pushed out.

5.3.4. Ring In-Plane Bending

The in-plane bending of the rings were again never previously studied in detail. With the present methodology, the bending moment that causes the ring to bend in the plane of the skin could be measured at the centroid of the ring cross section, as shown in Figure D.5. Again, the distributions could be divided into two sets, the first one being the 4-ring cylinders,

where the bending moment is relatively uniform over the width of the bay, whereas in the other case, the bending moment peaks near the first stringer location. This categorisation can also be observed in the shear force distribution (Figure D.6) where for the earlier set of cylinders, there is a broadly monotonous decline in shear force in contrast to the more varying distribution for the 7-ring cylinders. Yet again, this behaviour correlates with the different types of half waves adjoining the ring for the 7-ring cylinders compared to the 4-ring cylinders, which cause the net load to oscillate to either side of the ring (thus the non-monotonous change in shear force). This is again observable in the distribution of axial shear forces (Figure E.1) where it can be seen that for all the cylinders, the distribution is different along the length of the ring on either side of it.

5.3.5. Remarks

In this section, the secondary loads, which are transverse to the axis of the stiffeners were characterised. It was found that the exact distribution of the loads depend on the post-buckled deformation pattern of the skin. In all the bending moments discussed, the radial bending stands out as it shows both local variation and a strong global variation of the loads in a vein similar to the axial loads, the earlier being caused by the local deformation of the skin and the latter being caused by the deformation pattern of the whole cylinder across various bays. In this context, the specified design values for bending moment were deemed unwise for the use in design as the bending moment at a point is not accurately represented using the beam fixed on both ends with distributed load assumption made by Kuhn et al [1].

For the in-plane bending loads in the stringers (circumferential bending), a consistent trend was observed locally in each bay, which was superimposed on the bending effect caused by the transition of the stringer from the double thickness region to the single thickness region. For the ring secondary bending, it was too difficult to analyse the radial bending moment due to the difficult-to-find neutral axis and a multitude of loads causing any bending moment like the off-axis introduction axial loads. The shear force was analysed and very similar trends were found in each bay, correlating to the skin deformation patterns. Furthermore, looking into the in-plane bending of the ring, similar correlation could be seen. The common thread being non-monotonous increase/decrease in shear force being found for 7-ring cylinders which have multiple half waves in their post-buckled skin deformation pattern.

For all cases, thought was given on the possible load transfer mechanism. For the shear loads in the radial direction, the general explanation of the flattening of the skin pulling the stiffeners inwards largely explains the overall bending, however, no detailed correlation could be established with the deformation pattern. For the in-plane loads, the bending moment distribution could be correlated with the uneven shear flow introduction into the stiffener on either side. For the shear force, it was hypothesised that the apparent net force on them was due to the difference in net normal traction provided by the skin on each side. However, further information is needed than extracted in the present study, mainly the shear and normal traction distribution on each side of the stiffeners. However, the outputs generated from virtual

testing were not refined enough to establish a detailed understanding of the load transfer mechanism. First, the uncertainties of the virtual testing model that arise from the under-reported experimental data cast a doubt on the quantitative values calculated. Second, the mesh is not converged for the in-plane shear forces. Finally, even in the case of converged values, the presence of rivets make the load transfer discrete, making the correlation of the continuous distribution of the skin section forces. With these considerations, perhaps a better analysis could be performed using a more validated approach and using a bonded model to capture the ideal case of continuous load transfer at the interfaces to validate the model.

6

Conclusion

This thesis set out to develop a virtual testing approach for post-buckled cylindrically curved skin-stiffened structures using FEM and to analyse the load transfer mechanism. After a thorough literature review, the following research question was posed: *"How to develop and validate a virtual testing model for curved diagonal tension cylinders and accurately analyse the loads generated on the stiffeners?"*. Four sub-questions were posed to help answer this question with corresponding hypotheses. To answer these questions, a virtual testing approach was developed in this project and compared to experiments for the validation, which was then used to analyse the loads on the stiffeners. In this section, a summary of the results and findings are presented. The research questions can now be revisited and answered.

1. What details are needed to be modelled to accurately recreate experimental results?
2. How to account for the unknown geometrical imperfections in the experiments?
3. To what extent can the model be validated given the under-reported experimental data and how useful would that model be?
4. What is the load transfer mechanism according to the results of virtual testing and how well do the analytical models take this into account?

6.1. Answers to the Sub-Questions

The first two sub-questions were *"What details are needed to be modelled to accurately recreate experimental results?"* and *"To what extent can the model be validated and how useful would that model be?"*. The hypothesis to answer the earlier was that *"modelling the geometry, material and boundary conditions with accuracy is needed to recreate the stress response and in addition, an imperfection model will be needed to recreate the gradual appearance of the diagonal folds"*. The two research questions may be answered at the same time. In

the model generated, the stress response in the stringers and rings were compared with the experimental results. In all cases, the trend of the stresses matched well with experimental data and the addition of imperfections did indeed show a gradual development of diagonal tension stresses. However, the magnitude was off in multiple cases. Many possible reasons were discussed for the discrepancy and categorised into two main categories, the inaccurate modelling of known parameters and the uncertain parameters from the experiment. It was reasoned out that the main reason for the discrepancy is the unknown imperfection in the skin and a possible resistance to the axial contraction of the cylinder provided by the testing jig. So, while the hypothesis cannot be said to be proven given the uncertainty about the experimental results, it can be said to be plausible. Furthermore, given that the virtual testing results lie in the range of possibilities caused by the uncertainty in the experimental data, the model could be considered validated enough to provides reasonable modelling of physical behaviour of the tests. As to how useful such a model was, as it was seen in chapter 5, while the exact quantitative observations may not be relied on, the insights on the load transfer mechanisms can be used to develop further knowledge on the topic.

The next sub-question was *"How to account for the unknown geometrical imperfections in the experiments?"* and in this thesis, a large imperfection in the shape of the superposition of first positive and negative eigenmodes were introduced into the model. The aim was just to account for the imperfection by checking the effect of the magnitude. It was hypothesised that *"during post buckling, there will be a slight imperfection sensitivity for the stresses on the stiffeners, which will not affect the stresses too much, especially for deep post buckling"*. However, significant effect of imperfection was found on the stresses in some cases, which goes to disprove the hypothesis. Furthermore, the eigenmodes used had different deformation patterns in different bays which resulted in different stringers having different stresses, which indicated that there is significant effect of the imperfection shape on the stresses. This result warrants a further study that should analyse systematically the effect of imperfections.

The final sub-question pertains to the use of the developed model to analyse the loads that develop in the stringers and it asked *"What is the load transfer mechanism according to the results of virtual testing and how well do the analytical models take this into account?"*. To this end, a post-processing method was developed that could calculate the shear force and bending moment distribution in the stiffeners. Using this, the primary axial loads and the secondary bending loads were analysed. Two hypotheses were made with regards to the local distribution of the loads and their agreement with the current semi-empirical analysis method. They were that *"the local distribution of the axial load depends upon the post-buckling deformation pattern of the adjacent panels"* and that *"the local distribution of the loads is not captured well in the analytical method."* The local distribution of the loads, especially in the stringers were found to be in complete opposition to the assumption of a compression maximum at the middle of the bays. Instead the peak was always at the ring location with a minimum in the middle of the bay or the bay showing monotonous increase/decrease in stresses, thus proving the latter hypothesis. Further analysis of the results and correlation with the deformation pattern found

that the distribution of axial loads were correlated with the deformation pattern in the adjoining bays, thus proving the earlier hypothesis.

Further analysis was done to reason out the ”cause” of the local variation in stresses and it was found that the change in effective width along the length argument, which was taken from results from flat webs were flawed as a very similar variation in the axial load was found if the cylinder was axially restrained. Further comparison with the shear stress and principal stress distribution on the skin showed that along regions of high inwards skin deformation, the shear stress is low. It was observed that the shear flow into the stiffener is high when one side of the stiffener attaches to a skin under less deformation where the shear stress is high compared to the other side where the shear stress is low due to high skin deformation. The developed understanding of the load transfer mechanism categorised the effect of diagonal tension into its global and local effect, where the global effect refers to the pulling force created by the diagonal tension field and the local effect refers to the shear flow transfer into the adjoining stiffeners causing the local variation. Finally, a comparison was made between the virtual testing loads and the semi-empirical method, which showed the semi-empirical method deviate significantly from the results as it uses the incorrect assumption of maximum compressive stresses at the centre of the bay.

Similarly to the axial loads, the secondary bending effects were characterised using the developed post-processing approach for the two stringers in the radial direction and along the plane of the skin. For all cases, the shear force distribution was judged to depend on the deformation pattern of the skin. The results for the radial bending of the stringers were interesting as in addition to the local inward bending expected to be observed within every bay, there was an overarching trend observed across bays, which led to the conclusion that the specified design value for moment is a flawed approach to analyse secondary bending. Further, an attempt was made to find the load transfer mechanism for which the inward pulling of the stiffeners by the ”flattening” of the skin explains the observation of the radially inwards bending, no detailed correlation could be developed like in the case of axial forces. For the in-plane bending, the bending moment and the net shear force seen in a bay were hypothesised to arise from the differential in the shear and normal traction on either side of the stiffener respectively, however, the hypothesis could not be checked as it requires a more refined model.

6.2. Concluding Remarks

In conclusion, in this thesis, a virtual testing framework was developed with the aim to analyse the load transfer mechanism in diagonal tension panel. By modelling the geometry, material, boundary conditions, and imperfections, the experimental trends were recreated. It was also seen that for diagonal tension in curved skins, the imperfection affects the results not only for the buckling load but for the post buckling stresses as well. While the exact experimental results could not be recreated due to the uncertainties, with accurate modelling of known parameters, and sensitivity studies into the uncertainties permitted enough confidence in the model to use it for analysis of the load transfer mechanism. The developed post-processing

approach allowed a detailed characterisation of the loads on the stiffeners that would be difficult to measure in actual experiments. Further analysis of the distributions enabled a more detailed understanding of the load transfer mechanism for axial loads generated on the stiffeners which differ from the traditional understanding.

6.3. Recommendations for future work

The results of this thesis opens up scope for future work in the further development of the framework and on further analysis of diagonal tension, which are discussed below.

Through the validation effort for the virtual testing approach, this study showed the importance of extensive documentation and reporting of experimental data. The The set of tests selected to validate the models had limited reported experimental data which limited the confidence on the developed framework. So, to further gain confidence in it, the framework could be used to create other similar cylinders that have more data reported from the experiments. For example, the four other cylinders tested by Kuhn et al [6] could be used for further validation with relatively minor changes in the stringer geometry and extraction procedure. Furthermore, there are other NACA tests with slightly different geometry [38, 29] about cylinders under torsion with slightly different geometry, but with more reported outputs such as the torque-twist curves and even detailed observations of deformation pattern on the skin (which is crucial to the loads that develop on the stiffeners as seen in chapter 5).

While this study was focused just on the loads, the models generated were able to exhibit crippling type of failure. The current model may be further developed to include material damage models and further refinement to recreate both the skin and the stiffener failure that was observed in the experiments [6].

From the imperfection study conducted, it is evident that both the magnitude and the shape of the imperfection is critical to the stress response on the stiffeners, which warrants further studies into systematic effects of imperfection on diagonal tension behaviour. This study used just the first eigenmodes as imperfections, however, it would be interesting to see how higher modes and their combinations affect the stresses. Furthermore, future experimental investigations into diagonal tension should make effort to capture the exact imperfection field so that validation of finite element models is easier.

For the analysis of the load transfer mechanism, the biggest shortcoming in this thesis was the unconverged results for the in-plane shear force. The assumption of converged axial stress outputs resulting in converged shear forces was not sound. Thus, in future studies, detailed convergence studies should be made on the variables used for subsequent analysis that may be different than those on which the model was validated.

The developed understanding of the global and local effects of diagonal tension offers a basis for studies into post buckling of curved panels loaded in both compression and shear. The theory developed for this case by Kuhn et al [1] heavily relies on the effective width concept

for both compression and shear. While for compression effective width may seem logical, for shear and diagonal tension, as seen in this study, it does not agree with the load transfer mechanism. It will be interesting to study what happens as more and more compression is introduced in the stringers. The developed understanding of the local effect being rather independent of the average load on the stringers caused by the global effect and external load would be challenged. Perhaps there is a turning point after addition of enough compression that the load transfer may be better explained with the effective width concept. In fact, the current framework could be used with minor modifications on the boundary conditions and the removal of the outer stringer to recreate the experiments run by Kuhn et al [6] for stiffened cylinders under torsion and compression to explore this area.

References

[1] P Kuhn, JP Peterson, and LR Levin. “A summary of diagonal tension Part I: methods of analysis”. In: (1952). URL: https://ntrs.nasa.gov/citations/19930083335.

[2] Saullo G.P. Castro et al. “Evaluation of non-linear buckling loads of geometrically imperfect composite cylinders and cones with the Ritz method”. In: *Composite Structures* 122 (Apr. 2015), pp. 284–299. ISSN: 0263-8223. DOI: 10.1016/J.COMPSTRUCT.2014.11.050.

[3] Saullo G.P. Castro et al. “Linear buckling predictions of unstiffened laminated composite cylinders and cones under various loading and boundary conditions using semi-analytical models”. In: *Composite Structures* 118.1 (Dec. 2014), pp. 303–315. ISSN: 0263-8223. DOI: 10.1016/J.COMPSTRUCT.2014.07.037.

[4] R Vescovini and C Bisagni. “Two-step procedure for fast post-buckling analysis of composite stiffened panels”. English. In: *Computers and Structures* 128 (2013), pp. 38–47. ISSN: 00457949 (ISSN). DOI: 10.1016/j.compstruc.2013.06.002. URL: https://www.scopus.com/inward/record.uri?eid=2-s2.0-84884253384&doi=10.1016%2fj.compstruc.2013.06.002&partnerID=40&md5=c3a419713dac049b33dd7e3964087214.

[5] Saullo G.P. Castro and Maurício V. Donadon. “Assembly of semi-analytical models to address linear buckling and vibration of stiffened composite panels with debonding defect”. In: *Composite Structures* 160 (Jan. 2017), pp. 232–247. ISSN: 0263-8223. DOI: 10.1016/J.COMPSTRUCT.2016.10.026.

[6] P Kuhn, JP Peterson, and LR Levin. “A summary of diagonal tension Part II: experimental evidence”. In: (1952). URL: https://ntrs.nasa.gov/citations/19930083352.

[7] SP Timoshenko and JM Gere. *Theory of elastic stability*. 2009. URL: https://books.google.com/books?hl=en&lr=&id=rAk_AwAAQBAJ&oi=fnd&pg=PP1&dq=timoshenko+theory+of+elastic+stability&ots=4OvN_BTlVL&sig=DFgKLCfTXrOunhCE_SjMxBmNROI.

[8] S. C. Redshaw. “The Elastic Stability of a Curved Plate Under Axial Thrusts”. In: *The Journal of the Royal Aeronautical Society* 42.330 (June 1938), pp. 536–553. ISSN: 0368-3931. DOI: 10.1017/S0368393100103256. URL: https://www.cambridge.org/core/product/identifier/S0368393100103256/type/journal_article.

[9] SB Batdorf, M Schildcrout, and M Stein. *Critical combinations of shear and longitudinal direct stress for long plates with transverse curvature*. Tech. rep. 1947. URL: https://ntrs.nasa.gov/api/citations/19930081973/downloads/19930081973.pdf.

[10] Murry Schildcrout and Manuel Stein. *Critical combinations of shear and direct axial stress for curved rectangular panels*. Tech. rep. 1949. URL: https://ntrs.nasa.gov/citations/19930082606.

[11] E F Bruhn. *ANALYSIS AND DESIGN OF FLIGHT VEHICLE STRUCTURES*. Tech. rep. 1973.

[12] DJ Wilkins. "Anisotropic Curved Panel Analysis". In: *General Dynamics, Convair Aerospace Division Report FZM-5567* (1973). URL: https://apps.dtic.mil/sti/citations/ADA309250.

[13] VZ Vlasov. "General theory of shells and its application in engineering". In: *cir.nii.ac.jp* (1964). URL: https://cir.nii.ac.jp/crid/1570572699245590912.

[14] D. M. A. Leggett. "The elastic stability of a long and slightly bent rectangular plate under uniform shear". In: *Proceedings of the Royal Society of London. Series A - Mathematical and Physical Sciences* 162.908 (Sept. 1937), pp. 62–83. ISSN: 0080-4630. DOI: 10.1098/RSPA.1937.0167.

[15] A Krornm. *The limit of stability of a curved plate strip under shear and axial stresses*. Tech. rep. 1939. URL: https://ntrs.nasa.gov/citations/19930094518.

[16] S.B. Batdorf, Murry Schildcrout, and Manuel Stein. *Critical shear stress of long plates with transverse curvature*. Tech. rep. 1947. URL: https://ntrs.nasa.gov/api/citations/19930081971/downloads/19930081971.pdf.

[17] SB Batdorf, M Stein, and M Schildcrout. *Critical shear stress of curved rectangular panels*. Tech. rep. 1947. URL: https://ntrs.nasa.gov/api/citations/19930081975/downloads/19930081975.pdf.

[18] S B Batdorf, Manuel Slein, and Murry Schildcrout. *Critical stress of thin-walled cylinders in torsion*. Tech. rep. 1947. URL: https://ntrs.nasa.gov/api/citations/19930081969/downloads/19930081969.pdf.

[19] Mozhdeh Amani, B. L.O. Edlund, and M. M. Alinia. "Buckling and postbuckling behavior of unstiffened slender curved plates under uniform shear". In: *Thin-Walled Structures* 49.8 (Aug. 2011), pp. 1017–1031. ISSN: 0263-8231. DOI: 10.1016/J.TWS.2011.03.007.

[20] EE Sechler and LG Dunn. *Airplane structural analysis and design*. 1942. URL: https://cir.nii.ac.jp/crid/1130282272347168896.

[21] C Kassapoglou. *Design and analysis of composite structures: with applications to aerospace structures*. 2013. URL: https://books.google.com/books?hl=en&lr=&id=hMejr4aIehQC&oi=fnd&pg=PP7&dq=design+and+analysis+of+composite+structures+kassapoglou&ots=iI1MSe1lZ-&sig=NOlwBCYT3IxqZDeoTte_3Qjsh_E.

[22] Theodor Von Karman et al. "The Strength of Thin Plates in Compression". In: *Journal of Fluids Engineering* 54.2 (Jan. 1932), pp. 53–56. ISSN: 0098-2202. DOI: 10.1115/1.4021738. URL: https://dx.doi.org/10.1115/1.4021738.

[23] Karl Marguerre. *The apparent width of the plate in compression*. Tech. rep. 3. 1937. URL: https://ntrs.nasa.gov/api/citations/19930094583/downloads/19930094583.pdf.

[24] DEPARTMENT OF THE AIR FORCE WASHINGTON. *Strength of Metal Aircraft Elements Revised Edition, June 1951*. Tech. rep. 1951. URL: https://apps.dtic.mil/sti/citations/ADA382434.

[25] RB Deo, BL Agarwal, and E Madenci. *Design Methodology and Life Analysis of Postbuckled Metal and Composite Panels: Volume 1*. Tech. rep. 1985. URL: https://apps.dtic.mil/sti/citations/ADA171253.

[26] R B Deo and B L Agarwal. "Design Methodology and Life Analysis of Postbuckled Metal and Composite Panels. Volume 3. Design Guide". In: (1985). URL: https://apps.dtic.mil/sti/citations/ADA170988.

[27] H Wagner. *Tension fields in originally curved, thin sheets during shearing stresses*. Tech. rep. 1935. URL: https://books.google.com/books?hl=en&lr=&id=tI1TAAAAMAAJ&oi=fnd&dq=Wagner,+H.,+and+Ba+l+lerstedt,+W.:+Tension+Fie+l+ds+in+Originally+Curved,++Thin+Sheets+dur+ing+Shearing+Stresses&ots=6eUIM-G_wh&sig=Z5ESSdXZSGVcQDuvKnsDMlcVjB8.

[28] P Kuhn and GE Griffith. *Diagonal Tension in Curved Webs*. Tech. rep. 1947. URL: https://books.google.com/books?hl=en&lr=&id=C3xDAQAAIAAJ&oi=fnd&pg=PA26&dq=Diagonal+Tension+in+Curved+Webs+kuhn&ots=46m2MvzFFz&sig=7gACBmiTCoHwwagTjqIx9BUkZ1o.

[29] R L Moore and C Wescoat. *Torsion Tests of Stiffened Circular Cylinders*. Tech. rep. 1944. URL: https://ntrs.nasa.gov/citations/19930090929.

[30] R B Deo, H P Kan, and Northrop Corporation. "Design Development and Durability Validation of Postbuckled Composite and Metal Panels. Volume 1. Executive Summary". In: (1989). URL: https://apps.dtic.mil/sti/citations/ADA250299.

[31] R B Deo et al. "Design Development and Durability Validation of Postbuckled Composite and Metal Panels, Volume II- Test Results". In: (1989). URL: https://apps.dtic.mil/sti/citations/ADA250565.

[32] R B Deo, H P Kan, and " N M Bhatia. "Design Development and Durability Validation of Postbuckled Composite and Metal Panels. Volume 3. Analysis and Test Results". In: (1989). URL: https://apps.dtic.mil/sti/citations/tr/ADA251104.

[33] R B Deo, H P Kan Dtic, and J A Hangen. "Design Development and Durability Validation of Postbuckled Composite and Metal Panels, Volume IV Design Guide Update". In: (1989). URL: https://apps.dtic.mil/sti/citations/ADA250661.

[34] James P Peterson. "Experimental investigation of stiffened circular cylinders subjected to combined torsion and compression". In: (1950). URL: https://ntrs.nasa.gov/api/citations/19930082837/downloads/19930082837.pdf.

[35] *Abaqus - SIMULIA User Assistance 2022*. URL: https://help.3ds.com/2022/english/dssimulia_established/SIMULIA_Established_FrontmatterMap/sim-r-DSDocAbaqus.htm?contextscope=all&id=ec01bc8c83d743a6a30123c5a034edca.

[36] By Paul Kuhn, L L Ross Levin Langley Memorial Aeronautical, and boratory Langley Field. *Tests of 10-inch 24S-T aluminum-alloy shear panels with 1-1/2-inch holes I*. 1943.

[37] Paul Kuhn and James P Peterson. *Strength analysis of stiffened beam webs*. 1947.

[38] E Schapitz. *The Twisting of Thin-walled, Stiffened Circular Cylinders*. Tech. rep. 1938.

A

Stress Extraction Location Nomenclature

For the extraction location for stress on the stringer and rings, nomenclature is used which is of the form "$loc = x.y$". For the stringers, x is the number of bays from the ring closest to the fixed end and y is the fraction of the length of the bay at which the extraction location is placed (see Figure A.1. Similarly, for the rings, x has the same meaning, however, the bay 0 is clockwise from the stringer that lies on the global x-axis as seen in Figure A.2. Similarly, y means the fraction of the way through the angle subtended by the bay at the cylinder centre.

The extraction location used for the extraction of stringer stresses for validation are as follows:

- 4-ring cylinders: 1.2, 1.5, 1.8
- 7-ring cylinders: 2.2, 2.5, 2.8, 3.2, 3.5, 3.8

The extraction locations used in the rings are 0.5, 1.5 and 2.5 for all the validation plots.

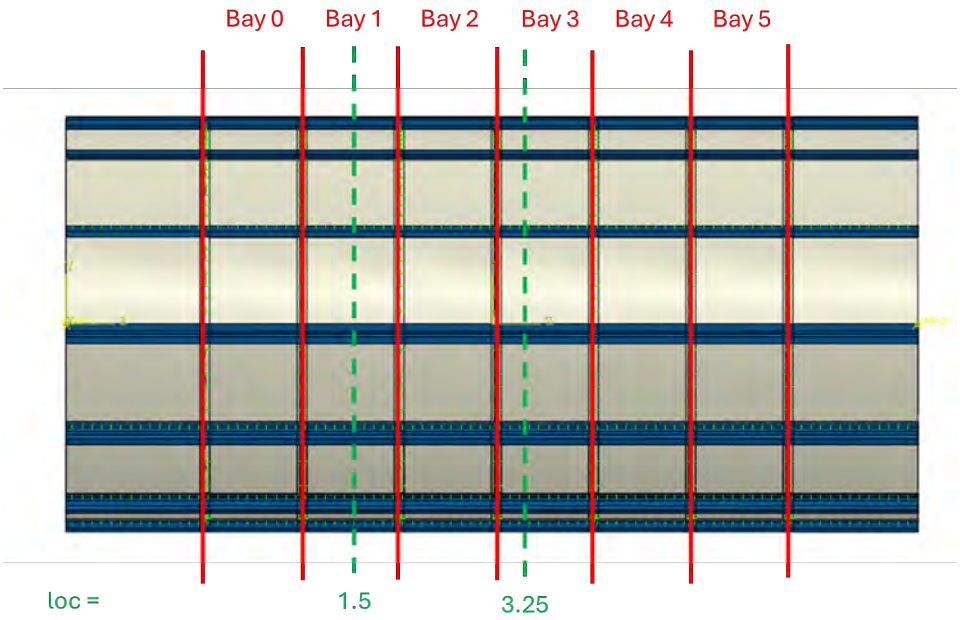

Figure A.1: Nomenclature for the extraction of stringer stresses

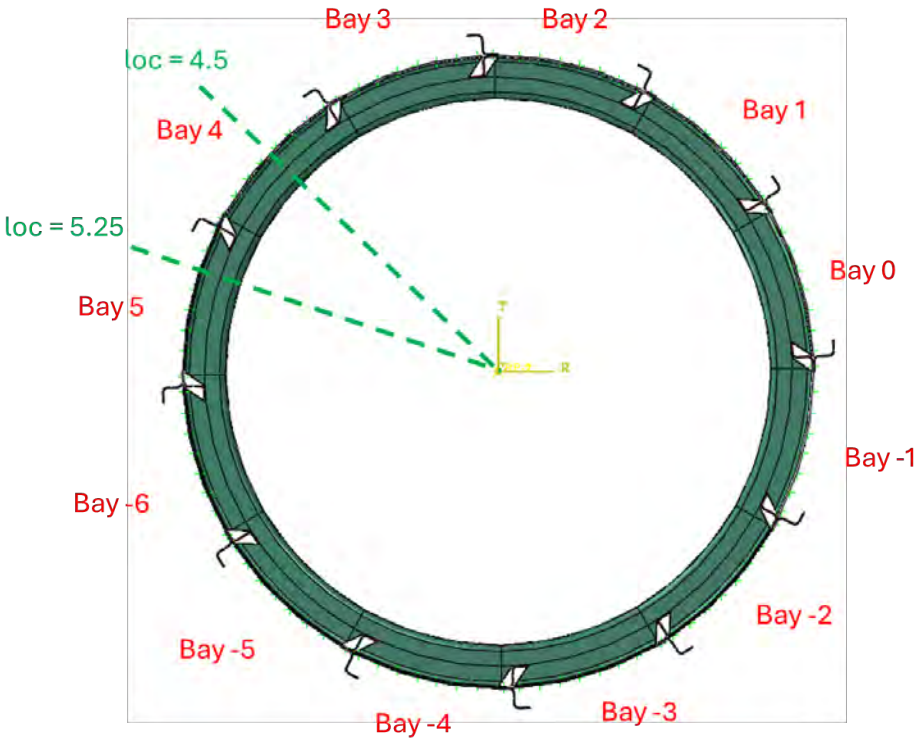

Figure A.2: Nomenclature for extraction location of ring stresses

B

Selection of Modelling Parameters

The results for the earlier presented non-linear analysis was from an analysis that had the best combination of modelling parameters. In the modelling approach presented in section 3.2, there were some parameters that were not completely decided on. These were the method of modelling the doubler region, the method of modelling the skin-stiffener interface and the boundary condition at the loaded end of the cylinder. In this section, the effect of these modelling parameters are discussed and the reason for the selection of the modelling parameters used in all further analyses is established.

B.0.1. Effect of modelling the doubler using the skin feature

The doublers modelled using the skin feature and by extruding the thickness of the skin on the doubled bays result in almost identical behaviour in both the torque vs twist response (see Figure B.1) and the stress response of the stiffeners (see Figure B.2 and Figure B.3). The model using the extruded stringers seem slightly more compliant, and also the rings seem to be loaded to slightly higher stresses. However, for the purposes of the virtual testing model, in the presence of other more important uncertainties, these responses are practically the same.

Using the skin feature does not add any more nodes as it uses the surface nodes of the continuum shell elements and thus is computationally less expensive. Furthermore, using the skin feature models the doubler sheet to be continuous along the circumference of the cylinder. Thus, it was decided to model the doubler using the skin feature for all cylinders.

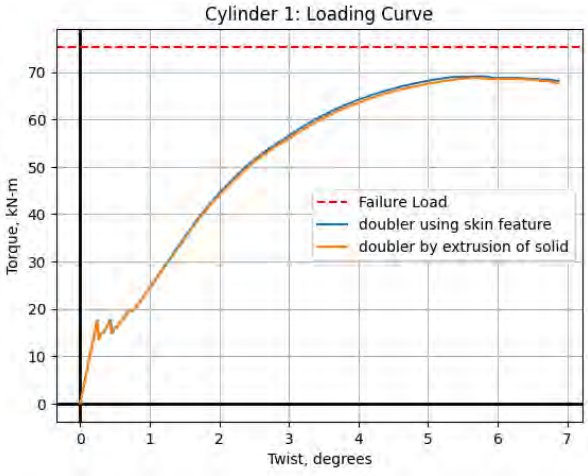

Figure B.1: Loading curves for the two different methods of modelling the doublers

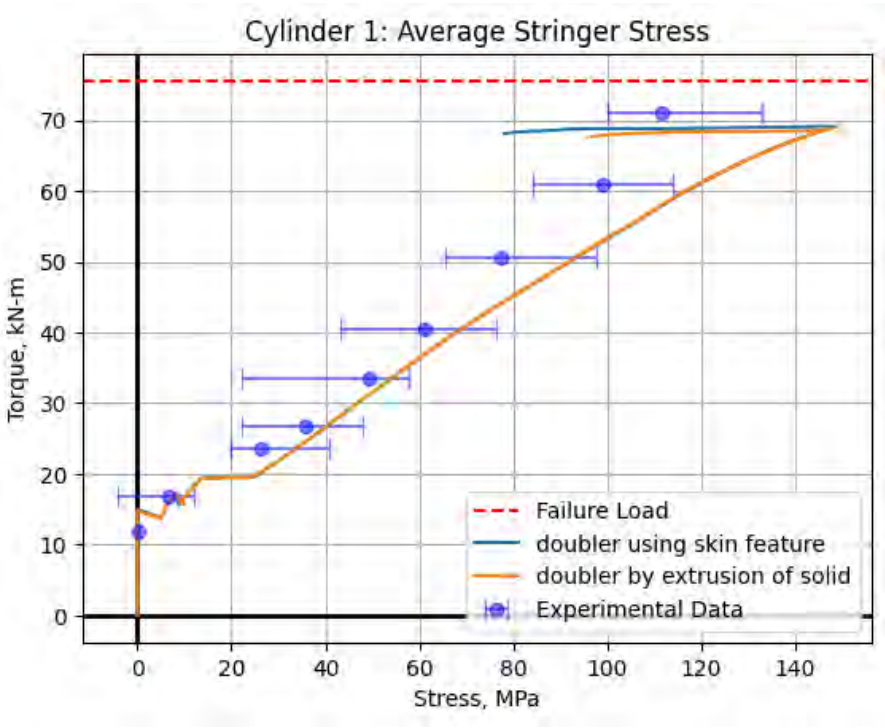

Figure B.2: Stringer Stresses for the two different methods of modelling the doublers

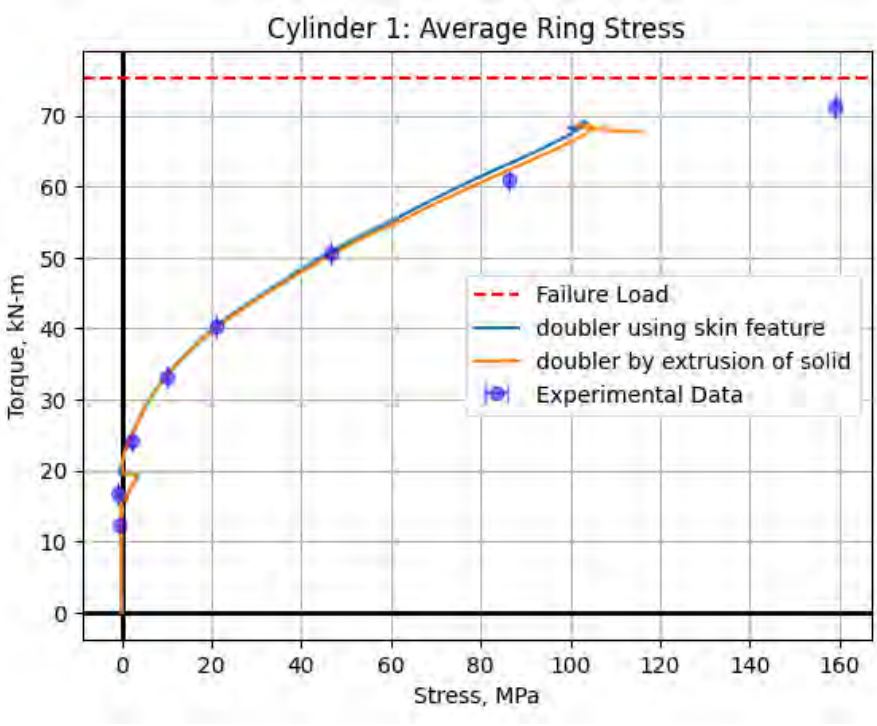

Figure B.3: Ring Stresses for the two different methods of modelling the doublers

B.0.2. Effect of Modelling Rivets

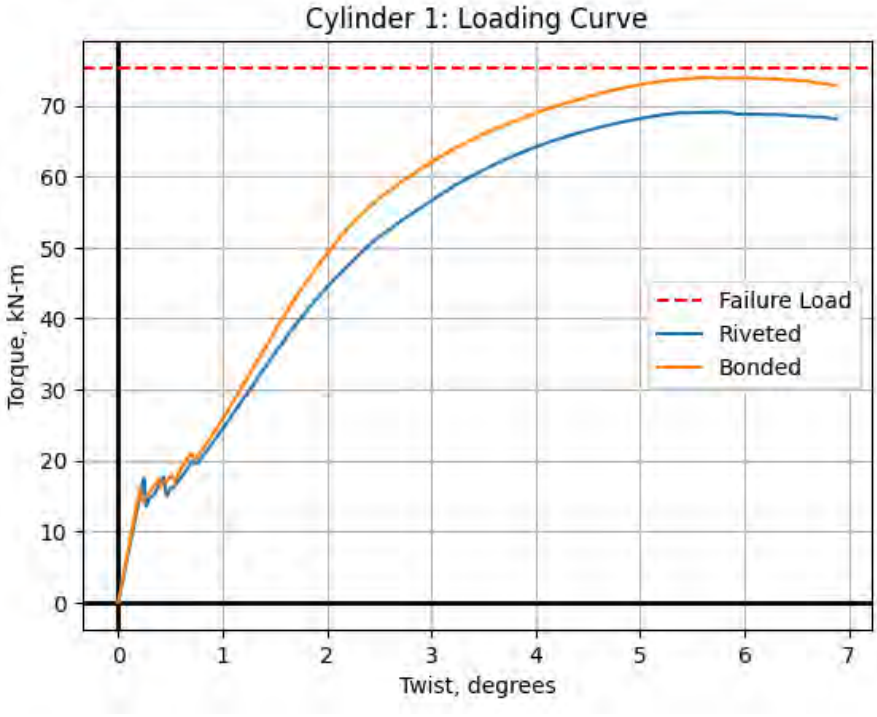

Figure B.4: Loading curves for riveted and tie constrained model

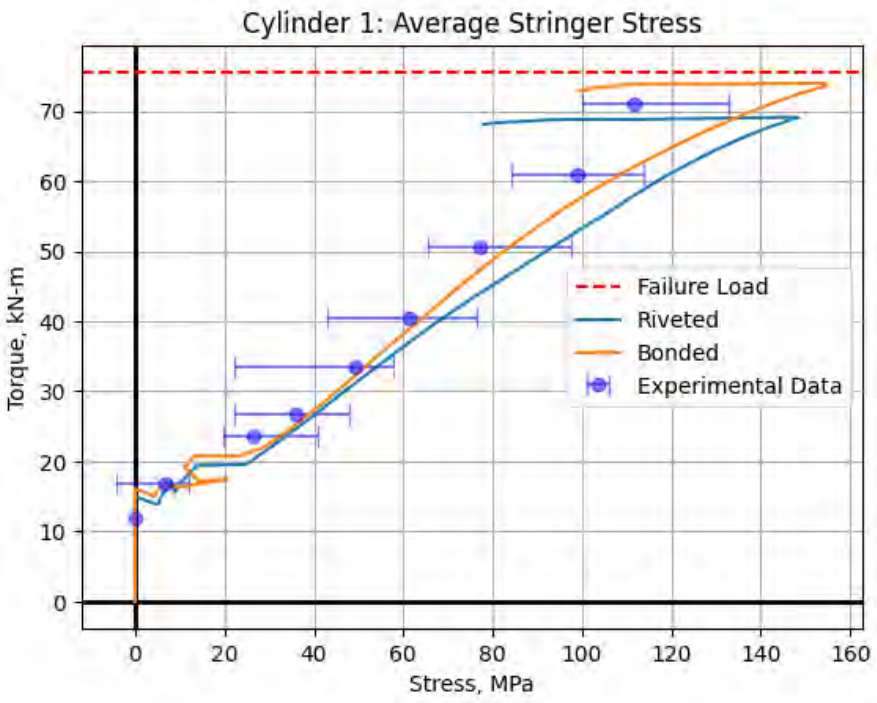

Figure B.5: Comparison of stringer stresses for the riveted and bonded models

The loading curve comparing the torque response for the cylinders where the joint between the stringer and the skin is modelled using point based fasteners (also referred to as riveted model) and tie constraints (also referred to as bonded models) in Figure B.4. The It is clearly apparent that the stiffness of the bonded model is higher than the stiffness of the riveted model during both the linear and post-buckled regimes. This behaviour is expected because using tie constraints, the stiffness of the joint between the skin and the stiffeners is higher. Also, the boundary conditions for each skin bay is less stiff in the riveted model as there is some degree of movement allowed in the skin that is in contact with the stiffeners' bottom flanges. From the same explanation, a smaller buckling load was expected for the riveted cylinder, but the results show slightly higher buckling load for them. This likely arises from the maximum time-step increment not being converged and causing the buckling load to be overshot. It was attempted to converge the time step increment, but even reducing it from 0.01 to 0.0025, it was not possible to capture the buckling load. Further refinement was not attempted as the execution time of the simulation became too large.

The development of stresses with increase in load can be seen in the stiffeners and the rings can be seen in Figure B.5 and Figure B.6 respectively. The riveted model predicts higher stiffener stresses, which may be explained by the fact that the tie constraint allows better load transfer between the skin and the stringers, which would enable a higher ”effective width” of the skin which would alleviate the compression force into the stringers. For the rings, the stresses are slightly lower for the riveted model early during the loading, which then become slightly higher.

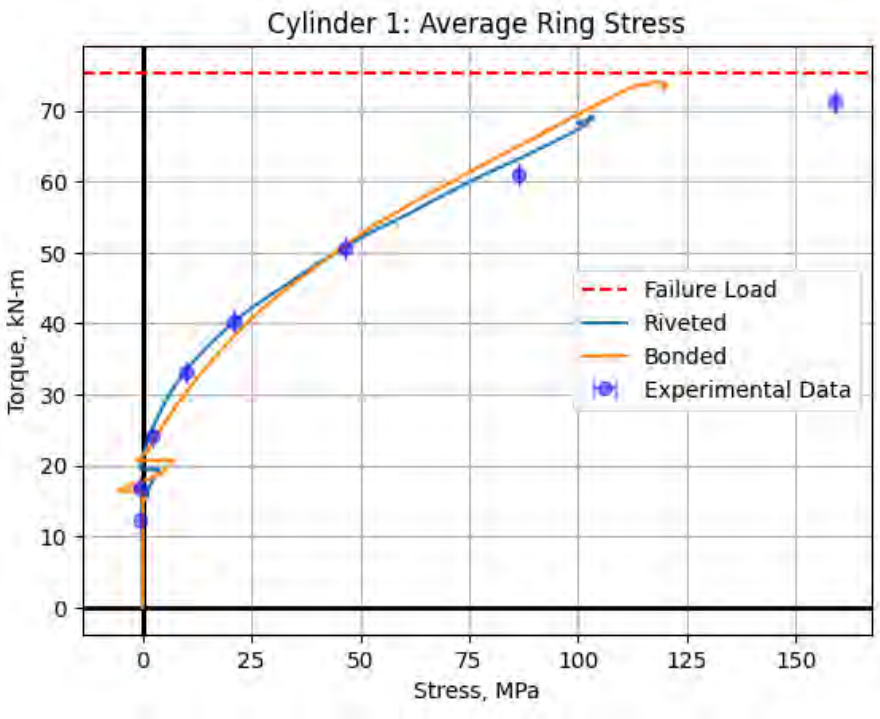

Figure B.6: Comparison of ring stresses for the riveted and bonded models

Finally, given that there is significant differences between the behaviour modelled using the tie constraints and using point-based fasteners, it was decided to use the latter to compare with the experimental results.

C

Mesh

C.1. Mesh Convergence Study

In order to ensure that the mesh in the model is fine enough to provide accurate results. The variable used to judge convergence was the stress developed at the middle of the central bay for stringers and the middle of a bay in the middle-most ring. A detailed study was run on Cylinder 1 (see Figure C.1) and it was assumed that the other Cylinders with the same number of rings would also show converged behaviour. However, a study later conducted for Cylinder-2 showed that the finer skin mesh is needed for the stresses in the rings of Cylinder-2 to converge (see Figure C.2). In the meshing scheme used in the analysis, along the axis, the mesh size of the stringer matched mesh size in the skin. This was also the case for the rings except in some cases when the ring was meshed to a finer degree compared to the skin. The mesh for all cylinders were considered converged at the following parameters:

- Skin Mesh Size: 5.0 mm
- Stringer Mesh Size (Global): 5.0 mm
- Ring Mesh Size (Global): 5.0 mm
- Elements on Stringer Flange: 5
- Elements on Stringer Web: 5
- Elements on Ring Flange: 4

In all cases, the convergence was judged roughy for the mesh size at which the results do not change significantly on further increasing the mesh size. A stricter criteria for this may have been decided. However, considering that increasing the mesh density significantly increases the computational expense (requiring over two days for a single analysis using the available

resources), the current mesh size was considered adequate to capture the stresses for the analysis performed.

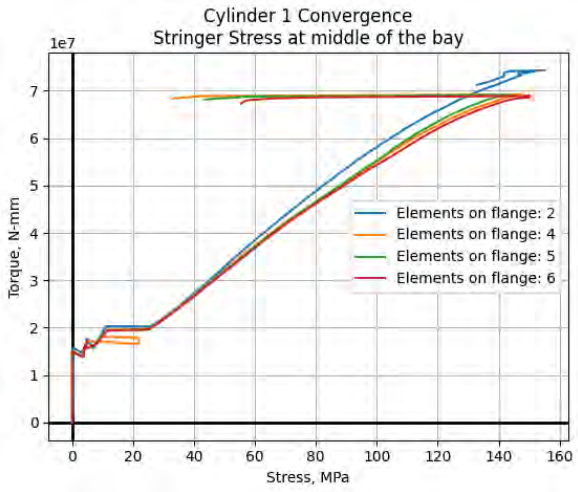

(a) Stringer stress: number of elements in flange

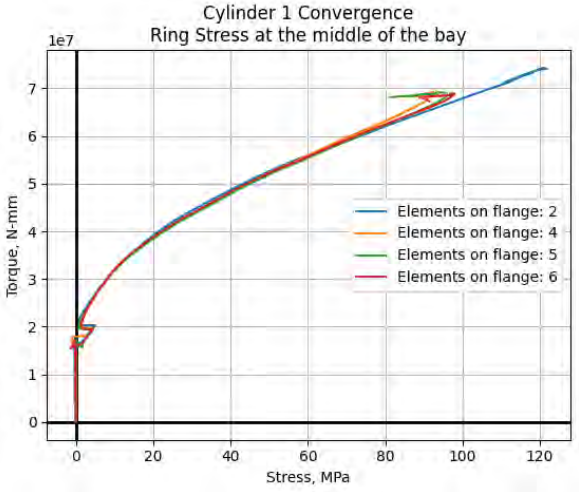

(b) Ring stress: number of elements in flange

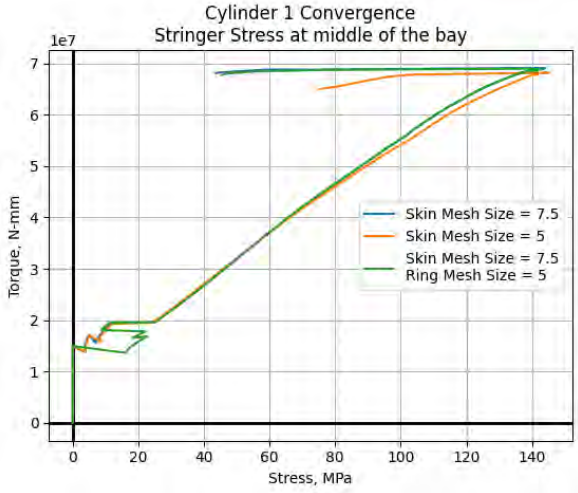

(c) Stringer stress: mesh size in skin (= mesh size in the stringer)

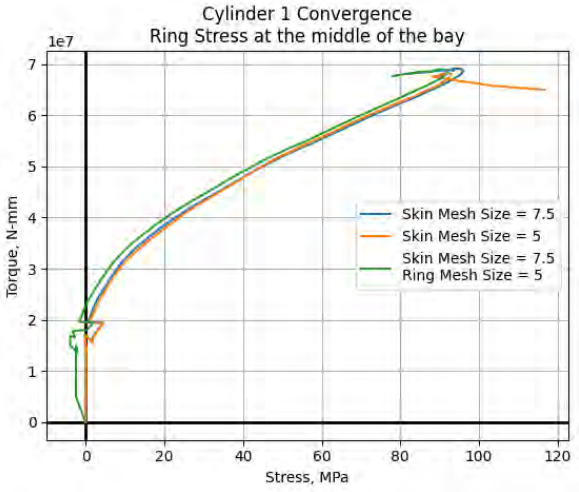

(d) Ring stress: mesh size in skin (= mesh size in the ring, unless stated otherwise)

Figure C.1: Mesh Convergence for Cylinder 1

C.2. Discussion on convergence of Extracted Loads

For the study, it was assumed that the mesh for converged stresses at the extraction location would result in convergence of the extracted load because the latter is a quantity that derives from the earlier and is averaged over the cross section. This was true for the axial forces in the stringers and the rings and the radial bending moment in the stringer as it can be seen from Figure C.4, where the average and maximum values for the forces and the maximum bending moment in Cylinder-2 do not change significantly with the mesh size in the skin, which is equal to the global mesh size of the stringers and the rings. This implies that these values extracted from the skin are valid to be compared with the semi-empirical method as was done in chapter 5.

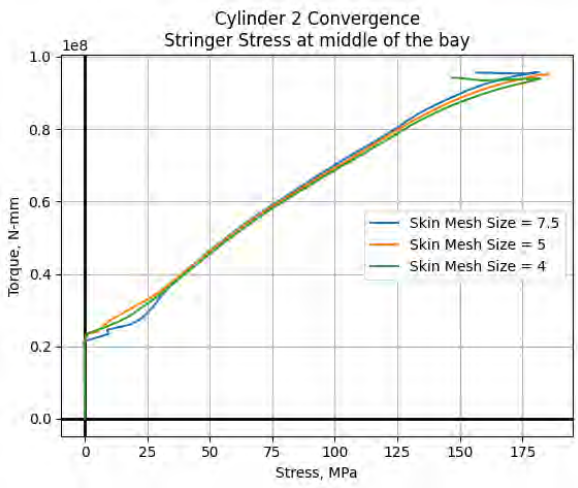

(a) Stringer stress: mesh size in skin (= mesh size in the stringer)

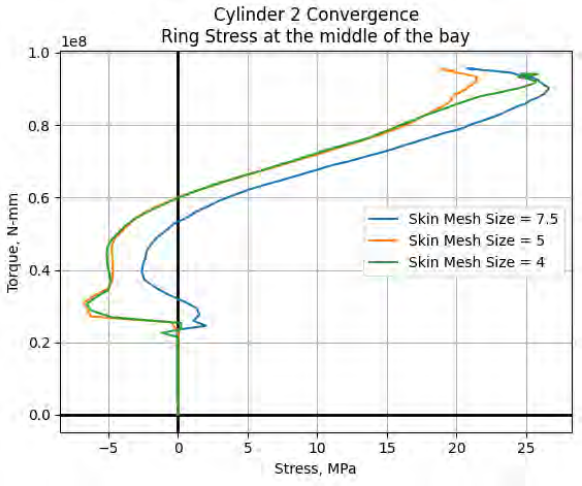

(b) Ring stress: mesh size in skin (= mesh size in the ring)

Figure C.2: Mesh Convergence for the skin for Cylinder 2

However, it was observed that this is not the case for all outputs. The axial and shear forces at the middle of a stringer and at the middle of a bay in the middle-most ring for Cylinder-2 are shown in Figure C.5 where it can be seen that while the axial and radial shear forces have converged for the mesh used for the analyses presented in this study (which is a size of 5mm in the skin), the circumferential shear force does not seem to be converged.

Furthermore, a look into the distribution of the loads along the length of the stiffeners show a very distinct jagged behaviour characterised by sharp changes in loads, which are most prominent in the circumferential shear force distributions in the stringers (see Figure E.2) and the in-plane shear force distribution in the rings (see Figure D.6). It was observed that the locations of the jaggedness correspond with the rivet locations, which is easy to see for the rings, where there are 7 sharp changes in the distribution within a bay, corresponding to the 7 rivet locations in every ring bay as seen in Figure C.3. However, the jaggedness was only noticed for the finer meshes, so there is reason to suspect that the local behaviour due to the rivets have not converged as further mesh refinement could change the results further.

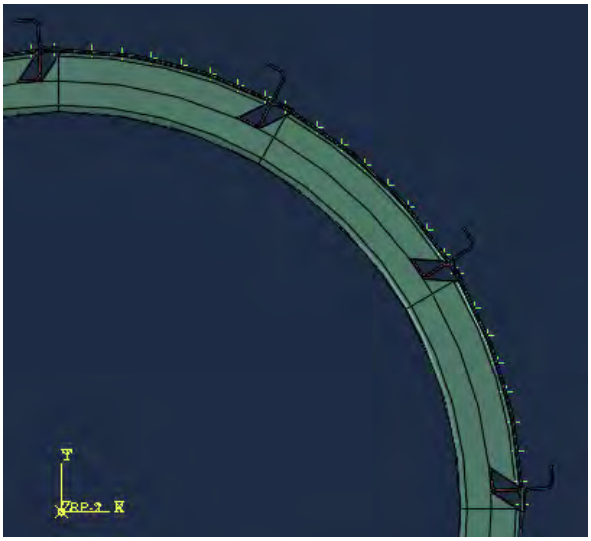

(a) Rivet Locations on the rings

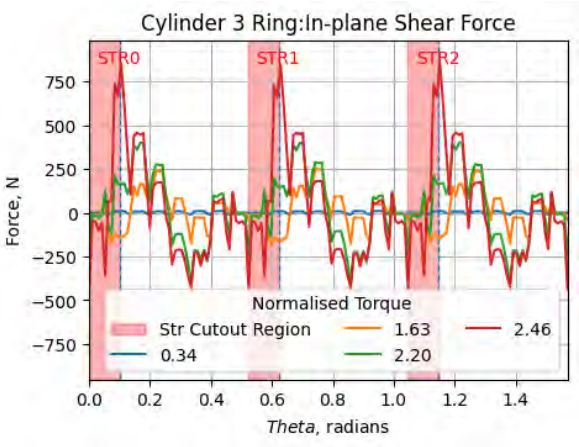

(b) Ring in-plane shear force distribution in the middle-most rings for cylinder 3.

Figure C.3: Jaggedness in the ring in-plane shear force due to the rivet locations in the rings.

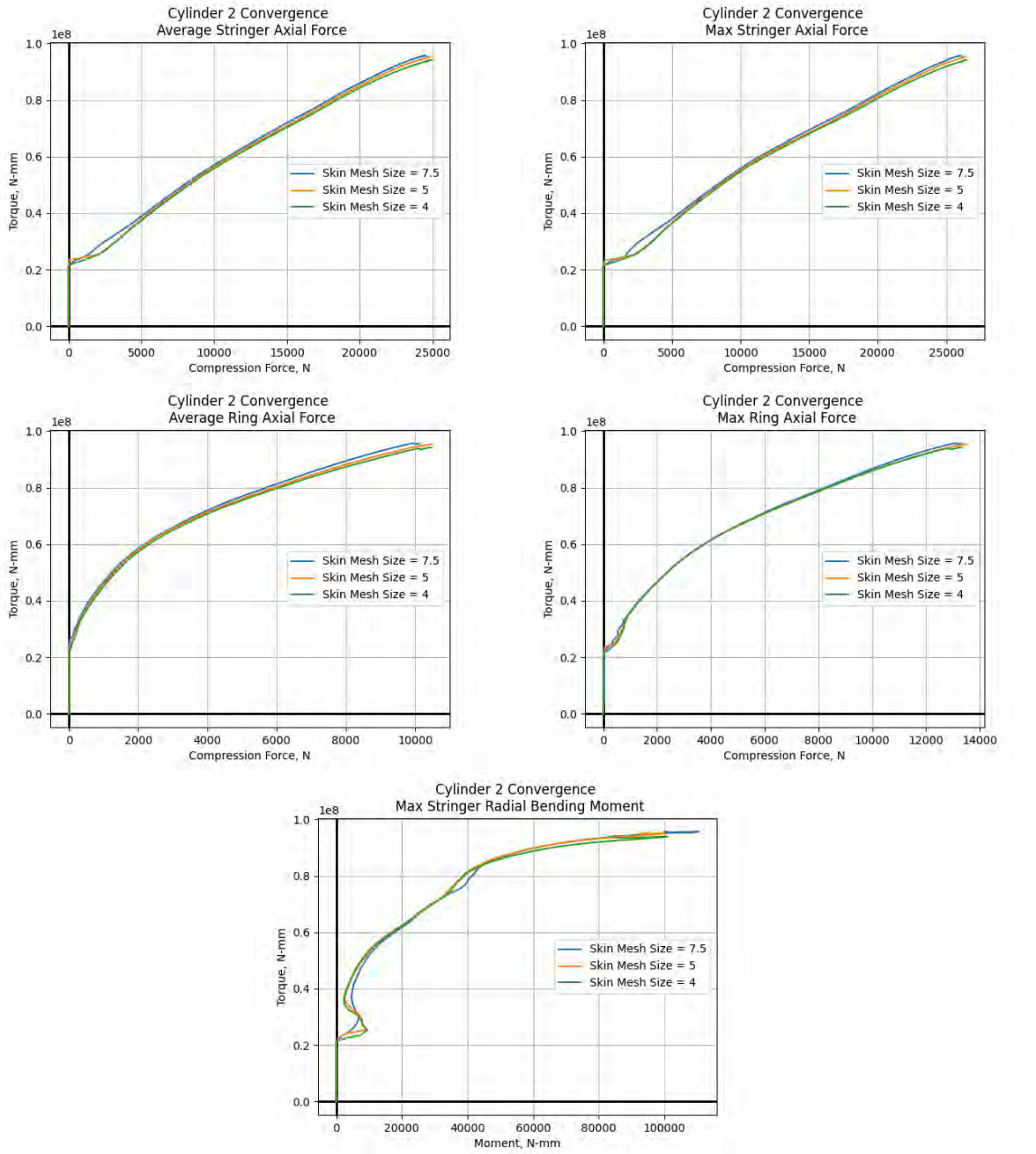

Figure C.4: Skin mesh convergence for average and maximum axial force in the stringer (middle-most bay) and ring (middle-most ring) and the maximum radial bending moment in the stringer (middle-most bay)

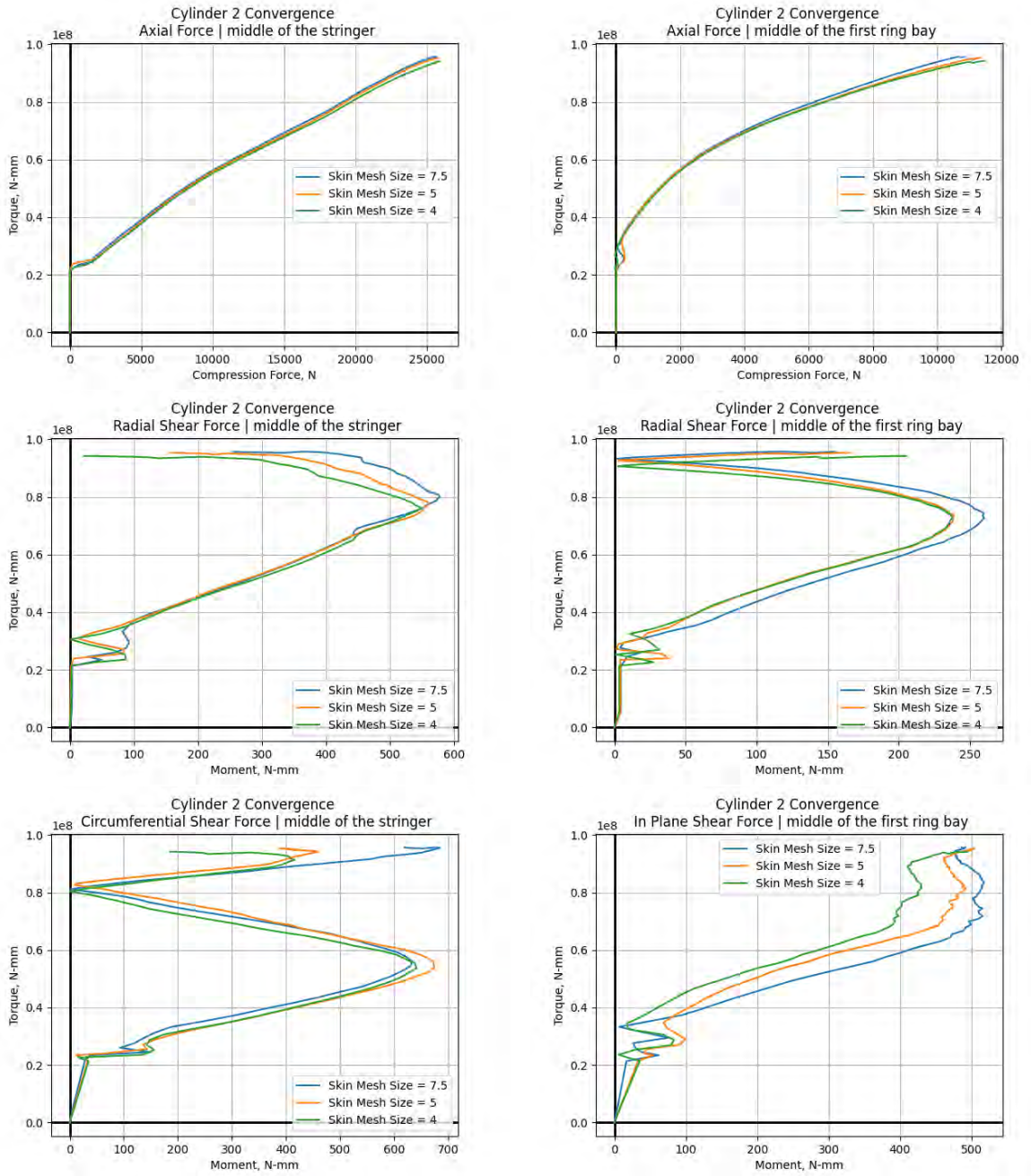

Figure C.5: Skin mesh convergence for the axial and shear forces at the middle of the stringer and at the middle of a ring bay

D

Graphs: Secondary Bending Distributions

This appendix chapter presents the distribution of secondary bending shear forces and bending moments for all cylinders.

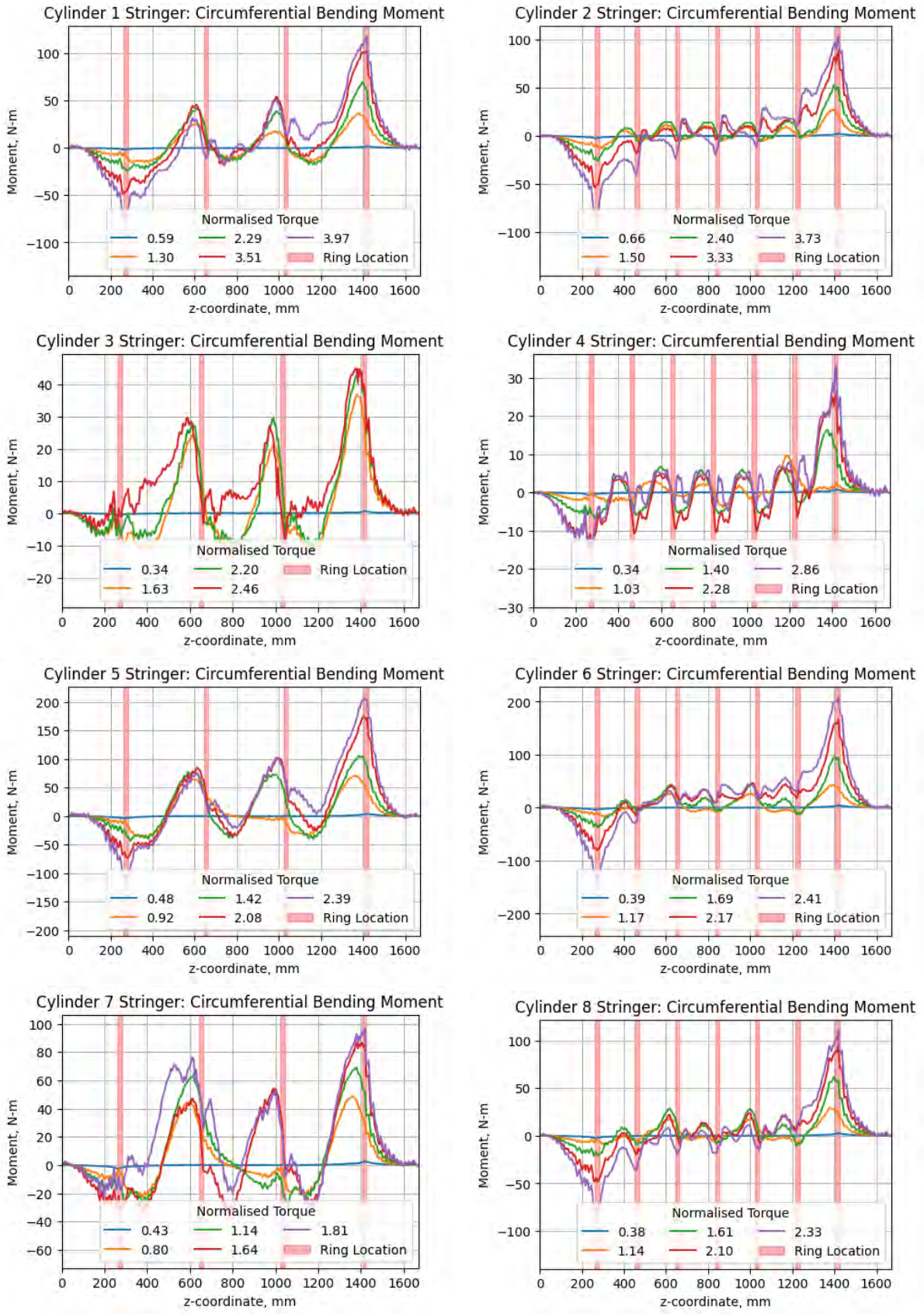

Figure D.1: In-plane bending moment in the stringers at different loads for all perfect cylinders

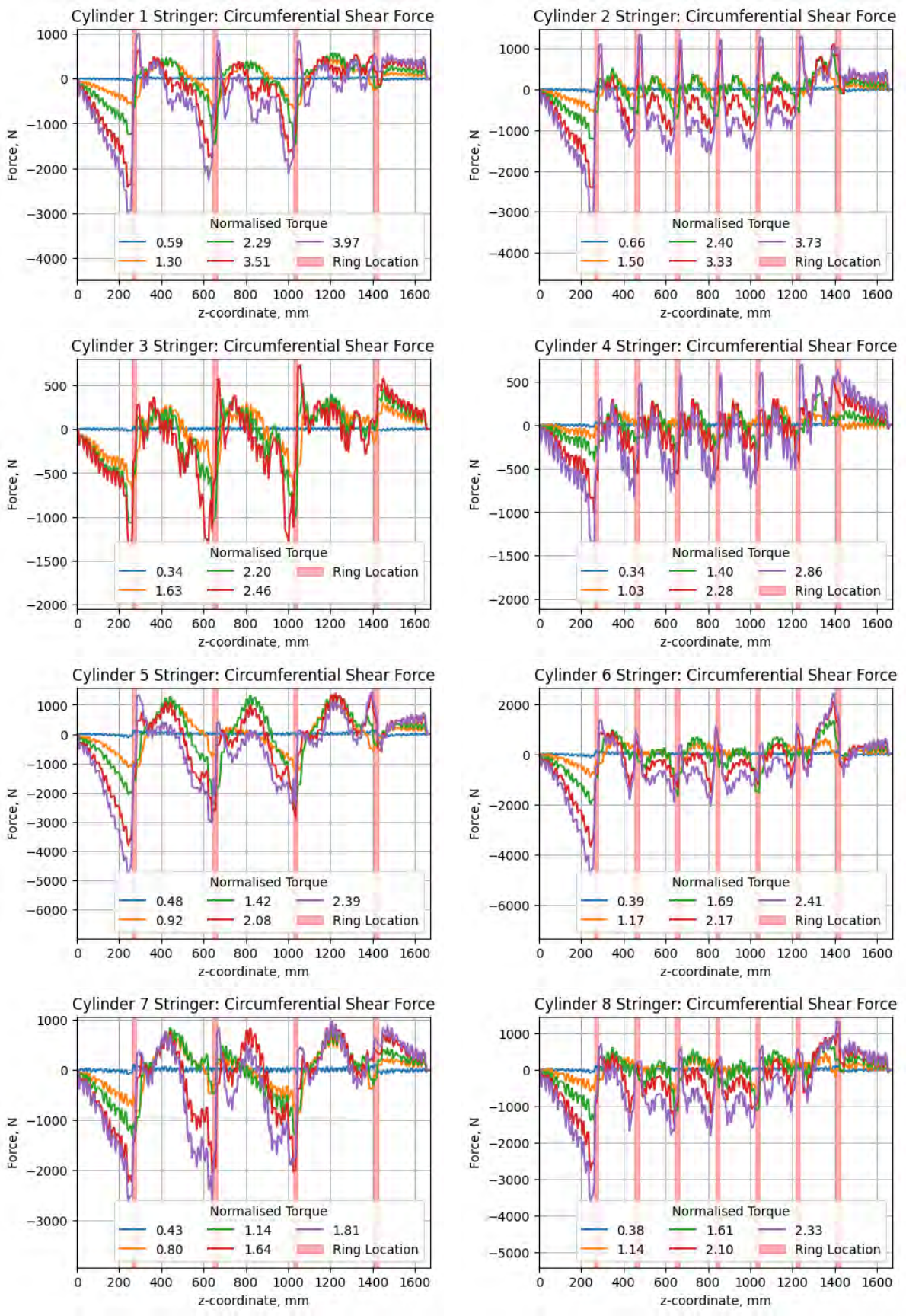

Figure D.2: In plane shear force in the stringers at different loads for all perfect cylinders

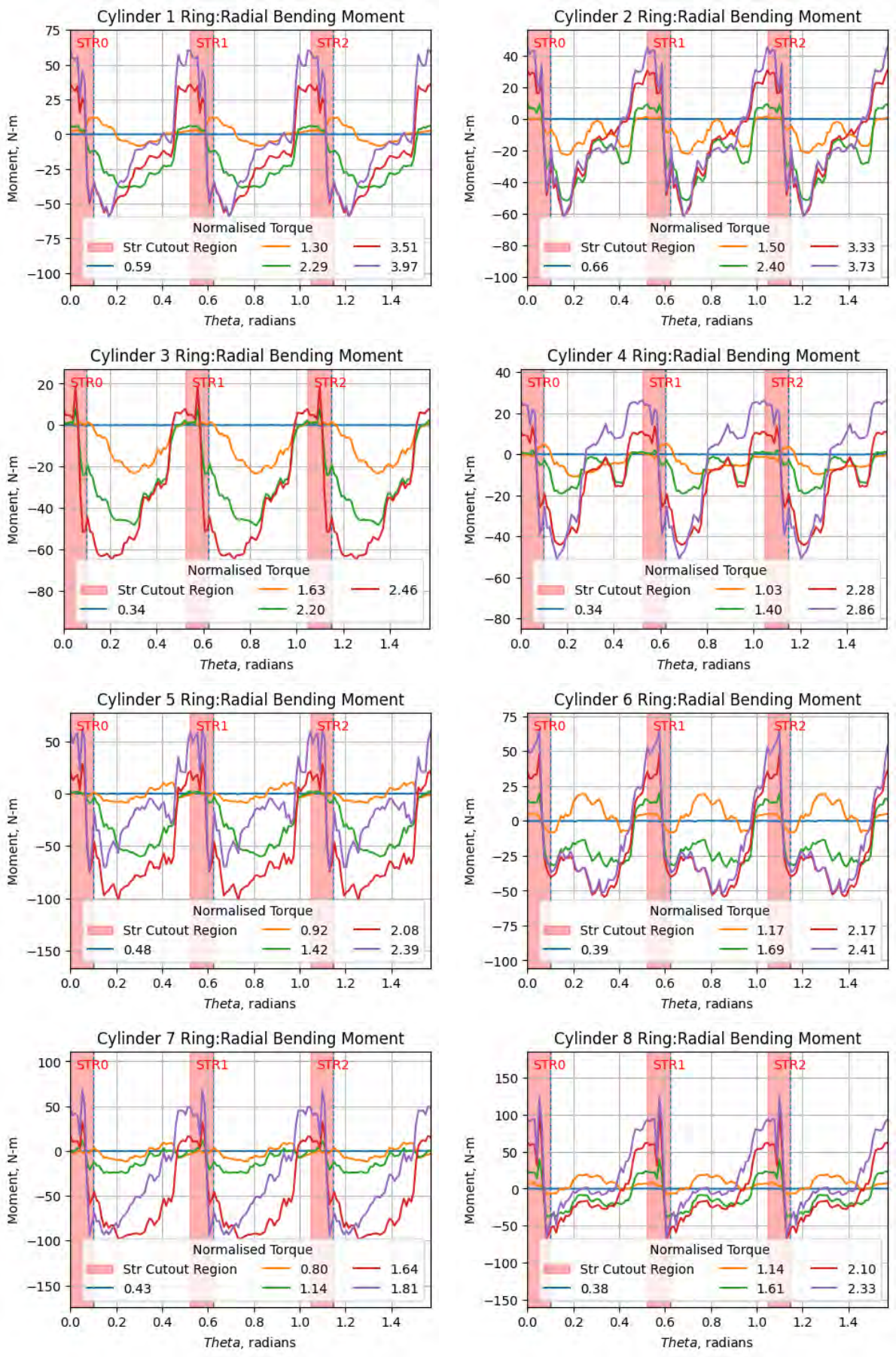

Figure D.3: Radially inwards bending moment in three bays of the middle-most ring at different loads for all perfect cylinders

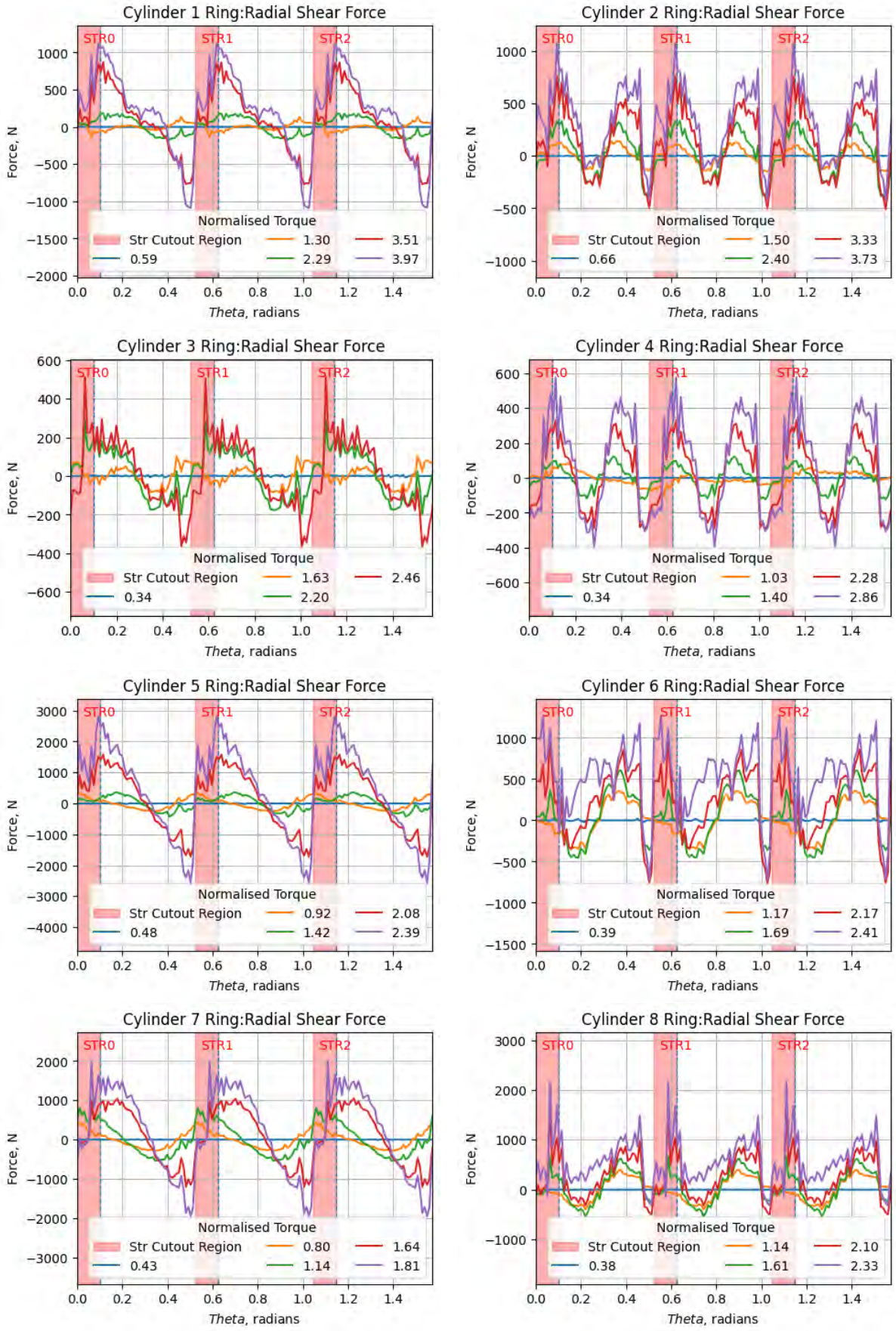

Figure D.4: Radial shear force in three bays of the middle-most ring at different loads for all perfect cylinders

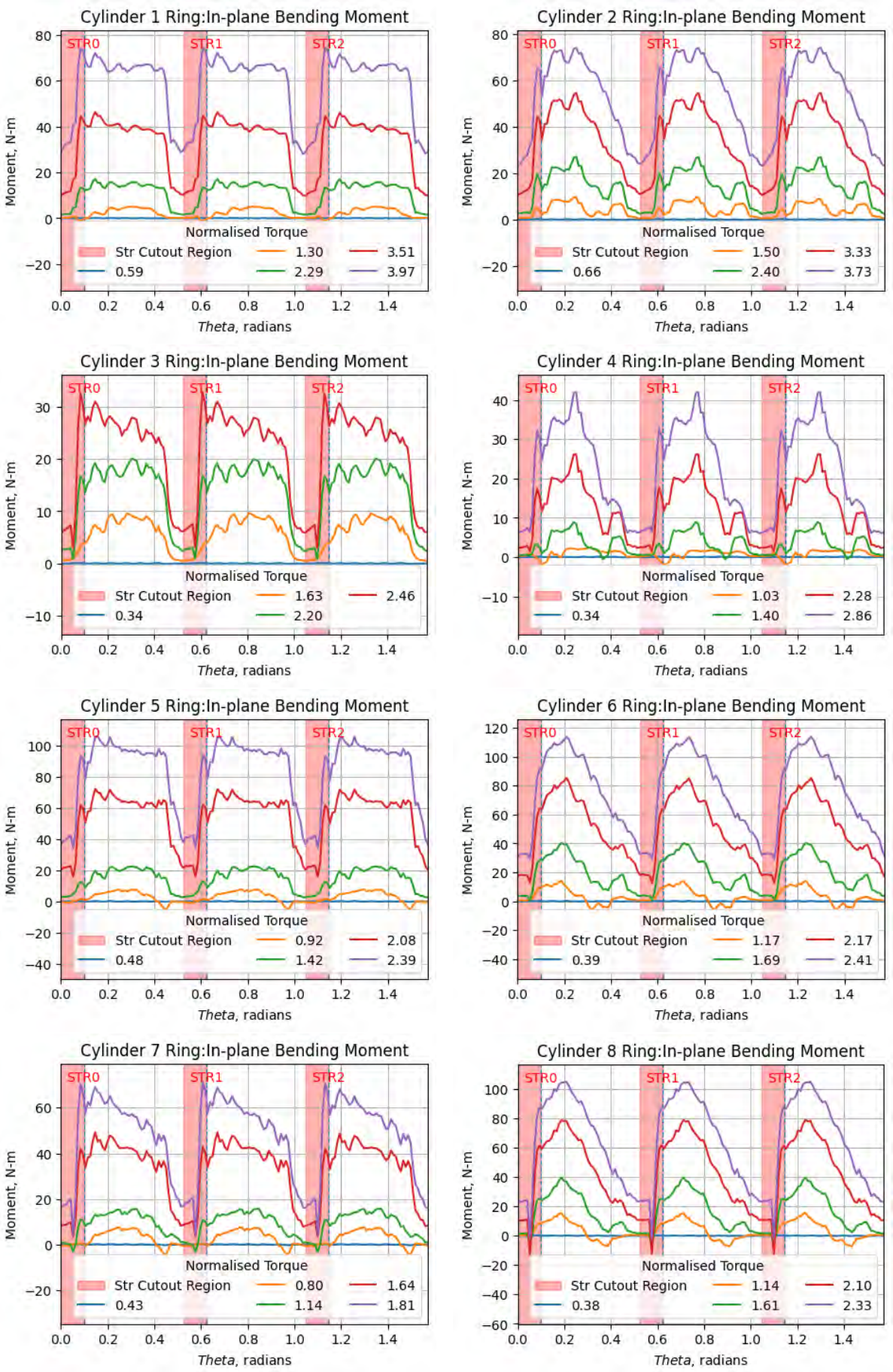

Figure D.5: In-plane bending moment in three bays of the middle-most ring at different loads for all perfect cylinders

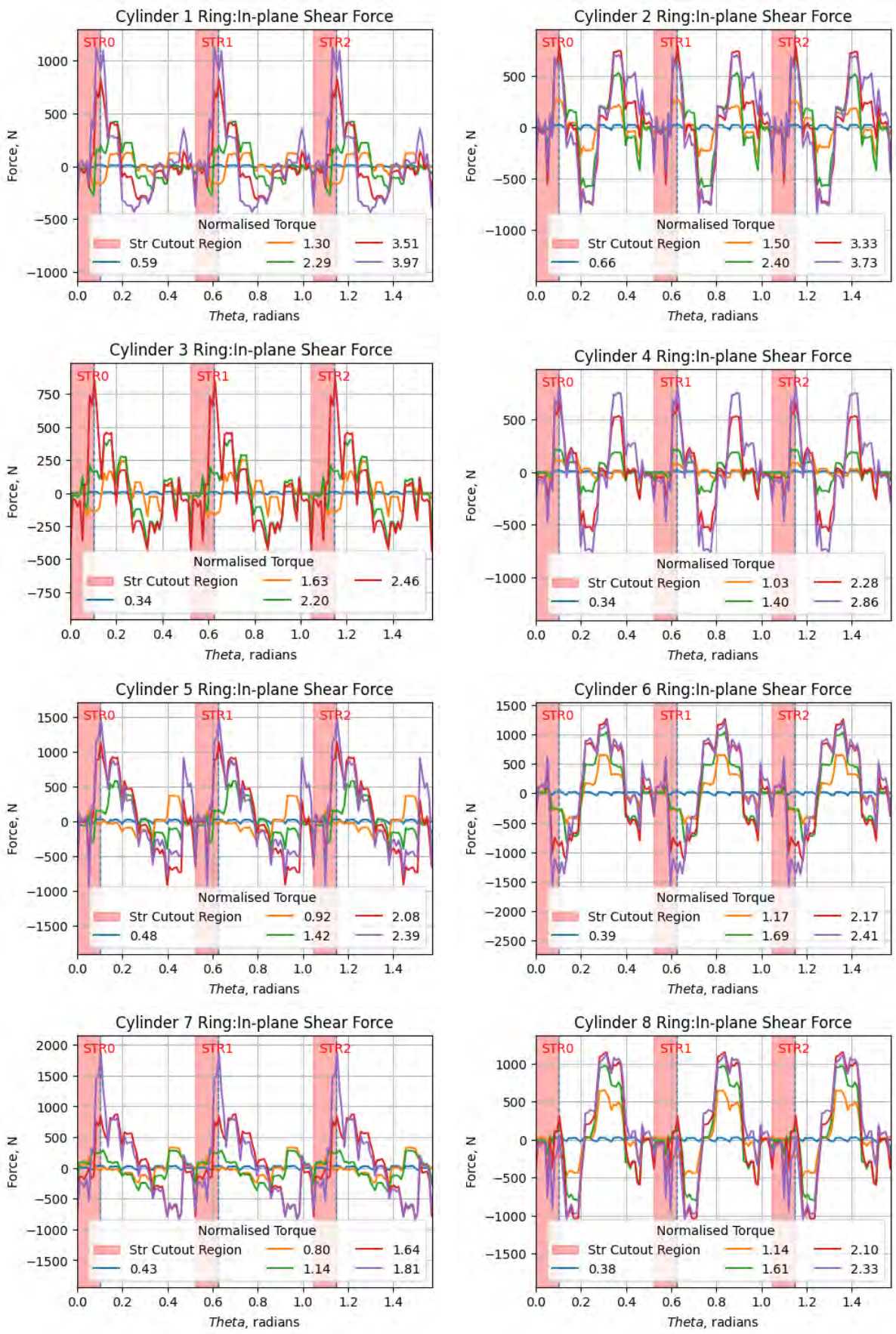

Figure D.6: In plane shear force in three bays of the middle-most ring at different loads for all perfect cylinders

E

Graphs: Skin Section Force Distributions

This appendix chapter presents the axial, circumferential and shear section forces in the skin for all the cylinders at a moderate applied twist at the loaded end which corresponds to a moderately high applied torque. Furthermore, the corresponding deformation pattern is also shown at the end in Figure E.4 for the purposes of noticing its correlation between the section forces.

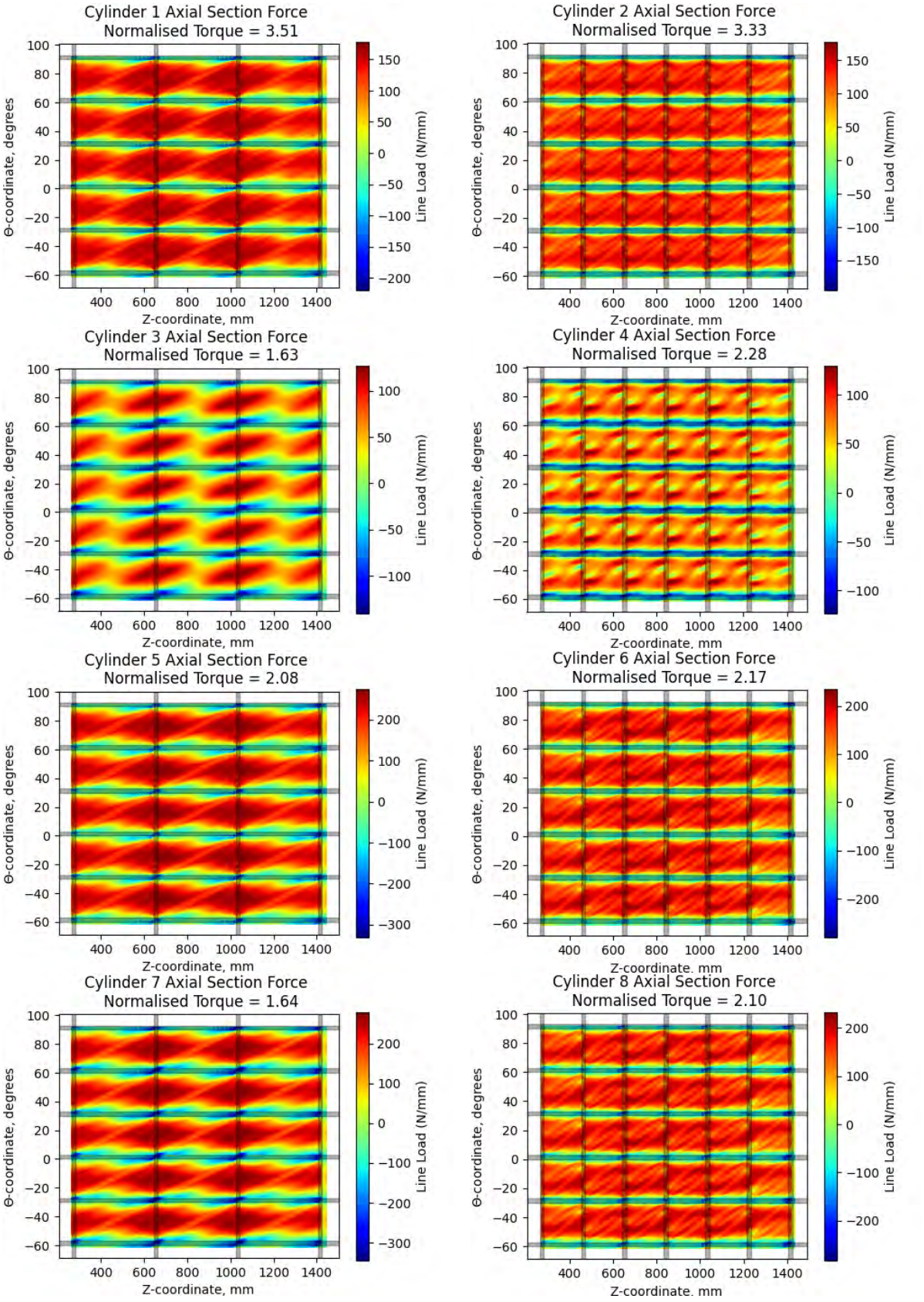

Figure E.1: Axial Force Distribution in the skin at a certain moderately high post-buckling load

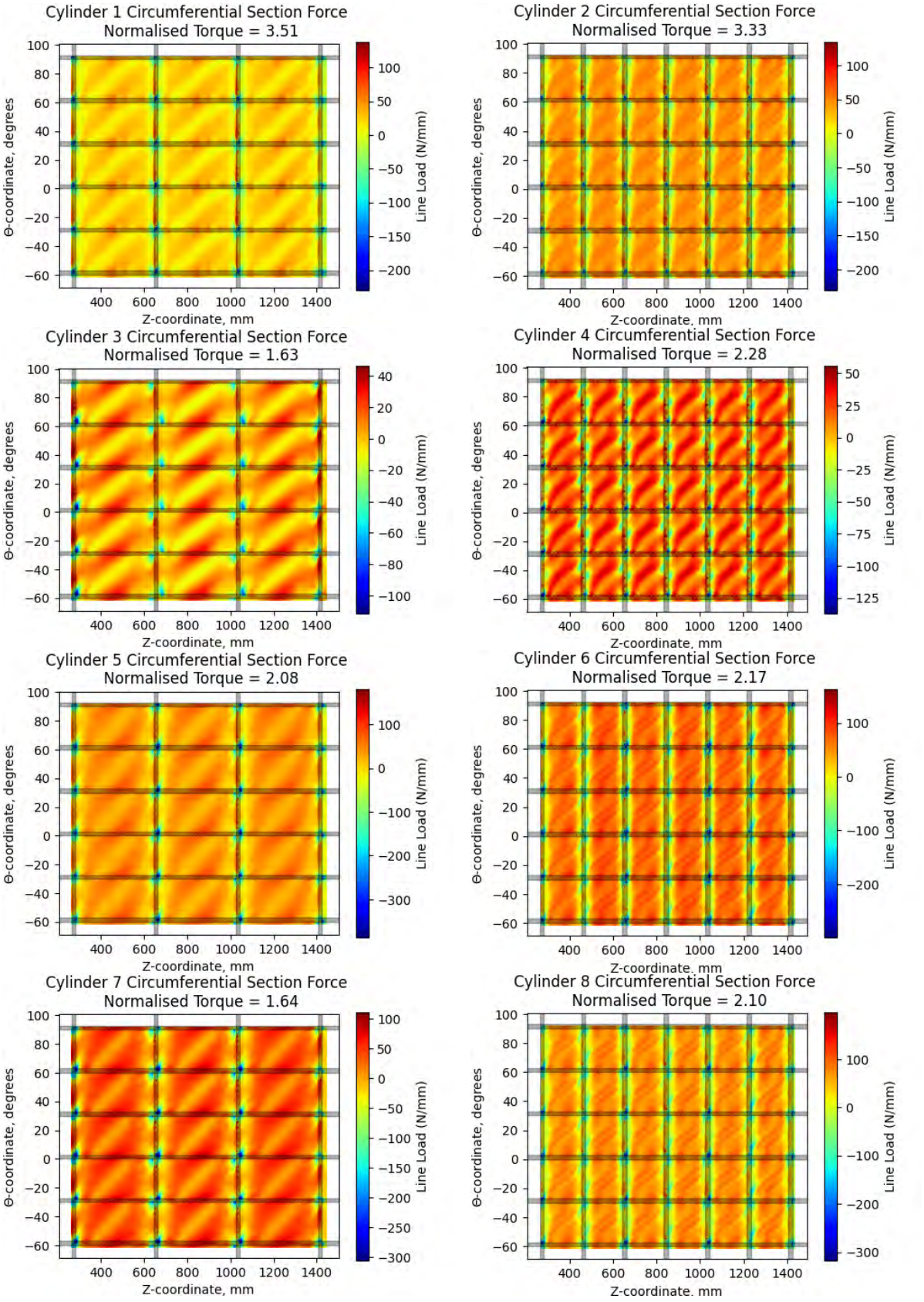

Figure E.2: Circumferential Section Force Distribution in the skin at a certain moderately high post-buckling load

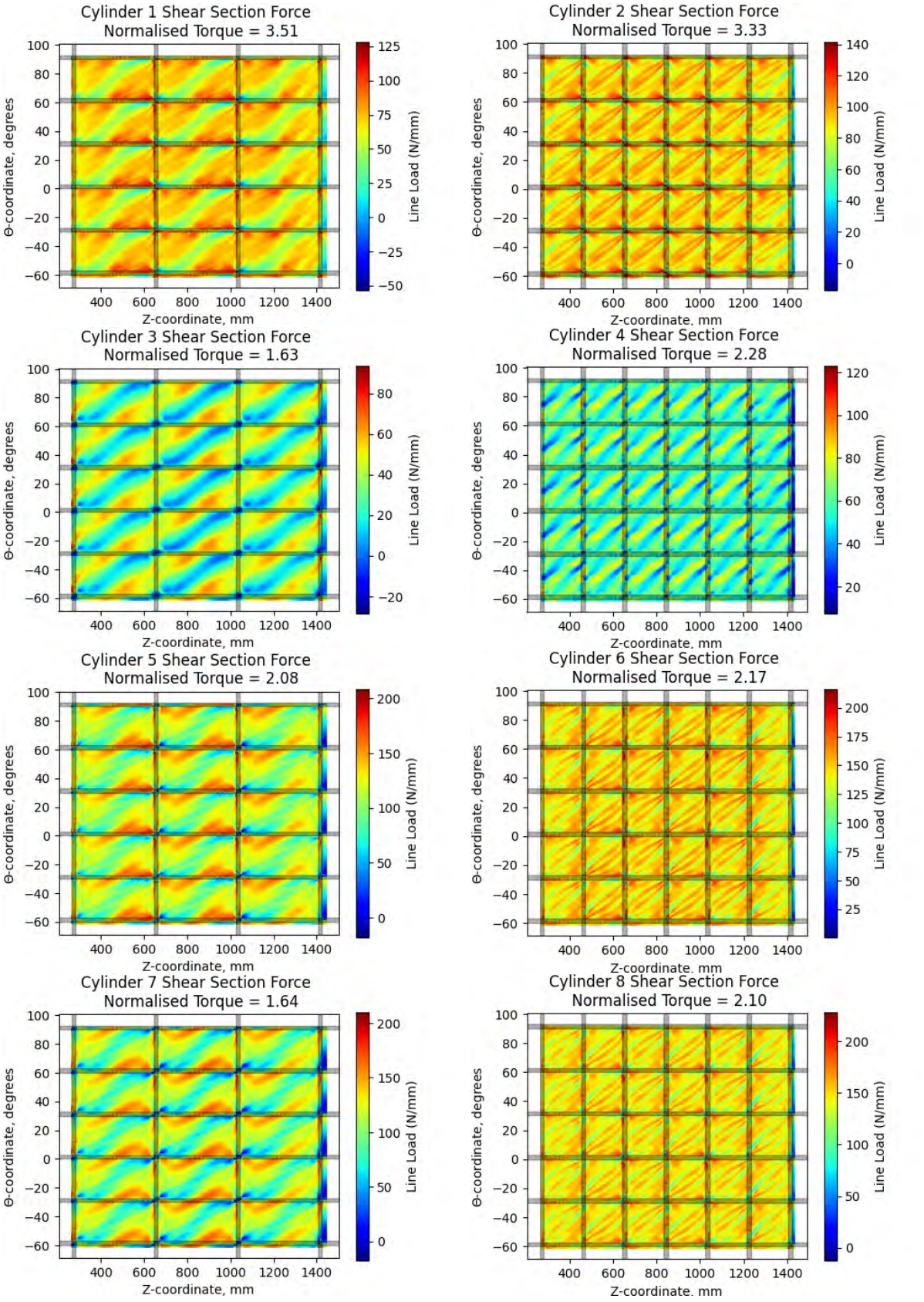

Figure E.3: Shear Section Force Distribution in the skin at a certain moderately high post-buckling load

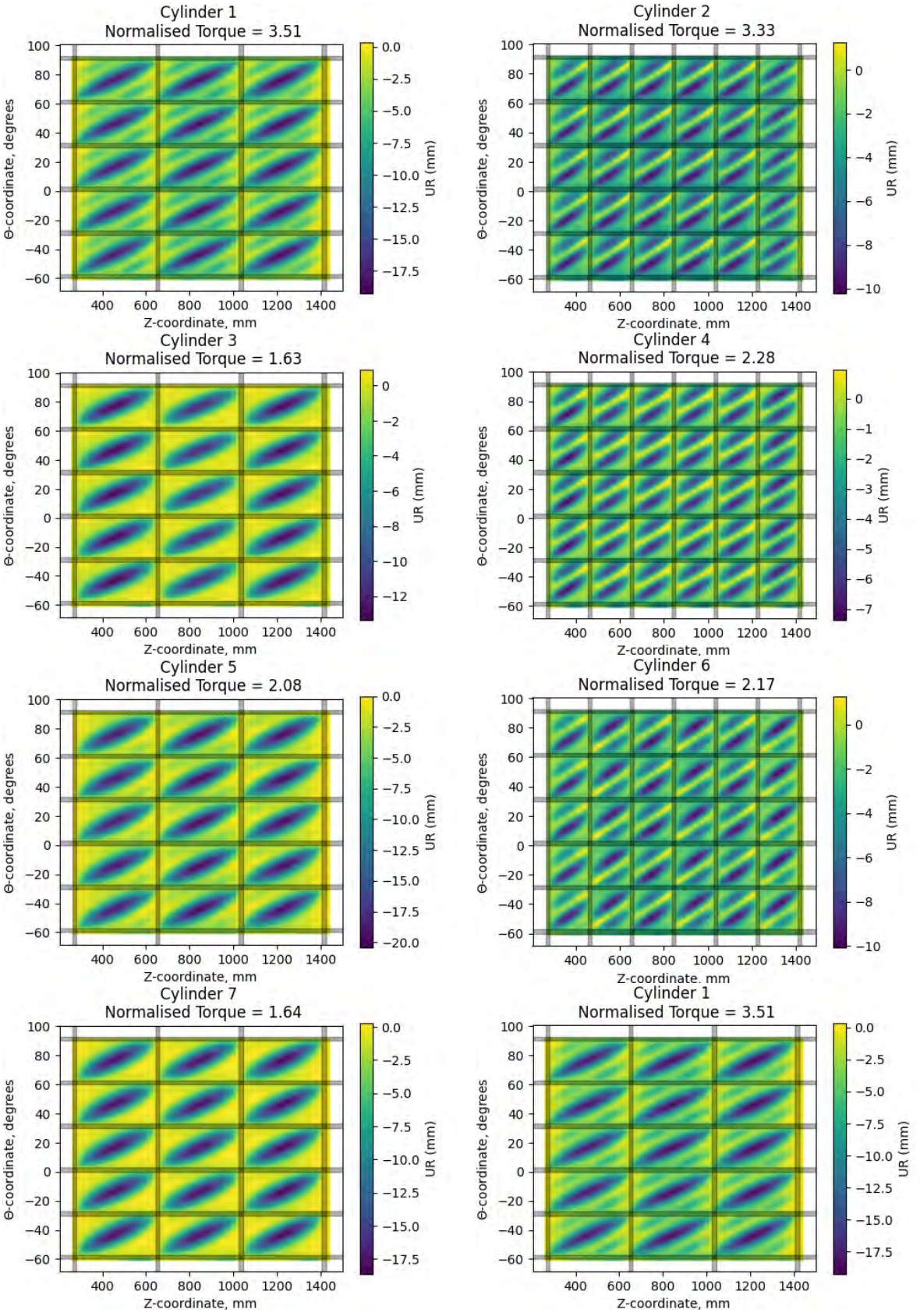

Figure E.4: Deformation pattern on the skin a certain moderately high post-buckling load